

# Arbeitsbericht NAB 12-47

**Laboratory Characterisation of Cores  
(Geothermal Well Schlattingen SLA-1,  
Switzerland):**

**Petrophysics and rock mechanics / physics**

November 2012

J. Sarout (Rock mechanics/physics)  
L. Esteban (Petrophysics: X-ray & NMR)  
M. Josh (Petrophysics: Resistivity & Dielectrics)

CSIRO-ESRE

Nationale Genossenschaft  
für die Lagerung  
radioaktiver Abfälle

Hardstrasse 73  
CH-5430 Wettingen  
Telefon 056-437 11 11

[www.nagra.ch](http://www.nagra.ch)



# Arbeitsbericht NAB 12-47

**Laboratory Characterisation of Cores  
(Geothermal Well Schlattingen SLA-1,  
Switzerland):**

**Petrophysics and rock mechanics / physics**

November 2012

J. Sarout (Rock mechanics/physics)  
L. Esteban (Petrophysics: X-ray & NMR)  
M. Josh (Petrophysics: Resistivity & Dielectrics)

CSIRO-ESRE

**KEYWORDS**

Schlattingen, petrophysics, laboratory tests,  
rock mechanics, rock physics, mineralogy, porosimetry,  
dielectrics, X-ray tomography, scratch tests

Nationale Genossenschaft  
für die Lagerung  
radioaktiver Abfälle

Hardstrasse 73  
CH-5430 Wettingen  
Telefon 056-437 11 11

[www.nagra.ch](http://www.nagra.ch)

Nagra Working Reports concern work in progress that may have had limited review. They are intended to provide rapid dissemination of information. The viewpoints presented and conclusions reached are those of the author(s) and do not necessarily represent those of Nagra.

"Copyright © 2012 by Nagra, Wettingen (Switzerland) / All rights reserved.

All parts of this work are protected by copyright. Any utilisation outwith the remit of the copyright law is unlawful and liable to prosecution. This applies in particular to translations, storage and processing in electronic systems and programs, microfilms, reproductions, etc."

## Table of Contents

Table of Contents .....	I
List of Tables.....	III
List of Figures .....	V
<b>1 Introduction .....</b>	<b>1</b>
1.1 Background and scope .....	1
1.2 The geothermal well Schlattingen SLA-1 .....	3
<b>2 Cores X-ray characterization .....</b>	<b>7</b>
<b>3 Mechanical characterization.....</b>	<b>13</b>
3.1 Introduction .....	13
3.2 Whole Core Scratching.....	13
3.2.1 Principle.....	14
3.2.2 Experimental Methodology .....	16
3.2.3 Results .....	17
3.3 Uniaxial Loading of Cylindrical Plugs .....	29
3.3.1 Experimental Methodology .....	29
3.3.2 Results .....	30
<b>4 Petrophysics/rock physics characterization .....</b>	<b>33</b>
4.1 Nuclear Magnetic Resonance .....	33
4.1.1 Spin Polarization and Longitudinal Relaxation Time $T_1$ .....	33
4.1.2 Spin Tipping onto the Measurement Plane and Free Induction Decay (FID) .....	34
4.1.3 Spin Refocusing, CPMG Pulse Sequence and Transverse Relaxation Time $T_2$ .....	35
4.1.4 Plug preparation and methodology .....	37
4.1.5 NMR results.....	37
4.2 Dry-wet water mass and grain density.....	46
4.3 Mineralogy analysis.....	51
4.3.1 Semi-quantitative XRD analysis.....	51
4.3.2 X-ray Diffractometry and Cationic Exchange Capacity methodology.....	52
4.3.3 Principle and methodology of Specific Surface Area measurements.....	52
4.3.4 Results: XRD, CEC and SSA .....	53
4.4 Electrical properties at low frequency .....	58
4.4.1 Experimental methodology.....	59
4.4.2 Pore water salinity .....	60
4.4.3 Results .....	64
4.5 Electrical properties at high frequency .....	70
4.5.1 Principle of dielectric measurements.....	70
4.5.2 Experimental methodology and results .....	73

4.6	Ultrasonic wave velocities.....	85
<b>5</b>	<b>Summary and discussion.....</b>	<b>89</b>
5.1	Empirical correlations of physical properties .....	89
5.1.1	Dielectrics and P-waves ultrasonic velocities.....	89
5.1.2	Dielectrics and SSA.....	91
5.1.3	Mineralogy, water content and velocities .....	102
5.2	Executive summary of petrophysics and rock physics results.....	102
<b>References</b>	.....	<b>105</b>
<b>Appendix A – Structure of the electronic data base</b>	.....	<b>109</b>
<b>Appendix B – Photo documentation of core samples</b>	.....	<b>111</b>

## List of Tables

Tab. 1-1:	Summary of the rock cores received and tested by CSIRO (see Appendix B).....	2
Tab. 1-2:	Important technical borehole information about the geothermal well Schlattingen-1.....	5
Tab. 3-1:	Summary of the results of the scratch tests on the cores SCR1 – SCR4. Arithmetic mean and variance are calculated for the entire core length and for the core sections, which correspond to the sub-cored plugs. ....	18
Tab. 3-2:	Summary of the results of the uniaxial loading test on the specimen extracted from the deepest end of the cores SCR01, SCR02 and SCR03. Full dataset can be found in a digital format in the file UCS-SCR01.xls, UCS-SCR02 and UCS-SCR03.....	30
Tab. 4-1:	Water content (mass normalized) from NMR using 1st amplitude and NMR time distribution with the 3 echo sequences for each NAGRA samples. ....	40
Tab. 4-2:	Semi-quantitative XRD analysis on the NAGRA plug samples.....	51
Tab. 4-3a:	Semi-quantitative analysis of the SLA-1 collection with interpretation of the rock type by Nagra and CSIRO, respectively.....	54
Tab. 4-3b:	Total fractions of clay, carbonate, quartz and feldspars, derived from the detailed XRD analysis of the SLA-1 collection with interpretation of the rock type by Nagra and CSIRO, respectively.....	55
Tab. 4-4:	Detailed XRD analysis with CEC and SSA results on the full NAGRA collection. ....	56
Tab. 4-5:	Recipe for the pore water NAGRA collection (from Report AN 11-159). Note that the mass correction of kg/kg of water as volumetric units of kg/L of water is ignored because of a negligible deviation smaller than analytical uncertainties.....	61
Tab. 4-6:	Electrical conductivity (I) from anion/cation. Database compiled from Shugar and Dean, 1990; Atkins, 1986; Berezanski, 1997; Sawyer et al., 1995; Holler and Enke, 1996.....	61
Tab. 4-7:	Results of salinity and electrical conductivity of the brine extracted from the NAGRA sample collection.....	63
Tab. 4-8:	Tectrical resistivity results from the NAGRA plugs. ....	67
Tab. 4-9:	Archie’s parameters computed from electrical resistivity at 1 kHz under 100 psi confining pressure and brine saturation of 19.25 mS/cm.....	68
Tab. 4-10:	Dielectric analysis of the SLA-1 samples including the real dielectric permittivity, the equivalent imaginary dielectric permittivity and the equivalent conductivity for all the preserved samples. Measurements were made using the parallel plate dielectric cell and cling film coupling. ....	75
Tab. 4-11:	Dielectric analysis of the Nagra samples including the real dielectric permittivity, the equivalent imaginary dielectric permittivity and the equivalent conductivity for all the preserved samples. Measurements were made using the parallel plate dielectric cell and brine coupling.....	75

Tab. 4-12:	Data from electrical high frequency on a selection of the NAGRA collection: real dielectric permittivity, equivalent imaginary dielectric permittivity and equivalent electrical conductivity from discs preserved in glad film and in brine and from powders (specific collection: NAGRA-G, -H, -I and -SCR04). .....	80
Tab. 4-13:	Summary table of P- and S-wave velocities obtained on plugs extracted from cores A to J and from SCR04. ....	86
Tab. 5-1:	Executive summary of petrophysics and rock physics results.....	104

## List of Figures

Fig. 1-1:	Topographic map, displaying the location of the geothermal well Schlattingen-1 (SLA-1). .....	3
Fig. 1-2:	Stratigraphy of the geothermal well Schlattingen-1 (SLA -1).....	4
Fig. 2-1:	X-ray CT scanograms of the cores used for scratch testing (SCR01 to SC05). Blue rectangles stand for the three plugs extracted for uniaxial stress testing, whereas red rectangles stand for the plugs extracted for Fast Tracked Petrophysic testing workflow. Note that the bright horizontal stripe that appear on the images are artefacts related to the plexiglass couch where seat the cores to maintain them in a horizontal plane. ....	7
Fig. 2-2:	X-ray CT scanograms of the cores used for the Fast Tracked Petrophysic testing workflow.....	8
Fig. 2-3:	Example of transversal CT slices acquired every 1cm along the core SCR04 from top to bottom. ....	9
Fig. 2-4:	Example of X-ray CT slice images obtained on the plug NAGRA-A extracted from the lowest (deepest) part of the core A. Note that the plug and discs used for dielectric and other petrophysical characterization appear in these scans. ....	11
Fig. 2-5:	Example of 3D high density map reconstructed from the CT slice images of the plug NAGRA-B extracted from the lowest (deepest) part of the core B.....	12
Fig. 3-1:	Force decomposition of the cutting process (Detournay and Defourny, 1992).....	14
Fig. 3-2:	Linearity between the tangential component of the force on the cutting face $F_{cs}$ and the cross sectional area $wd$ (Richard, 1999).....	15
Fig. 3-3:	Correlation between intrinsic specific energy $\varepsilon$ and UCS (Richard, 1999). ....	16
Fig. 3-4:	Experimental setup: Scratch test apparatus, also known as the <i>Wombat</i> .....	17
Fig. 3-5:	SCR01. Scratch test results: Four depths of cut have been used. The core has been scratched from top to bottom (right: original data; middle: cut-off of edge effects; left: moving average).....	19
Fig. 3-6:	SCR01. Unconfined compressive strength log (UCS log). The data for this test can be found in a digital form in the file Scratch-SCR01.xls. Note, the horizontal stripe in the CT scan at 748.64 m images the fixation of the core sample. The little nodule at 748.6 m exhibits a carbonate spot which may give rise to the enhanced UCS value at this location.....	20
Fig. 3-7:	SCR02. Scratch test results: Four depths of cut have been used. The core has been scratched from the bottom to the top (right: original data; middle: cut-off of edge effects; left: moving average).....	21
Fig. 3-8:	SCR02. Unconfined compressive strength log (UCS log). The high UCS value at 770.12 m may be explained by the carbonate spot at this location as seen in the CT scan. The data for this test can be found in a digital form in the file Scratch-SCR02.xls.....	22

Fig. 3-9: SCR03. Scratch test results: Four depths of cut have been used. The core have been scratched from the bottom to the top (right: original data; middle: cut-off of edge effects; left: moving average). ..... 23

Fig. 3-10: SCR03. Unconfined compressive strength log (UCS log). The data for this test can be found in a digital format in the file Scratch-SCR03.xls..... 24

Fig. 3-11: SCR04. Scratch test results: Four depths of cut have been used. The core has been scratched from bottom to top bottom (right: original data; middle: cut-off of edge effects; left: moving average)..... 25

Fig. 3-12: SCR04. Unconfined compressive strength log (UCS log). The data for this test can be found in a digital format n the file Scratch-SCR04.xls..... 26

Fig. 3-13: SCR05. Scratch test results: Four depths of cut have been used. The core has been scratched from bottom to top. .... 27

Fig. 3-14: SCR05. Unconfined compressive strength log (UCS log). The data for this test can be found in a digital format in the file Scratch-SCR05.xls..... 28

Fig. 3-15: Uniaxial stress loading of a cylindrical rock specimen for direct determination of the UCS. Specimen assembly including: (i) two orthogonal pairs of cantilevers for radial strain measurements; and (ii) a pair of diametrically-opposed axial LVDTs for axial strain measurements. .... 29

Fig. 3-16: Rock specimens extracted from cores SCR01 (a), SCR02 (b) and SCR03 (c) pre-testing and post-failure. Stress-strain data for these three tests can be found in digital format in the files UCS-SCR01.xls, UCS-SCR02.xls and UCS-SCR03.xls, respectively. Summary of the main results of these 3 tests are reported in Tab. 3-2. .... 31

Fig. 3-17: Schematic explanation of the possible difference in the estimation of the UCS by the scratch test and the uniaxial loading methods for a heterogeneous rock core. .... 32

Fig. 4-1: Induced curve during Polarization  $T_1$ -relaxation (degree of alignment) as function of the time that hydrogen population is exposed to an external constant magnetic field. .... 34

Fig. 4-2: Explanation of the CPMG pulse sequence to measure  $T_2$ . .... 36

Fig. 4-3: Example of NMR distribution in NAGRA-A plug. The top plot gives the raw signal NMR amplitude normalised to the volume of the plug to extract the water content at the first amplitude: maximum amplitude at the shortest time. The water content can be extrapolated to a time of  $0\mu s$ . The plot in the middle corresponds to the cummulative amplitude from the time distribution of the NMR signal (bottom plot) for each echo sequence method (FID/CPMG/INVREC). The "theoretical" water limit between CBW and capillary-free water is around 3 ms. Using this limit, it gives the amount of water in CBW for each plug. Note that INVREC sees in this example, two changes of slope: at short time (CBW) and long time ( $> 10$  ms: free water sensu-stricto)..... 38

Fig. 4-4: NMR distribution from all the NAGRA collection with  $T_2$  distribution from CPMG (top),  $T_2^*$  distribution from FID (middle) and  $T_1$  distribution from INVREC (Bottom)..... 39

- Fig. 4-5: Water content (%) from NMR with comparisons between the 3 echo sequences (FID/CPMG/INVREC) at the top, and presented under an histogram (bottom plot) to discriminate the specific plug sample with low or high water content. .... 41
- Fig. 4-6: Histogram of NMR water content (%) per sample averaged through the 1st amplitude and time distribution from each NMR methods. Note the very low content in plugs NAGRA-F and -H and the highest for NAGRA-E and -G. .... 42
- Fig. 4-7: Histogram of NMR total porosity (%) per sample computed from the previous water content normalized to the plug volume and averaged through the 1st amplitude (blue color) or through the inversion (red color) from each NMR methods (FID, CPMG and INVREC). Note the very low content in plugs NAGRA-F and -H and the highest for NAGRA-E and -G. The error-bars correspond to the standard deviation between the NMR methods applied on each plug sample. .... 42
- Fig. 4-8: Porosity distribution (%) from all the NAGRA sample collection along the time constant T2 from CPMG NMR method: distribution from preserved (top graph) and distribution from heat treated sample at 65C during 2 days and then rehydrated under room condition during 3 months (Bottom graph). Note how the weak bounded water disappeared after heat treatment whereas the CBW remains. Do not forget that T2 is related to the pore size with increase of the pore size when T2 increases. .... 43
- Fig. 4-9: Computed porosity of the NAGRA sample collection under preserved condition (plug samples in blue color), after heat treatment at 65C during 2 days and rehydrated under room condition during 3 months (disc samples in red color). The stick water or the suspected CBW contribution on the total porosity from preserve condition (%) is also presented in green color for each sample. Note the water absorption (CBW > 100%) for the samples F, H and SCR04.; or the very low water absorption for the samples G, I and J. .... 44
- Fig. 4-10: Effect of sample size on the porosity evaluated from NMR CPMG first amplitude. (a) Porosity on the preserved and heat treated samples versus their length. Note the excellent linear trend for the heat treated samples; (b) Relation of the CBW contribution with the Surface to volume ratio of the samples heat treated. Note how the CBW > 100% (potentially smectite rich) are out of the trend. .... 45
- Fig. 4-11: Water from wet-dry method versus NMR CPMG after 24h and 48h oven dried at 65 °C and 1 month at 105 °C: (a) water content % and (b) derived porosity (%). .... 47
- Fig. 4-12: Porosity lost during heating process compare to its related preserved condition during different duration of heating and temperature for each of the SLA-1 samples..... 48
- Fig. 4-13: Density calculated from water content on NMR and wet-dry method. The bulk density and grain density derived from these methods show over-estimation from NMR on grain density for the samples J and G as well as an under-estimation on bulk density from wet-dry method and correspond to the richest in clay minerals (see semi-quantitative XRD results: Smectite?). .... 49

Fig. 4-14: Water re-hydration tests after heating at 65C during 48h and put under room condition 20mn, 2 days and 3 months. The water added by the humidity inside the sample from the room condition (RH at around 35% and 24C) is calculated as % from its dry mass status..... 50

Fig. 4-15: Water re-hydration of samples oven-dried during 48h and the re-hydrated during 20 min and 2 days at room condition. .... 50

Fig. 4-16: Left) Shales typically are comprised of quartz, feldspar and lithic grains imbedded in an isotropic or anisotropic matrix of clay minerals with a contribution of other possible minerals including carbonates and pyrite. Right) The individual grains of swelling clays have additional surface area within the interlayers which may also be crucial to the petrophysical and geomechanical behaviour of the rock. .... 53

Fig. 4-17: The correlation observed between specific surface area determined by direct measurement in the laboratory using the EGME method and an indirect method analytically determined from XRD mineralogy. There is a good correlation between the analytical SSA determined using XRD and the measured value from sorption of EGME. .... 57

Fig. 4-18: New electro-acoustic rig to perform low frequency electrical resistivity spectrum and axial ultrasonic records under confining stress and fluid saturation. (a) Cell under brine filling to remove the air bubbles; (b) cell ready for measurements; (c) electrodes with transducers and spacers (in red) to adapt the length of the sample; (d) Sleeve with 2 electrode rings in its middle and inserted in one of the electrode part. .... 60

Fig. 4-19: Brine extraction from NAGRA samples after centrifugation. Note the different colors of the brine due to occurrence of organic matter (yellowish color) and in some of the sample a black oil film at the surface of the water also related to oily organic matter. .... 62

Fig. 4-20: Histograms of the pore water salinity in each NAGRA sample. Note the perfect match between the artificial brine from NAGRA and the extracted brine from each sample with some few exceptions: NAGRA-G and SCR04 (higher) and NAGRA-NAGRA-B-D and -F (lower)..... 64

Fig. 4-21: Electrical spectrum on NAGRA-A with 2 and 4 electrodes under no confining pressure..... 65

Fig. 4-22: Resistivity spectrum on NAGRA-A at 2 and 4 electrodes with no confining pressure. .... 66

Fig. 4-23: Time scan of the electrical impedance at three frequency (100Hz, 1 kHz and 10 kHz) with temperature on NAGRA-B. .... 66

Fig. 4-24: Resistivity spectrum with and without confining pressure on 2 and 4 electrodes for the NAGRA-B. .... 67

Fig. 4-25: Archie’s paramaters computed on the SLA-1 collection plugs from electrical resistivity at 1 kHz under 100 psi confining pressure under brine saturation at 19.25 mS/cm. .... 69

Fig. 4-26: Compilation of all the NAGRA plugs measured for their resistivity at 1 kHz (ohm.m) against the water content from NMR (%). .... 70

- Fig. 4-27: Dipolar molecules can rotate to align with the applied electric field. But other charge polarisation processes exist as well..... 71
- Fig. 4-28: An example of a dielectric response based on the models of Debye and and Cole-Cole.  $\epsilon'_{r \text{ low}} = 1000$ ,  $\epsilon'_{r \text{ high}} = 10$ ,  $\tau = 1 \mu\text{s}$  and in the case of Cole-Cole  $\alpha = 0.15$ . Both data sets presented are the same but they are plotted on Left) linear magnitude and Right) log magnitude. .... 72
- Fig. 4-29: Example model of the hydration of clay grain interfaces as water attaches itself to the exposed charge sites at the outer edge of the clay mineral boundary. Cations and anions in the water can also attach themselves to the clay grain and are able to participate in both conduction and polarisation processes when an electric field is applied. .... 73
- Fig. 4-30: Parallel plate dielectric measurement cell. The instrument consists of a three terminal capacitor for which parallel faced disc samples are prepared. The cell can be placed in a load cell to insure good coupling between the sample and the electrodes. .... 74
- Fig. 4-31: Example measurements for Nagra sample A. Top) Real and equivalent imaginary dielectric permittivity responses determined using cling film coupling with Cole-Cole fitting. Bottom) Real dielectric permittivity and conductivity determined using brine coupling (3.5 g/l NaCl). Using cling film coupling we observe a plateau in real dielectric permittivity below 100 KHz of approximately  $\epsilon'_{r} = 300$  which transitions rapidly to a lower value from 100 KHz to 100 MHz. There is a corresponding peak in the dielectric loss (the imaginary component) associated with this transition. The brine coupled real dielectric permittivity is decreasing with increasing frequency; however the conductivity we observe with the brine coupled measurement is generally very flat across the frequency range ( $\sigma = 0.02 \text{ S/m}$ ), but increases slightly above 1 MHz, as a result of additional dipolar loss mechanisms adding to the conduction loss. .... 76
- Fig. 4-32: Comparison of the cling film versus brine treatment measurement procedures for the dielectric parameters  $\epsilon'_{r}$  (real dielectric permittivity),  $\epsilon''_{r}$  (equivalent imaginary dielectric permittivity) and  $\sigma$  (equivalent conductivity). Generally the cling film (Glad) and Brine coupled measurements correlate with one another, however the transition from 1 MHz up to 10 MHz improves the correlation from typically  $\sim 0.6$  up to better than 0.95, which is retained at 1GHz..... 77
- Fig. 4-33: The real dielectric permittivity determined for the averaged “Carbonates” “Shales” and “Marls” from the Nagra Samples. (a) The broad frequency sweep and (b) the 1 MHz to 100 MHz frequency sweep. Below 1 MHz, marls have the highest dielectric permittivity closely followed by the shales and the carbonates are much lower. Above 1 MHz the shales have the highest dielectric permittivity, closely followed by the marls but the carbonates have much lower dielectric permittivity. (c) The conductivity determined for the average “Carbonates” “Shales” and “Marls” from the Nagra Samples. Brine is used to improve DC coupling through the sample. Across the entire frequency range shales have the highest conductivity closely followed by the marls but the carbonates have a much lower conductivity. .... 78

Fig. 4-34: CSIRO 16 mm coaxial transmission line cell. Small coaxial samples of solid rocks are specially prepared for the cell, but more typically the cell is used for analysing drill cuttings which are packed into the coaxial volume after being prepared as a fine powder or a paste. .... 79

Fig. 4-35: Dielectric and conductivity measurements of the samples NAGRA-G, H, I and SCR04. The samples were prepared as powders and then tested using the 16 mm coaxial transmission line cell. The dielectric response reduces almost perfectly linearly with an increase in frequency. Samples G and I are particularly similar and they are also generally categorized as “shales according to their XRD response. Nagra H is categorized as a carbonate according to XRD data and it has the lowest dielectric response of all the samples tested. The conductivity generally increases with increasing frequency which indicates that polarisation loss  $\epsilon''$  is significant. .... 80

Fig. 4-36: Photograph of the end-loaded transmission line probe. .... 81

Fig. 4-37: The (a) dielectric and (b) conductivity measurements of a subset of the Nagra samples with the complete frequency range. The samples were prepared as pastes and then tested using the endloaded coaxial transmission line. The dielectric response of the samples is decreasing with frequency to a plateau value of approximately 30-40 at 1 GHz, which is much greater than the dry powder response but is expected because of the increased water content resulting from preparation. The conductivity is quite flat across the frequency range up to around 300MHz after which polarisation loss dominates the measurement. The (c) dielectric and (d) conductivity measurements of a subset of the Nagra samples as per Fig. 4-37a, with a zoomed in frequency range. .... 82

Fig. 4-38: (left) Comparison of real dielectric permittivity at 10 MHz measured using endloaded transmission line measurement on paste prepared from the preserved sample against a cling film coupled measurement on the preserved sample. Generally we see that the endloaded paste measurement is higher than its equivalent glad coupled parallel plate measurement on a preserved sample, but this is consistent with the additional water present in paste sample. The correlation is not particularly strong. (right) Comparison of the water content in the paste sample with the water content in the original preserved sample determined using NMR. We also observe that the water content of the paste (typically 20 – 35 % by mass) exceeds the water content of the preserved sample (typically 1 - 7 % by mass). .... 83

Fig. 4-39: This is an attempt at converting a preserved measurement into a paste measurement. The initial preserved sample dielectric response is increased by an amount calculated from the increase in moisture and CEC. The results demonstrate a very strong 1-to-1 correlation can be achieved and therefore we can substitute the ease of a paste style measurement for the quality of a preserved style measurement. .... 84

Fig. 4-40: Typical ultrasonic signal transmitted between two P-wave transducers through a cylindrical rock plug in the axial direction (plug extracted from the core NAGRA-B). The pink line corresponds to the trigger signal. .... 85

Fig. 4-41: Typical ultrasonic signal transmitted between two S-wave transducers through a cylindrical rock plug in the axial di. rection (plug extracted from the core NAGRA-B). The pink line corresponds to the trigger signal. .... 86

Fig. 4-42: Relationship between water content averaged from the three NMR methods (% from the Table 4-1) and the velocities ( $V_p$ - $V_s$ ) as well as grain density derived from NMR water content on all the NAGRA collection. .... 87

Fig. 5-1: The correlation observed between equivalent imaginary dielectric permittivity and  $V_p$ . The data presented covers the decadal incremental spot frequencies from 1 MHz to 1 GHz. The permittivity is measured on the paste sample prepared by drying and crushing preserved rock. The  $V_p$  measurement is performed directly on a preserved rock plug. We observe a strong negative correlation between  $V_p$  and the equivalent imaginary dielectric response of the powdered sample ( $V_p$  decreases as the equivalent imaginary dielectric response increases) and typically the correlation improves very slightly as the frequency is increased. .... 90

Fig. 5-2: The correlation observed between real dielectric permittivity and  $V_p$ . The data presented covers the decadal incremental spot frequencies from 1 MHz to 1 GHz. The permittivity is measured on the paste sample prepared by drying and crushing preserved rock. The  $V_p$  measurement is performed directly on a preserved rock plug. We observe a strong negative correlation between  $V_p$  and the real dielectric response of the powdered sample ( $V_p$  decreases as the equivalent imaginary dielectric response increases) and typically the correlation is better at low frequencies and reduces quite rapidly as the frequency exceeds 100 MHz. The optimum correlation occurs at 10 MHz. .... 91

Fig. 5-3: The correlation observed between specific surface area and real dielectric permittivity for all of the spot frequencies. A strong positive correlation is observed (SSA increases with an increase in dielectric response), but the correlation is strongly reduced above 100 MHz. The optimum frequency to observe this correlation is at 10 MHz where the correlation is  $R^2 = 0.9324$ . .... 92

Fig. 5-4: The correlation observed between specific surface area and equivalent imaginary dielectric permittivity for all of the spot frequencies. The SSA shows a strong positive correlation with the equivalent imaginary dielectric permittivity better than  $R^2 = 0.81$  for all frequencies, but unlike the real dielectric permittivity the correlation improves slightly as the frequency is increased. At 1 GHz the correlation is  $R^2 = 0.9206$ . .... 93

Fig. 5-5: (left) The high swelling clay content shale powder (clay platelets marked in orange) and (right) the low swelling clay content powder. In each case the water that is added (volume marked in light blue) to the sample form droplets between the disaggregated grains but the swelling clay retains a significant quantity of moisture in the interlayer volume. Ions occurring in the water form more easily in high SSA minerals and have a more pathways through which to conduct. We expect some of these ions to be free to migrate through the sample by hopping in and out of the platelets and into the free water. We also expect some of the ions to be less free to migrate and be constrained on the surfaces of the grains or within the interlayers. As such, the ions provide a dual role, participating in both conduction and polarisation and there real and equivalent imaginary dielectric permittivity. .... 94

Fig. 5-6: Dielectric responses of a selected subset of the paste samples (Top and Top Inset) the real dielectric response, (Bottom) the equivalent imaginary dielectric response and (Bottom Inset) the conductivities. The samples have been selected to show how typical dielectric responses of shales are related to their SSA. The real dielectric response reduces with frequency to a plateau value of approximately 30 -40 but the real dielectric permittivity at 1 MHz is approximately 1 order of magnitude higher than the high frequency plateau. The real dielectric permittivity below 100 MHz is ordered according to SSA, with an increased SSA leading to an increased dielectric permittivity. In the frequency range between 100 MHz and 1 GHz the separation according to SSA is lost and it is apparent that the high frequency real dielectric permittivity is governed by other processes. Likewise the equivalent imaginary dielectric permittivity exhibits a simple downward 1-to-1 trend in frequency space which is consistent with conduction dominated loss, and is supported by the inset conductivity response. At above 100MHz the polarisation loss mechanisms begin to appear, but don't dominate equivalent imaginary dielectric permittivity until beyond 1 GHz. .... 95

Fig. 5-7: There is reasonable positive correlation between the real dielectric permittivity and the % water content in the sample at 100 MHz ( $R^2 = 0.8225$ ). But the correlation become considerably worse as the frequency is increased from 100 MHz to 1 GHz..... 97

Fig. 5-8: The correlation observed between specific surface area determined by direct measurement in the laboratory using the EGME and the cation exchange capacity CEC determined during XRD analysis using tetra sodium pyrophosphate method. A strong positive correlation between SSA and CEC is observed ( $R^2 = 0.9303$ ). .... 98

Fig. 5-9: The variation in cation exchange capacity versus real dielectric permittivity determined using endloaded paste measurement as the frequency is increased. Both measurements are done on samples prepared from a dried crushed preserved rock. We observe a strong positive correlation between CEC and endloaded real dielectric permittivity on the paste, but this correlation breaks down rapidly beyond 100 MHz. .... 99

Fig. 5-10: Moisture within the preserved sample determined from NMR at 2 MHz versus (Left) The specific surface area determined after drying cleaning and crushing and (Right ) the cation exchange capacity. The % water retained in the preserved sample shows a strong positive correlation with both the SSA ( $R^2 = 0.868$ ) and the CEC ( $R^2 = 0.8252$ ). .... 100

Fig. 5-11: The relationship between the moisture content determined from NMR on the preserved sample versus the endloaded dielectric permittivity of the paste samples. The data presented covers the decadal incremental spot frequencies from 1 MHz to 1 GHz. The data show a strong positive correlation which breaks down rapidly above 100 MHz. .... 101

Fig. 5-12: Mineralogy analysis on each NAGRA plugs (Top) with comparisons of carbonates and water content from NMR (%) and velocities (m/s)..... 103

# 1 Introduction

## 1.1 Background and scope

CSIRO Earth Science and Resource Engineering was requested by NAGRA to perform a broad laboratory characterization of rock cores recovered from the well SLA-1 located in Schlattingen (Switzerland). Fifteen (15) preserved cores in total have been sent to CSIRO (see details in the following section; Appendix B). All cores were X-ray CT scanned. Five (5) cores, namely SCR01 to SCR05, were tested using the scratching method to determine the unconfined compressive strength (UCS) as a function of depth. Three (3) plugs with dimension  $D = 38\text{mm}$  and  $L = 76\text{mm}$  were sub-cored from the lower ends of cores SCR01 to SCR03 to perform unconfined uniaxial stress loading to failure and directly determine their UCS. One plug was sub-cored from the lower end of SCR04 and subjected to the Fast Tracked Petrophysics testing workflow. One plug was sub-cored from the lower end of SCR05, X-ray CT scanned and subjected to NMR characterization. The ten (10) remaining cores, namely BD3, BD5, BD9, BD10, BD32, BD37, PEM (835.62m), EMPA (886.60), EMPA (929.86) and PEM (946.08), were sub-cored and all plugs subjected to the Fast Tracked Petrophysics workflow. Table 1-1 summarizes the data associated with the rock cores received by CSIRO.

On the occasion of a status review in December 2011, a comparison was conducted of CSIRO's semi-quantitative XRD measurements and Nagra's own mineralogical analyses on other core samples from the same borehole section of the Schlattingen SLA-1 well (Mazurek 2011). The comparison displayed marked deviations in clay mineral content of several CSIRO samples when compared with the samples from Nagra. In regards of these apparent discrepancies and the recent access to new parameters at CSIRO such as Cationic Exchange Capacity (CEC) from Methylene Blue method, XRD clay analysis using a PANanalytical diffractometer and Specific Surface Area (SSA) from ethylene glycol monoethyl ether method, an extension of the previous contract was proposed. The extension re-addresses the previous results on mineralogy and dielectrics and adds new results on exact amounts of different clay types available in each of the SLA-1 core to properly define the rock types between carbonates, marls and shales. The new XRD results reduced the uncertainties associated with the semi-quantitative XRD measurements. The remaining minor differences between Nagra's own analyses and the CSIRO measurements (CSIRO sample ID "H") can be attributed to the small scale spatial variability of the clay mineral content.

We have also added a significant amount of dielectric data which correlate very strongly with much of the mineralogical and textural information gathered so far. We have verified the NAGRA reported mineralogy for all of the samples provided except for Sample-H which has been identified as a carbonate with a total carbonate content of 87%. SSA for the SLA-1 samples typically ranges from  $\sim 10$  to  $\sim 120\text{ m}^2/\text{g}$  and this is consistent with the mineralogy from XRD. In fact determination of the analytical SSA, using published values of the SSA for the constituent minerals gives a 93% correlation with a close to 1-to-1 relationship.

Excellent correlations appear between dielectrics, CEC and SSA using paste samples, which suggests that mineralogy alone is the principal determinant. Surprisingly, this also applies to  $V_p$ , which would normally be considered as a texturally-controlled parameter. It is found to correlate strongly (up to approximately 86%) with dielectric response determined from paste, which has a significant portion of its textural quality destroyed during preparation. Ions occurring within the shale samples are the dominant cause of both real and equivalent imaginary dielectric permittivity below 100 MHz through Maxwell-Wagner processes and conduction. Above 100 MHz however, the mineralogy and water content dominate the measured dielectric response. This is also consistent with a realistic petrophysical shale model established from high resolution imaging. Paste measurement gives better correlations with textural and mineralogical

properties than intact preserved shale measurement, although a simple correction based on CEC and water content can convert the preserved measurement into an equivalent paste measurement with nearly 97% correlation. This important relationship is a critical first step in establishing drill cutting based formation evaluation and furthermore a dielectric log to SSA and CEC algorithm.

The new results lead the dielectrics method to a new level of interpretations: it proves to be a very accurate tool to assess the mineralogy control on P-wave velocities, CEC and SSA on rocks BUT also on cuttings without the needs of specific sample preparations or preservations.

Tab. 1-1: Summary of the rock cores received and tested by CSIRO (see Appendix B).

NAGRA Sample ID	CSIRO Sample ID	CSIRO coding	Depth (m)	Lithology type	Facies	Tests
SCR1	SCR1	CSRO-11-16	748.22-748.62	Marly carbonate	Effingen	ScT UCS
SCR2	SCR2	CSRO-11-17	770.03-770.44	Clay-rich marl	Parkinisoni-Wurtembregica	ScT UCS
SCR3	SCR3	CSRO-11-18	826.16-826.66	Sandy marl	Wedelsandsein	ScT UCS
SCR4	SCR4	CSRO-11-19	856.09-856.40	Claystone	Opalinus Clay	ScT Petro
SCR5	SCR5	CSRO-11-20	801.53-801.93	Clay-rich marl	Blagdeni	ScT
BD3	A	CSRO-11-21	761.85-762.06	Clay-rich marl	Varians	Petro
BD5	B	CSRO-11-22	766.15-766.52	Clay-rich marl	Varians	Petro
BD9	C	CSRO-11-23	772.76-773.00	Clay-rich marl	Parkinisoni-Wurtembregica	Petro
BD10	D	CSRO-11-24	773.60-773.90	Marly carbonate	Parkinisoni-Wurtembregica	Petro
BD32	E	CSRO-11-25	812.59-812.86	Claystone	Wedelsandsein	Petro
BD37	F	CSRO-11-26	826.72-827.00	Marly carbonate	Wedelsandsein	Petro
MARKE D PEM	G	CSRO-11-27	835.62-835.89	Claystone	Murchisonae/ Opalinus Clay	Petro
EMPA	H	CSRO-11-28	886.60-886.88	Sandy claystone	Opalinus Clay	Petro
EMPA	I	CSRO-11-29	929.86-930.10	Sandy claystone	Opalinus Clay	Petro
MARKE D PEM	J	CSRO-11-30	946.08-946.37	Sandy claystone	Opalinus Clay	Petro

In Table 1-1, ScT stands for scratch testing; UCS for uniaxial stress loading for determination of the unconfined compressive strength; and Petro for the Fast Tracked Petrophysics testing workflow.

## 1.2 The geothermal well Schlattingen SLA-1

The geothermal well Schlattingen-1 (SLA-1) is located on the road between Basadingen, Schlattingen and Diessenhofen (Canton Thurgau) about 10 km south-east of the town Schaffhausen (approx. N 47°40'41.7", E 8°45'42"; 416.6 m asl) in the Northeastern part of the Swiss Molasse Basin (Figure 1-1). The borehole is intended to produce geothermal energy for an economical and CO<sub>2</sub>-emission-free operation of greenhouses. Therefore, during 2011, a first deep borehole Schlattingen-1 was drilled to use the ground water from aquifers in the Upper Muschelkalk and the transition Mesozoic / permo-carboniferous - crystalline rocks. The borehole reached a final depth of 1508 m, passed through the Quaternary, Tertiary, Jurassic and Triassic sediment sequence (with marls, silt-, sand-, and claystones, limestones) and finally encountered the crystalline basement.



Fig. 1-1: Topographic map, displaying the location of the geothermal well Schlattingen-1 (SLA-1).

The drilling of borehole Schlattingen-1 was accompanied by an extensive site characterization program, including litho-stratigraphic and structural mapping of drillcores in the clay-rich Mesozoic sequences, geophysical logging, hydraulic packer testing, water sampling and hydraulic fracturing stress measurements (Albert et al. 2012). Focus of the investigations was on the characterization of the candidate host rock formations, namely the Effingen Member, the so-called 'Brown Dogger' (stratigraphic sequence of Callovian, Bathonian and Bajocian age) and the Opalinus Clay. The stratigraphic profile of borehole Schlattingen-1 is shown in Figure 1-2, available technical borehole data are summarized in Table 1-2.

Geothermal Well Schlattingen-1					
Stratigraphy	Depth	Lithology	Thickness [m]	Unit	
Quaternary	53		53	Quaternary	
NEOGENE	125		72	Upper Marine Molasse (OMM)	
				PALEOGENE	364
Oligocene					
	Eocene				
JURASSIC	491		2	Bohnerz-Formation	
	Malm	Kimmeridgian	549	58	Plattenkalk
			643	94	Massenkalk/Quaderkalk
	Oxfordian	674	31	Mittlere Malmmergel	
		720	46	Wohlgeschichtete Kalke	
	Dogger	Aalenian	733.1	13.1	Hornbuck-Schichten
			757.8	24.7	Effingen Beds Birmenst. Sch., Glaukonit-Sandmergel
			804.6	46.8	Anceps-O., Macroceph.-Sch., Varians-Sch. Parkinsoni-Württembergica-Sch. Subfurcaten-Ool., Blagdeni-Sch., Humphriesi-Sch.
			831.4	26.8	Wedelsandstein-Formation
			949.7	118.3	Opalinus Clay
	Liassic	949.7	53.3	Jurensis-Schichten – Psiloceras-Schichten	
	TRIASSIC	Keuper	1003	44	Knollenmergel, Stubensandstein-Fm., Bunte Mergel, Gansinger Dolomit, Schilfsandstein
			1047	65	Gipskeuper Lettenkohle
1112			33.3	Trigonodus-Dolomit	
Muschelkalk		Upper	1145.3	24.2	Hauptmuschelkalk
		Middle	1169.5	53	Dolomit der Anhydritgruppe Anhydritgruppe (Sulfatschichten)
Buntsandstein		Lower	1223	29	Wellengebirge
		1251	10	Buntsandstein	
PALEOZOIC	Permian	1261	78	Rotliegendes	
	Crystalline	1339	169	Gneiss	
Total depth		1508 m			

Fig. 1-2: Stratigraphy of the geothermal well Schlattingen-1 (SLA -1) after Albert et al. (2012).

Tab. 1-2: Important technical borehole information about the geothermal well Schlattingen-1 (see also Albert et al. 2012).

Geothermal Well Schlattingen-1 – SLA 1	
Location	Village of Schlattingen, around 10 km south-east of Schaffhausen
Co-ordinates	N 47°40'41.7", E 8°45'42"
Elevation	416.6 m asl
Max. depth:	1508.0 bg
Drilling techniques	Percussion drilling, cuttings:           0 - 725 m bg 989 - 1116 m bg 1185 - 1508 m bg Single barrel core drilling:           725 - 989 m bg 1116 - 1185 m bg
Investigation programme	Petrophysical logging (GR, FEL, DIL, DLL, Gamma-Gamma, Neutron-Neutron, Sonic) Core mapping and structural logging (ABF, ABI) Packer Testing (4 Tests) Hydrofracturing (15 Tests) Porewater sampling (4 Samples) Mineralogical and geotechnical characterization of core samples (> 50 samples tested)



## 2 Cores X-ray characterization

Cores and plugs images were acquired with a Toshiba Xspeed medical scanner operating at 120kV generating X-rays within an energy band of 20 to 60keV. Current level was set at 150 and 200mA for the slice and the view modes, respectively. Exposure time was set to 3s. The field of view was fit to the diameter of the core/plug under investigation. The whole core sections, still sealed in their plastic liner were first screened using the view/scanogram mode, i.e., 2D projection radiographs. This showed the presence of fractures, millimetre scale heterogeneities, and bedding orientation. Based on this preliminary imaging, the coring plan was established, i.e., plugs location and orientation in each core selected. The sub-cored plugs are stored in glass vials filled with *Ondina 68* oil. For display purposes, the 16-bit images acquired, with each pixel assigned a CT number in Hounslow units are converted into 8-bit images. The greyscale in these images is adjusted to highlight the layering, fractures and and other heterogeneities with good contrast.

The scanograms of cores SCR01 to SCR05 are shown in Fig. 2-1; and those of cores A to J are shown in Fig. 2-2. Most cores seem reasonably well preserved, although few fractures along the bedding plane appear in cores SCR04, C, D and J (hairline thickness). However, these fractures were not detrimental for plug sub-coring.

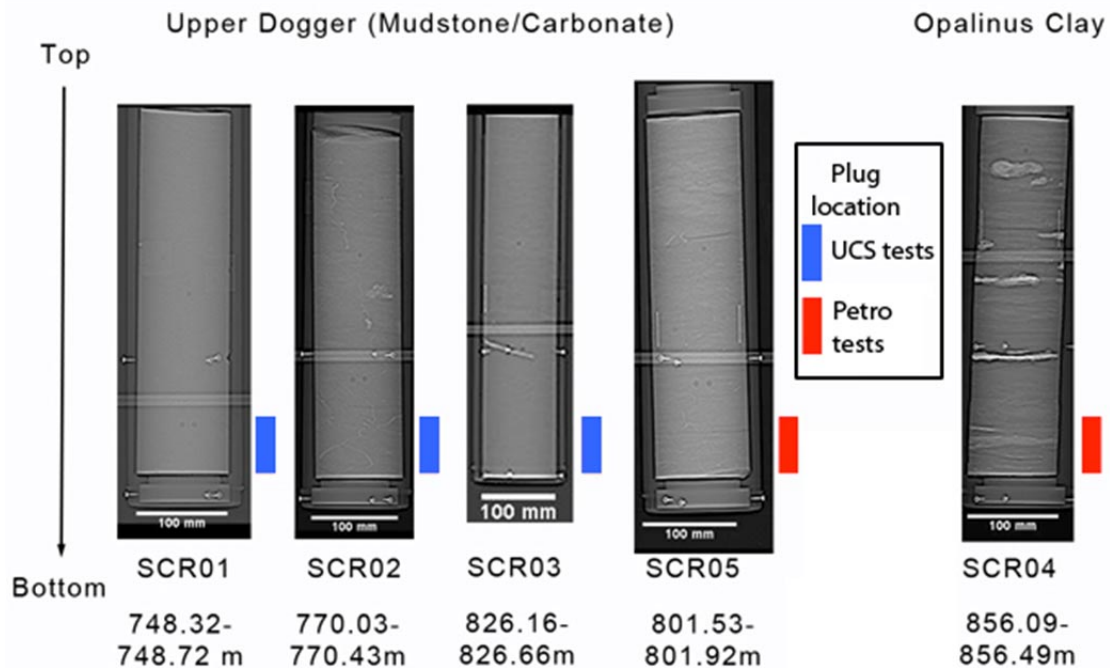


Fig. 2-1: X-ray CT scanograms of the cores used for scratch testing (SCR01 to SC05). Blue rectangles stand for the three plugs extracted for uniaxial stress testing, whereas red rectangles stand for the plugs extracted for Fast Tracked Petrophysic testing workflow. Note that the bright horizontal stripe that appear on the images are artefacts related to the plexiglass couch where seat the cores to maintain them in a horizontal plane.

Transversal CT slices were acquired every 1cm from the top to the bottom of each core (see Figures in the file CTscan/wholecore\_slice\_montage) to evaluate the occurrence in 3D of features such as fractures, laminations, heterogeneities etc. An example of such slice montage is given in Fig. 2-3 for core SCR04. The white patches are most probably carbonate concretions from diagenetic processes or carbonate rich lithoclasts with sometimes centimetric sizes in the wholecore SCR04, I and E. Some cores present enrichment in fossils-lithoclasts from millimetric to centimetric sizes in cores A, D and SCR05. Most of the other cores are quite homogeneous with rare very bright spots corresponding to pyrite minerals (iron-sulfides,  $\text{FeS}_2$ ), or filling veins (cores C and F) or in thin local layers/lenses (Core E, G and J) occurring when diagenetic fluids were active in these particular layers. Note in core H that half of the core is dark and the other half is brighter which is the signature of a drastic change in the sedimentary history. The bright part shows some patches of diffuse carbonates which could support a change in the fluid transport history and/or chemistry due to a change in the tectonic conditions or local stresses.

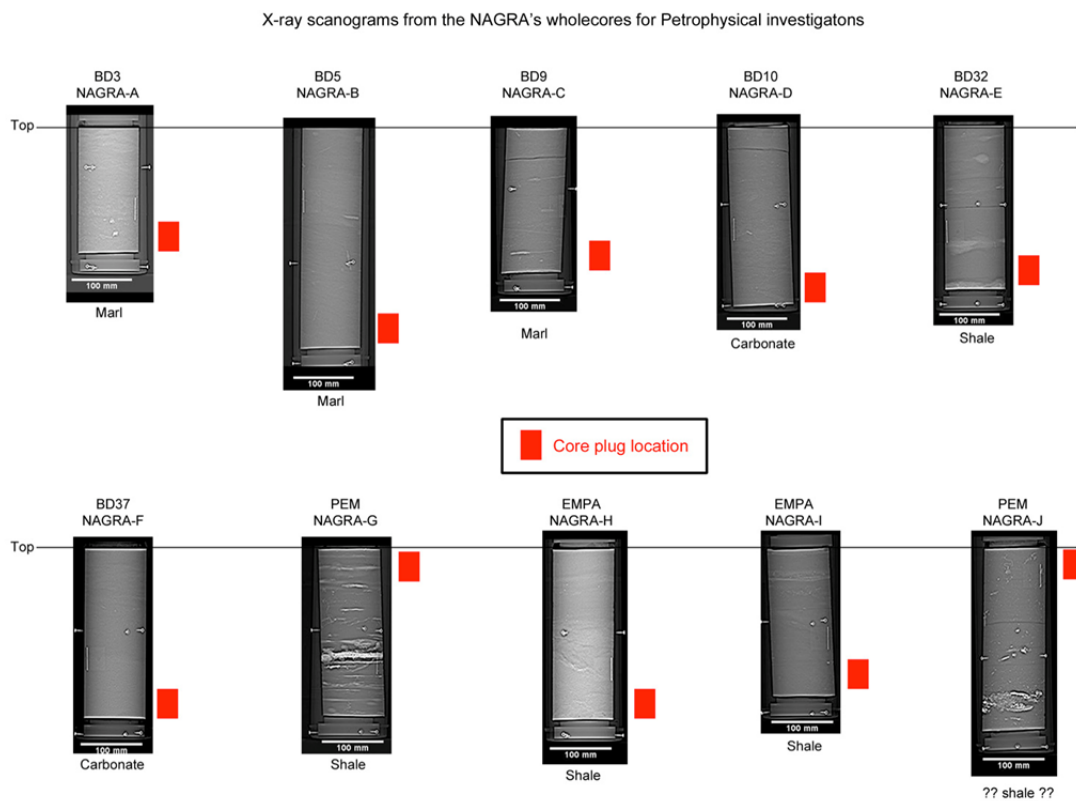


Fig. 2-2: X-ray CT scanograms of the cores used for the Fast Tracked Petrophysic testing workflow.

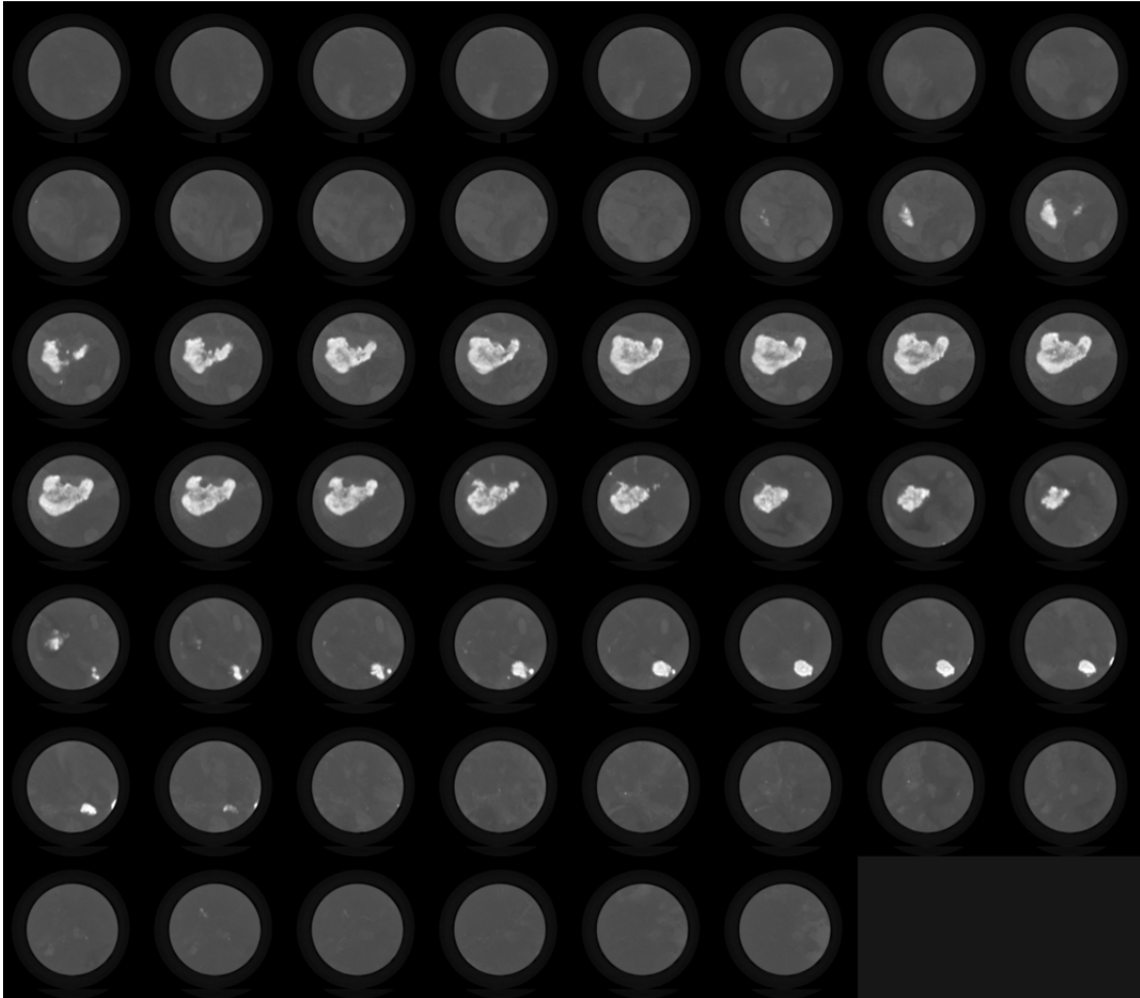


Fig. 2-3: Example of transversal CT slices acquired every 1cm along the core SCR04 from top to bottom.

All cores display occurrences of (i) dense patches with millimetre to centimetre size; (ii) dense layers with millimetre to centimetre thickness; and (iii) thin cracks or elongated veins. Some of them show a high density of lithoclasts, i.e., cores A, C and SCR05.

Plugs ( $D = 38\text{mm}$  and  $L = 55\sim 76\text{mm}$ ) were extracted from all cores following a new time-consuming procedure offering an almost 100% recovery rate. The sub-coring is performed in two steps: (i) a diamond wire saw is employed to obtain pseudo-cylinders with *Ondina 68* oil acting as a preservation/lubrication/cooling fluid; then (ii) a grinding of the lateral surface of the plugs is performed using a lathe to obtain the final cylindrical shape. In this last preparation step, the same oil is also used for preservation/lubrication/cooling. Eventually, the end faces of the plugs are trimmed to obtain flat, parallel surfaces.

All the plugs were extracted from the bottom (deepest) end of each core, except in cores G and J because of the presence of cracks at that location (Fig. 2-1 and Fig. 2-2). For these two particular cores, the plugs were sub-cored from the top (shallowest) end. Some discs of  $\sim 0.5$  cm thick were also prepared with flat parallel end faces for dielectric measurements. The off-cuts, discs and plugs were, at any stage, stored in glass jars filled with *Ondina 68* oil for preservation. The plugs/discs within the glass jars were subjected to X-ray scanning in three steps: (i)

scanograms (2D axial projections) were acquired; (ii) transversal/radial slices were acquired every 1mm along the plugs/discs axis; then (iii) two orthogonal axial slices were acquired (see example in Fig. 2-4; similar images for the other plugs can be found in the file CTscan/Plug\_CT\_slices). The aim of this procedure is to compare the size, spatial and orientation distributions of heterogeneities in the plugs and in the whole core. This can help the interpreter understand the various macroscopic measurements performed later on these plugs. The transversal/radial slices allow for a 3D reconstruction of the plugs/discs highlighting the size, spatial and orientation distributions of denser elements such as lithoclasts, carbonate patches or veins (see example Fig. 2-5; similar 3D analysis for the other plugs can be found in the file CTscan/Plug\_3D\_analysis). Note that heterogeneities occurring at the whole core scale previously described also appear at the plugs scale. The plug E is marked by occurrence of pyrite rich layer at the bottom and top of the plug recording the over-bright colors. The very shaly cores such as G and J only record isolated pyrites and more diffuse within layers in core E. The carbonate rich plugs are easily recognisable by their light colors with diffuse haloes-patches along the samples: Cores D, F and G are the best examples. Finally for the cores A, B and D, the fossils or lithoclasts seem to be rich in carbonates. The later cores record a kind of elongated tubes crossing the sub-layers from 3D extraction which recall bioturbation activities.

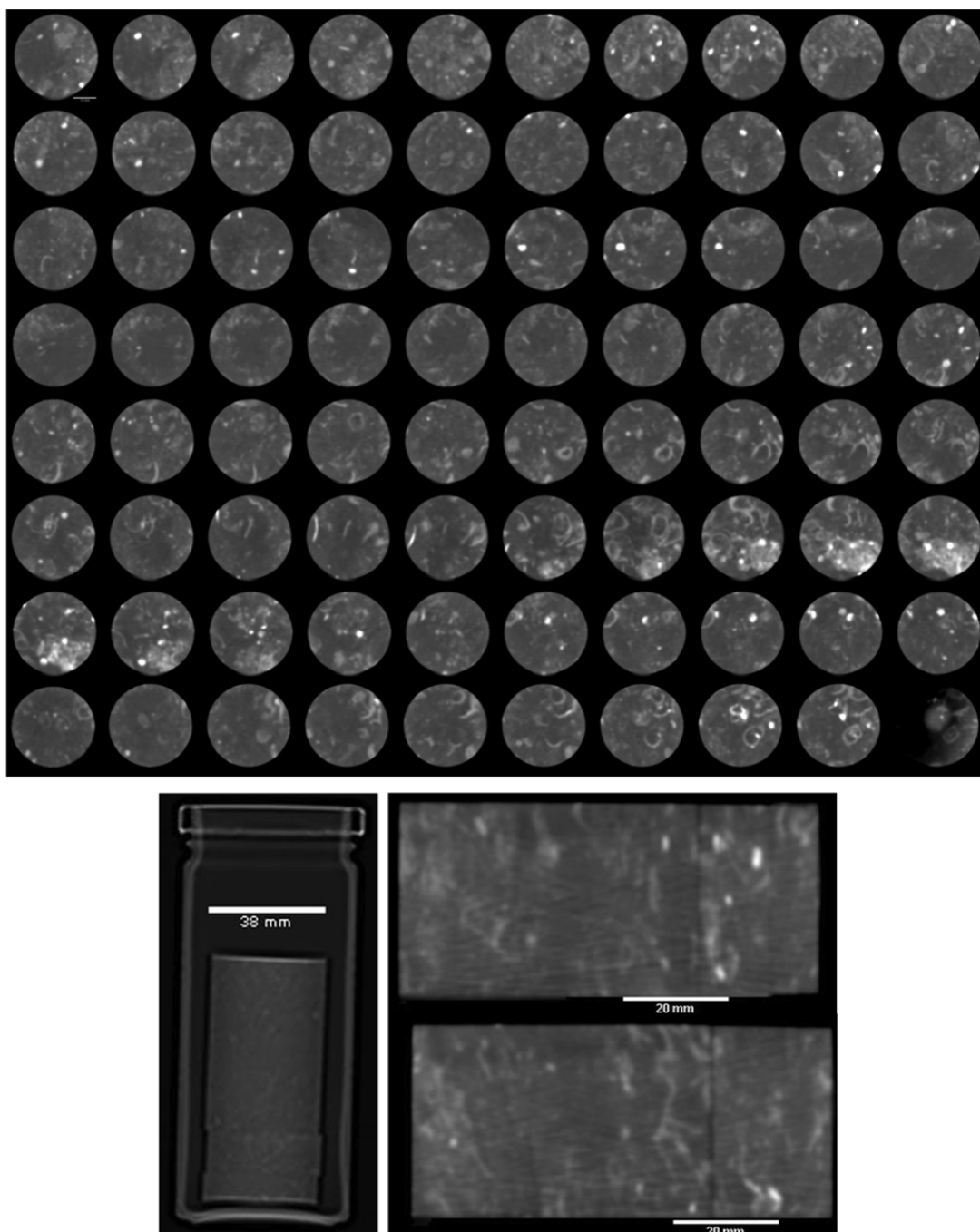


Fig. 2-4: Example of X-ray CT slice images obtained on the plug NAGRA-A extracted from the lowest (deepest) part of the core A. Note that the plug and discs used for dielectric and other petrophysical characterization appear in these scans.

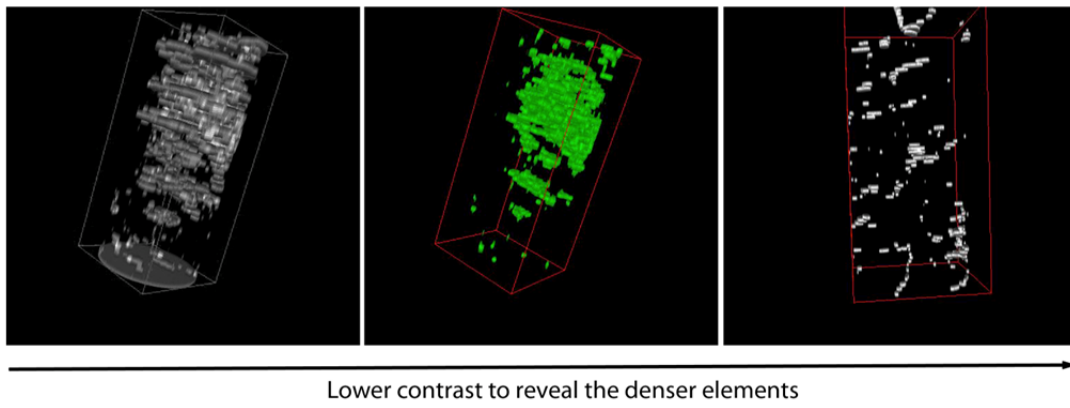


Fig. 2-5: Example of 3D high density map reconstructed from the CT slice images of the plug NAGRA-B extracted from the lowest (deepest) part of the core B.

### 3 Mechanical characterization

#### 3.1 Introduction

Scratch testing of rocks has been developed in the late nineties based on the early theoretical work of Detournay and Defourny (1992). It is an alternative to traditional triaxial deformation experiments aimed at determining the Mohr-Coulomb strength parameters of a rock. By scratching the surface of a rock with different depths of cut while measuring tangential and normal forces, strength parameters can be inferred. Advantages of the scratch testing method over the traditional method involving several single-stage triaxial tests (or single multi-stage triaxial test) include:

- A single rock sample is virtually required for the determination of the UCS and the internal friction angle. The scratch test is therefore not affected by possible heterogeneity between rock samples. It is also extremely useful when only little rock material is available due to the expensive nature of in situ core recovery operations;
- The scratch test is partially non-destructive as only a relatively shallow “groove” is engraved on the surface of the sample without modifying the rest of the rock material; it can therefore still be used for further testing of its other mechanical/physical/physical properties;
- Applied to inherently heterogeneous rocks, it can constitute a mean for assessing the degree of heterogeneity of a rock formation (e.g., on long cores);
- The scratch test is also much faster, and therefore cheaper, to perform than triaxial tests, especially for very low permeability rocks such as shales, i.e., few minutes on a single sample for the scratch test as opposed to several weeks per triaxial test, especially that several single-stage triaxial tests or a single multi-stage triaxial test are required to determine the two Mohr-Coulomb strength parameters.

The scratch test is currently promoted by oil/gas companies: it constitutes a mean for assessing the strength variation with depth on recovered cores. As a consequence at least two service companies have specialized in such testing (Epslog and Terratek), although it is usually not applied to shales but rather to reservoir rocks. Such data are part of geomechanical modelling and predictions workflows for borehole stability assessments for instance. In the mean time, attempts have been carried out for applying the scratching method to boreholes in situ rather than to recovered cores in the laboratory (Tan, 2008).

Unfortunately, due to the confidential nature of the scratch data acquired by the oil/gas industry, no published correlations with other mechanical/physical/physical properties are available in the open literature. However, the SHARC project includes a component dedicated to the acquisition of scratch test data on shales (a new application domain being developed within the project) and their correlation with the other acquired data types.

#### 3.2 Whole Core Scratching

The mechanical characterization part of this project was performed on the cores SCR01 to SCR05 (see Fig. 3-1). First, each of the five cores was scratched along its length with 4 different depths of cut using a sharp cutter. Then, a plug with dimension  $D = 38\text{mm}$  and  $L = 76\text{mm}$  was sub-cored from the lower (deeper) part of each of the cores named SCR01, SCR02 and SCR03. These plugs were subsequently subjected to an unconfined uniaxial loading until failure occurred. Young's modulus and Poisson's ratio were determined from the linear part of the stress-strain curve. The UCS of each plug was determined from the peak stress achieved near

the failure point. The aim of these uniaxial loading tests is to provide a calibration mean for the results obtained on the whole cores with the scratching method.

### 3.2.1 Principle

Cutting is defined as the process of tracing a groove of a constant cross sectional area along a free surface of the rock. Rock cutting consists of two processes: (i) pure cutting, occurring ahead of the cutting face of the tool and (ii) frictional contact, mobilised across the wear flat/rock interface (see Fig. 3-1).

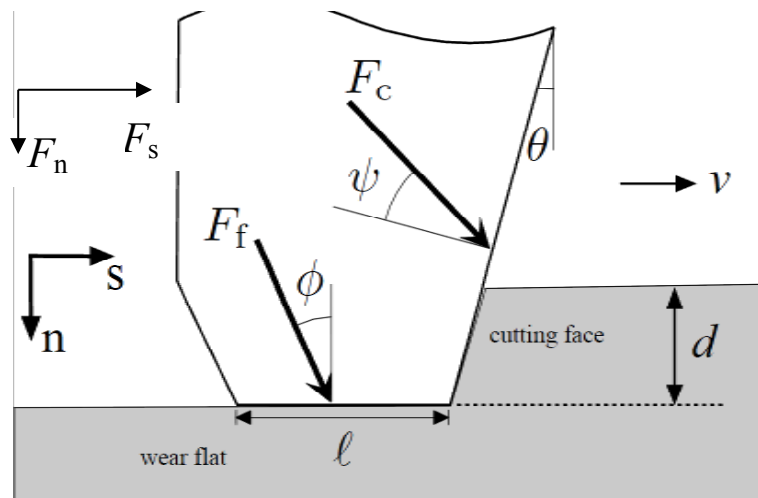


Fig. 3-1: Force decomposition of the cutting process (Detournay and Defourny, 1992)

A phenomenological model of rock cutting has been proposed by Detournay and Defourny (1992). The model is characterized by three parameters: (i) the intrinsic specific energy  $\varepsilon$ , (ii) the ratio of the vertical to horizontal force acting on the cutting face  $\zeta$  and (iii) the friction coefficient  $\mu$ . The total force  $\mathbf{F}$  acting on the cutter during the scratching is a sum of the force acting on the cutting face  $\mathbf{F}_c$  and the force acting on the wear flat  $\mathbf{F}_f$ . The horizontal/tangential (subscript  $s$ ) and vertical/normal (subscript  $n$ ) components of  $\mathbf{F}_c$  are thus expressed as

$$F_{cs} = \varepsilon A$$

$$F_{cn} = \zeta \varepsilon A$$

for a sharp cutter, where  $A$  is the cross sectional area of the groove being traced, i.e.,  $A = \omega d$  for a rectangular cutter of width  $\omega$  and  $d$  is the depth of the cut. The relationship between the components  $F_{fn}$  and  $F_{fs}$  is constrained by the coefficient of friction  $\mu$ , i.e.,

$$F_{fs} = \mu F_{fn}$$

By combining both pure and frictional cutting processes,  $F_{fs}$  can be expressed as

$$F_s = (1 - \mu\zeta)\varepsilon A + \mu F_n$$

and dividing by the cross section area  $A$ , the specific energy can be expressed as

$$E = E_o + \mu S$$

where the quantity  $E_o$  is defined as

$$E_o = (1 - \mu\zeta)\varepsilon,$$

the drilling strength  $S$  as

$$S = \frac{F_n}{A}$$

and the specific energy  $E$  as

$$E = \frac{F_s}{A}$$

Tests performed on various rocks using a sharp cutter show linearity between  $F_{cs}$  and  $wd$ . As evident in Fig. 3-2, the slope increases with increasing strength in the rock (from chalk to rhinestone). A strong correlation between  $\varepsilon$  and UCS is also evident in Fig. 3-3 based on numerous tests performed on various rocks.

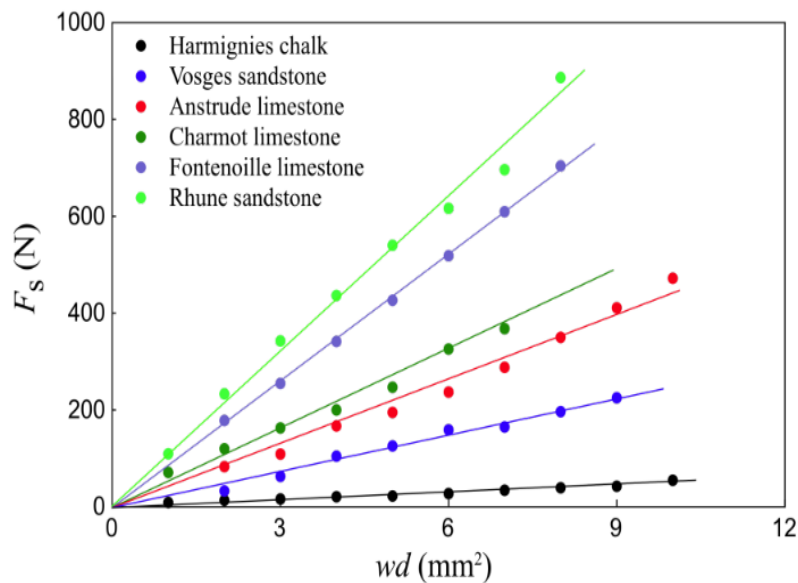


Fig. 3-2: Linearity between the tangential component of the force on the cutting face  $F_{cs}$  and the cross sectional area  $wd$  (Richard, 1999).

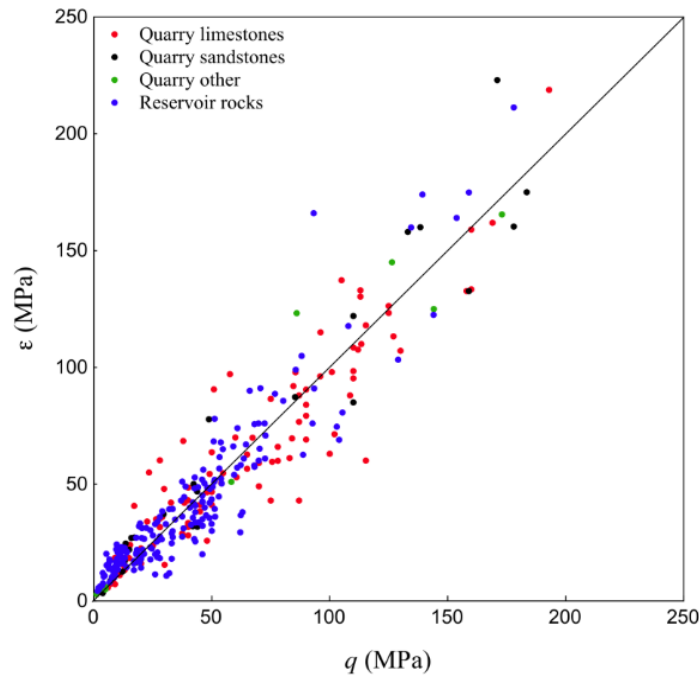


Fig. 3-3: Correlation between intrinsic specific energy  $\varepsilon$  and UCS (Richard, 1999).

### 3.2.2 Experimental Methodology

The apparatus (see Fig. 3-4) consists of a base, two orthogonal moving mechanisms, a cutting element, a holding bucket, a load sensor and a digital micrometer. The core frame consists of a horizontal and a vertical aluminium plate. A wheel fixed to a fine Archimedes screw allows precise adjustment of the vertical position of the cutter with respect to the rock sample holder. The cutter is fixed onto a load sensor and the vertical position of the cutting tool can be adjusted by rotating the wheel. A digital micrometer displays a read out of the vertical position of the cutter with respect to the rock sample holder. A stepper motor/gearbox mechanism allows the rock sample holder to move horizontally. During a given scratching, the depth of cut is therefore constant. The present configuration of the motor output torque and gear box ratio 1:15 allows a motion of the cutter at a constant velocity of 4 mm/s against a horizontal force up to 3000 N.

The measurement of forces acting on the cutter during the scratching is performed using a strain gauges type load sensor. The load cell offers the following features: (i) virtually uncoupled measurement of the vertical and horizontal components of the force; (ii) a high sensitivity (less than 1 N) over a large range (0 to 4000 N); and (iii) a high vertical and horizontal stiffness that limits the error on the depth of cut. The overall precision and resolution of the force measurement is about 1N. For a cutting velocity of 4 mm/s, a 100 Hz acquisition frequency is equivalent to a spatial resolution of 25 force measurements per millimetre. A software coded in *Labview* environment provides a graphical interface that enables the control and force data recording of the test.

An experimental procedure for using the Wombat apparatus has been established in order to evaluate the strength properties of a rock specimen. Based on this procedure, an adapted experimental procedure has been developed for shales, taking into account their peculiar properties.

As shown in Fig. 3-4, one end face of the plastic core housing is dry cut with a diamond saw. Subsequently, the lateral surface of the housing is cut, with a similar protocol, along the core axis in order to free the shallowest lateral surface of the rock cylinder. The freshly cut surface is right away covered with oil and wrapped in a plastic film. Each core is then set on the Wombat's sample holder for the surface to be scratched. Four subsequent scratch runs, with constant depth of cut using a sharp cutter, are performed at  $d = 0.1\text{mm}$ ,  $0.2\text{mm}$ ,  $0.3\text{mm}$  and  $0.4\text{mm}$ . During each scratch run, tangential/horizontal and normal/vertical forces,  $F_s$  and  $F_n$ , respectively, are recorded together with the abscissa along the rock core. The total time of scratching is less than 20min.

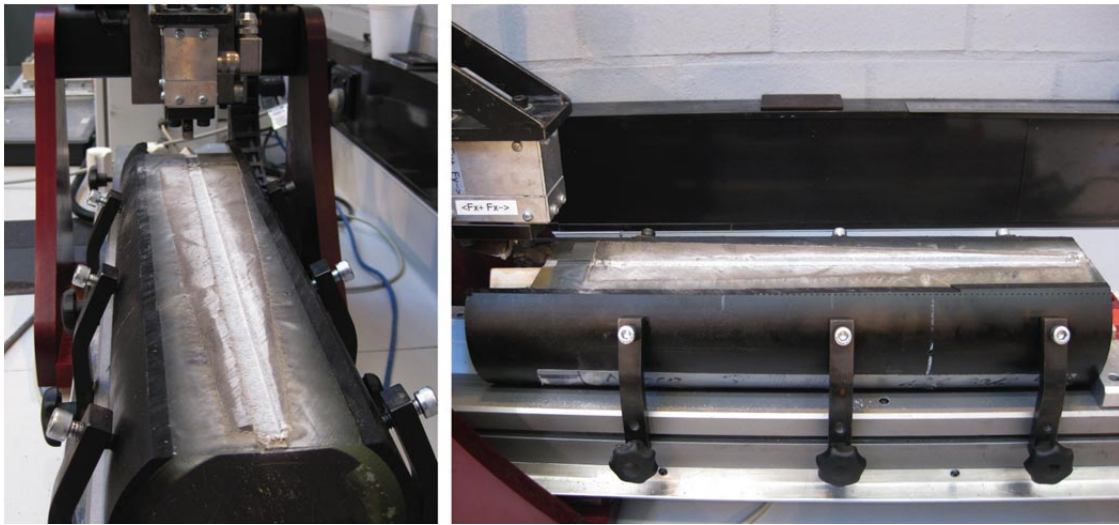


Fig. 3-4: Experimental setup: Scratch test apparatus, also known as the *Wombat*.

### 3.2.3 Results

For each of the cores SCR01 to SCR05, Fig. 3-5, Fig. 3-7, Fig. 3-9, Fig. 3-11 and Fig. 3-13 display, for the four depths of cut, (i) the tangential/horizontal force  $F_s$  recorded on the total length of the core (top plot); (ii) the tangential/horizontal force  $F_s$  recorded only on a selected length where no boundary effects associated with the edges of the rock core appear (middle plot); and (iii) the averaged tangential/horizontal force  $F_s$  along the selected length (bottom plot). The tangential/horizontal force  $F_s$  recorded along the core for each depth of cut is averaged using the moving average method, with a moving window spanning over 10mm. Within a given averaging window, the four average tangential/horizontal forces  $F_s$  obtained for the four depths of cut are fitted with a linear regression model. The slope of this model is the local intrinsic energy of the rock within the moving window. Divided by the width of the cutter, the intrinsic energy yield the local specific intrinsic energy of the rock, which corresponds to the local strength (UCS) of the rock.

Therefore, for each of the cores SCR01 to SCR05, Fig. 3-5, Fig. 3-7, Fig. 3-9, Fig. 3-11 and Fig. 3-13 display the final result of the scratch tests which consists of a log of the UCS in terms of the actual depth of recovery of the rock core. Superimposed on each UCS log, scanograms of the core before testing and pictures of the core after testing are also displayed (to scale) for qualitative comparison purposes. There is reasonable agreement between the variations in strength as evidenced by the scratch test results and the heterogeneities observed in the pictures and scanograms.

Specifically for each of SCR01 to SCR03, a plug has been sub-cored from the lowest end (deepest end) of the core for further unconfined uniaxial load testing (see following section). Pictures of these plug are also shown in Fig. 3-5, Fig. 3-7 and Fig. 3-13 for comparison purposes.

The results of the scratch tests are presented in Table 3-1 in terms of mean values and standard deviation of UCS  $\sigma_{\text{UCS}}$ . Separate calculations are performed for the core sections, which correspond to the sub-cores intended for UCS testing. This allows for an easy comparison of the scratch test results with the UCS tests.

Tab. 3-1: Summary of the results of the scratch tests on the cores SCR1 – SCR4. Arithmetic mean and variance are calculated for the entire core length and for the core sections, which correspond to the sub-cored plugs.

	SCR1	SCR2	SCR3	SCR4	SCR5
Entire core length					
UCS <sub>arithmetic mean</sub> (MPa)	62.2	53.0	63.3	43.0	52.3
$\sigma_{\text{UCS}}$ (MPa)	10.3	9.7	6.4	9.3	5.4
Core section corresponding sub-cored plugs (UCS tests)					
UCS <sub>arithmetic mean</sub> (MPa)	60.7	51.1	58.9	N/A	N/A
$\sigma_{\text{UCS}}$ (MPa)	7.0	2.8	4.2	N/A	N/A

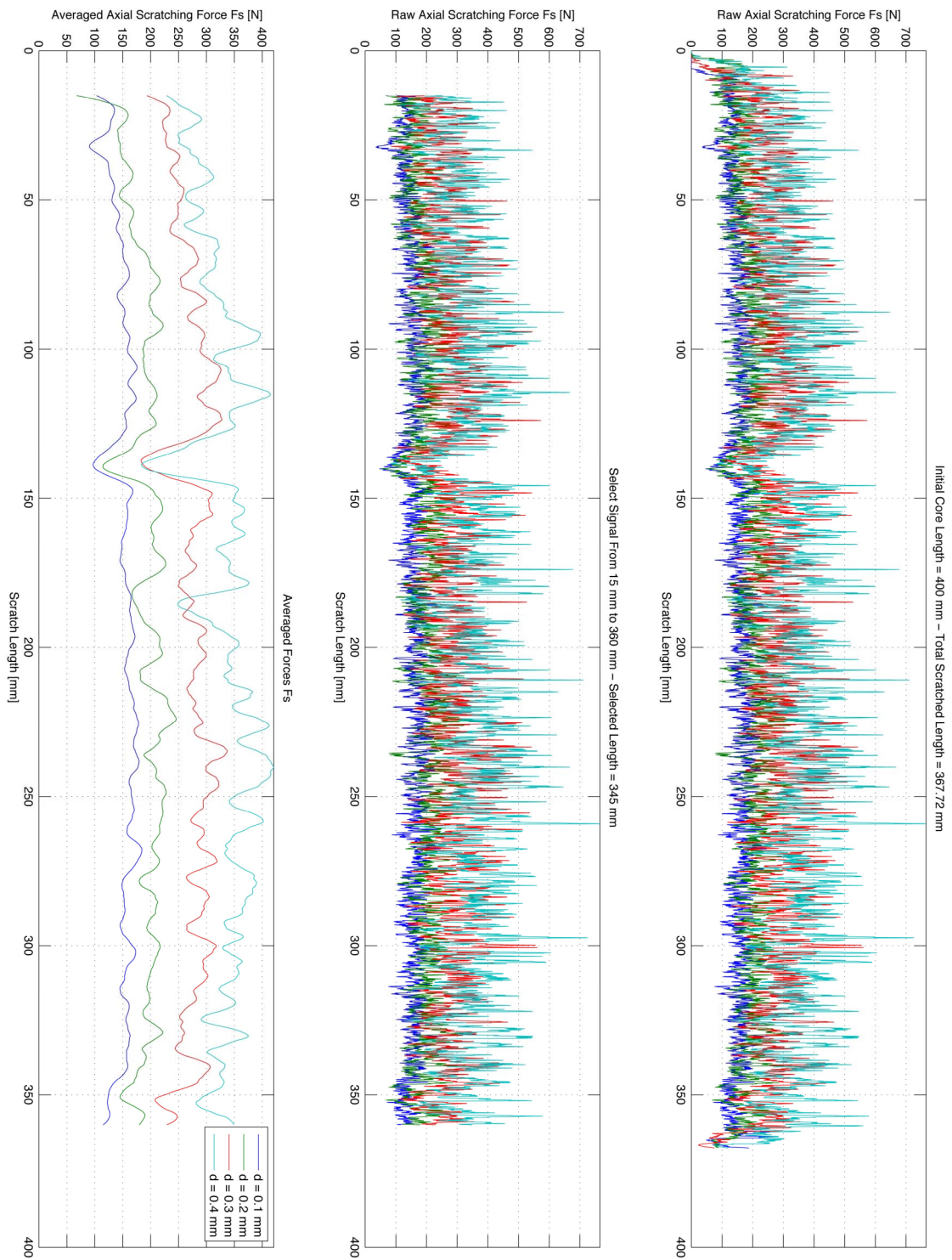


Fig. 3-5: SCR01. Scratch test results: Four depths of cut have been used. The core has been scratched from top to bottom (right: original data; middle: cut-off of edge effects; left: moving average).

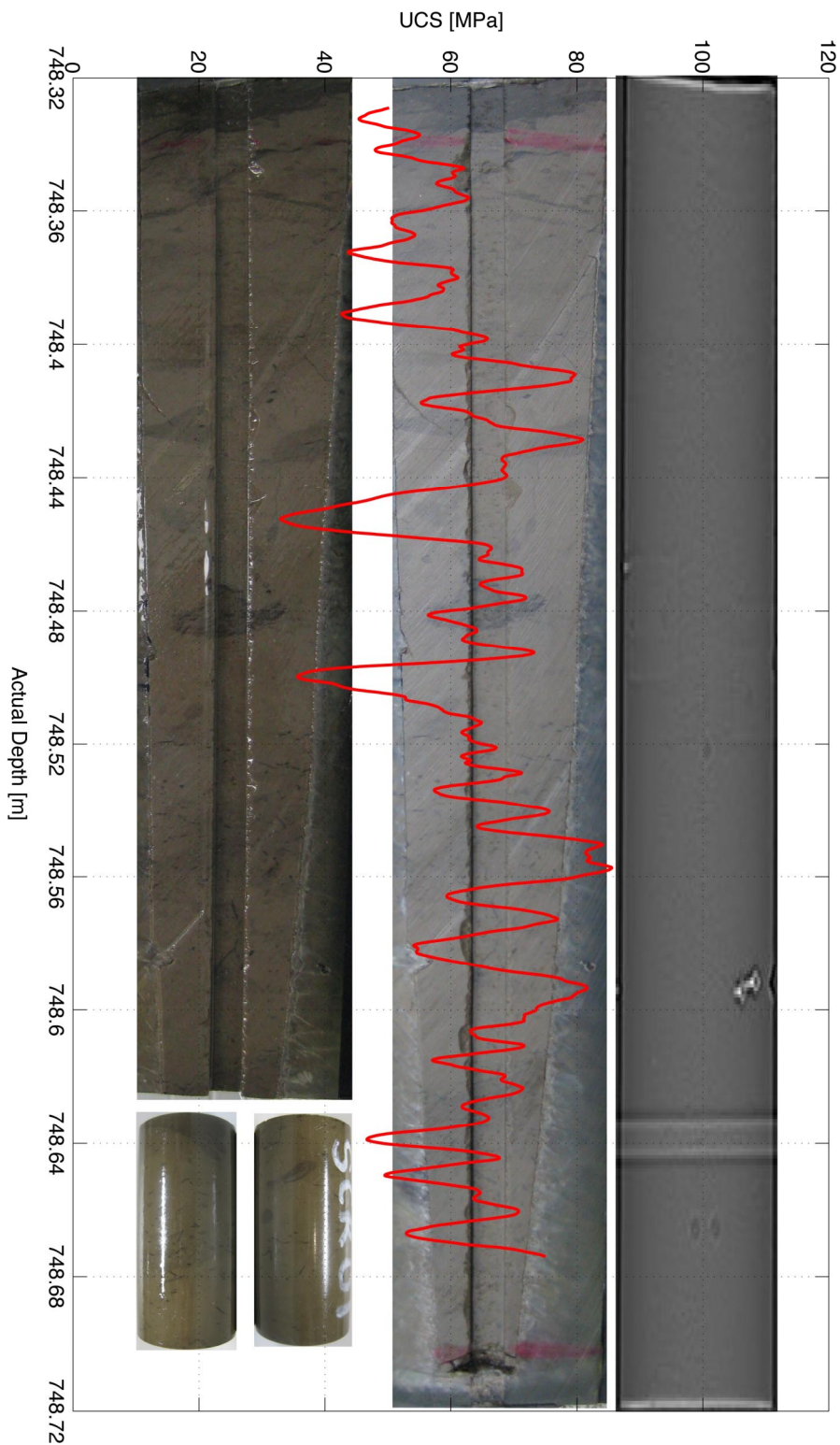


Fig. 3-6: SCR01. Unconfined compressive strength log (UCS log). The data for this test can be found in a digital form in the file Scratch-SCR01.xls. Note, the horizontal stripe in the CT scan at 748.64 m images the fixation of the core sample. The little nodule at 748.6 m exhibits a carbonate spot which may give rise to the enhanced UCS value at this location.

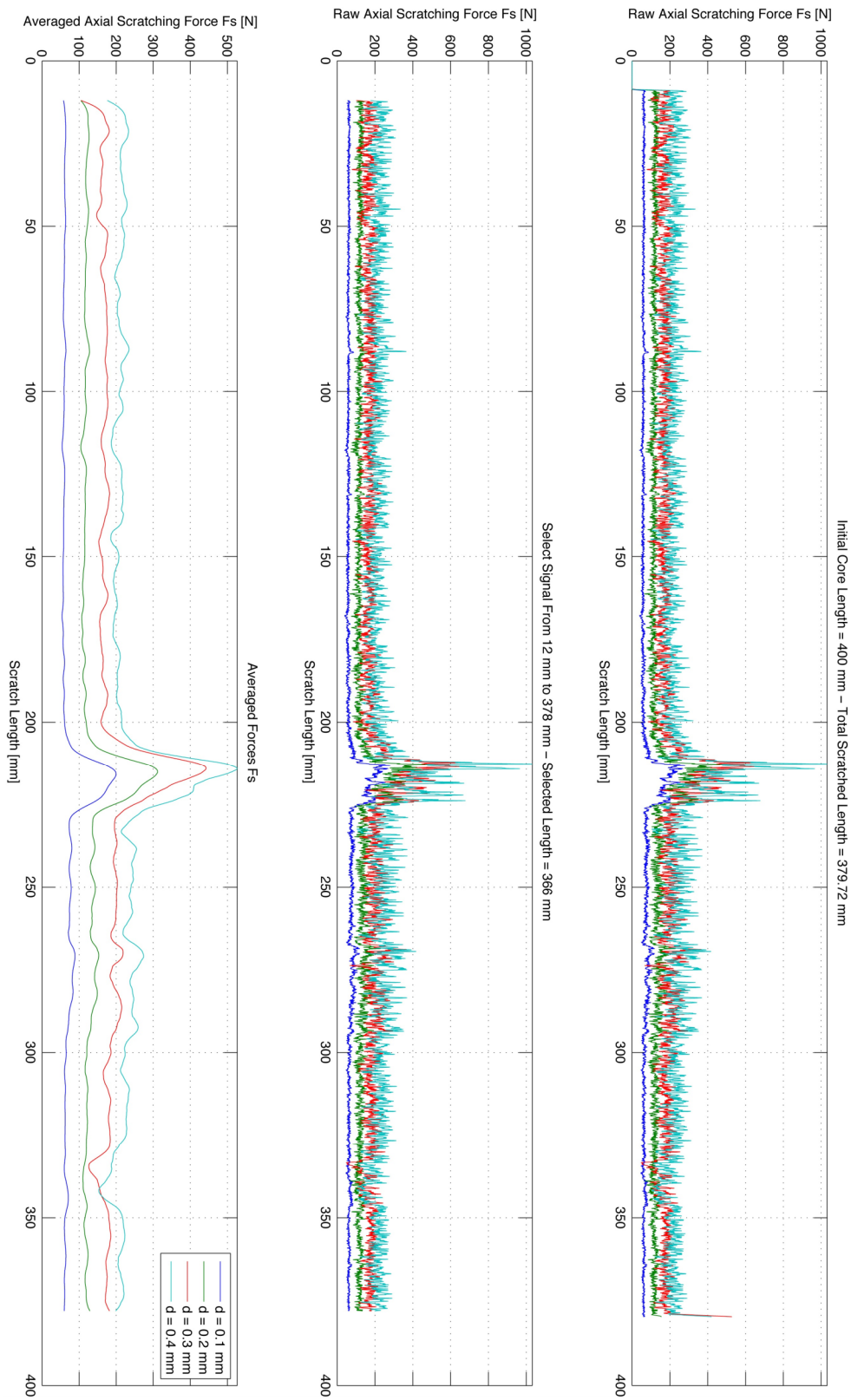


Fig. 3-7: SCR02. Scratch test results: Four depths of cut have been used. The core has been scratched from the bottom to the top (right: original data; middle: cut-off of edge effects; left: moving average).

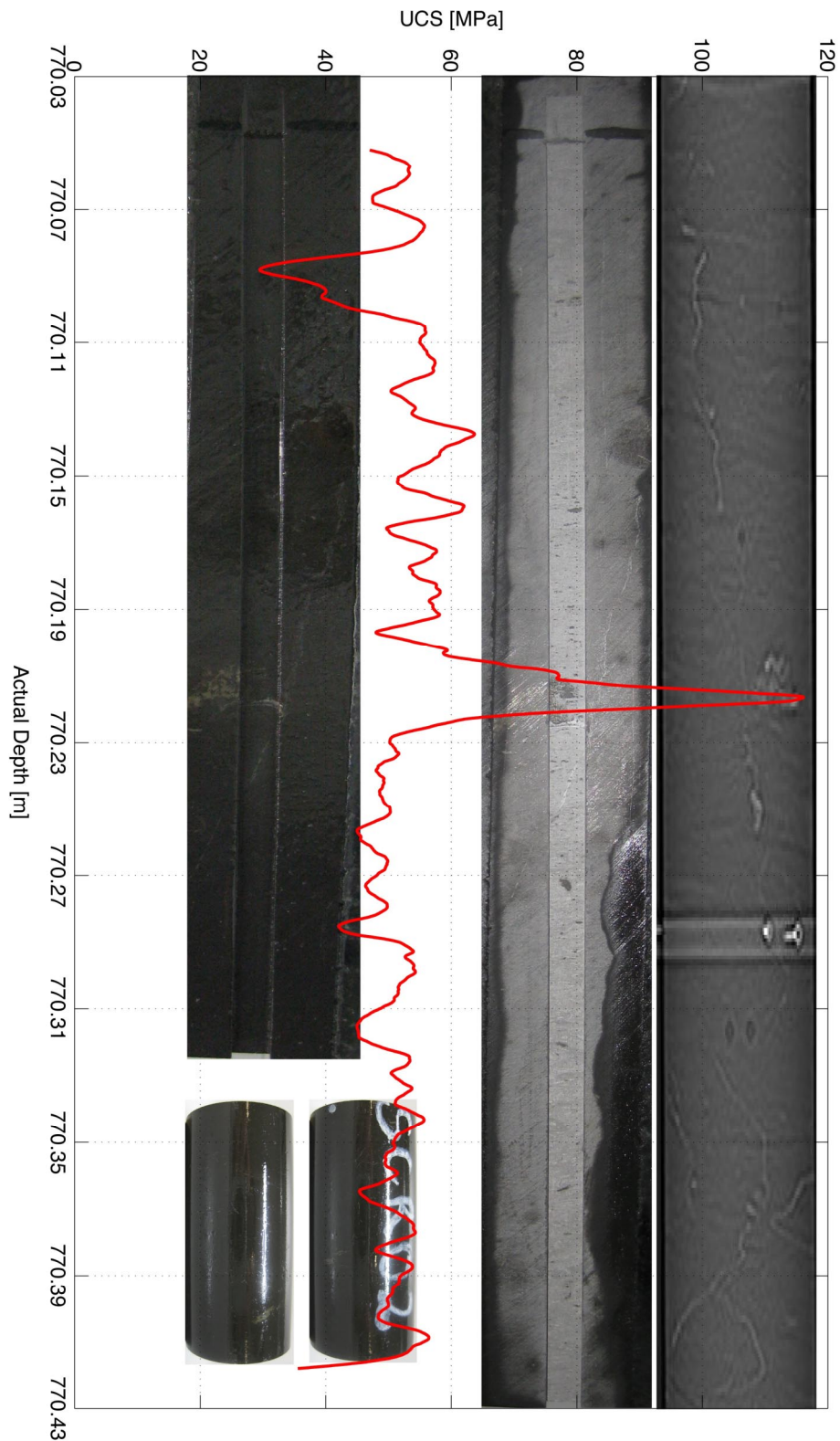


Fig. 3-8: SCR02. Unconfined compressive strength log (UCS log). The high UCS value at 770.12 m may be explained by the carbonate spot at this location as seen in the CT scan. The data for this test can be found in a digital form in the file Scratch-SCR02.xls.

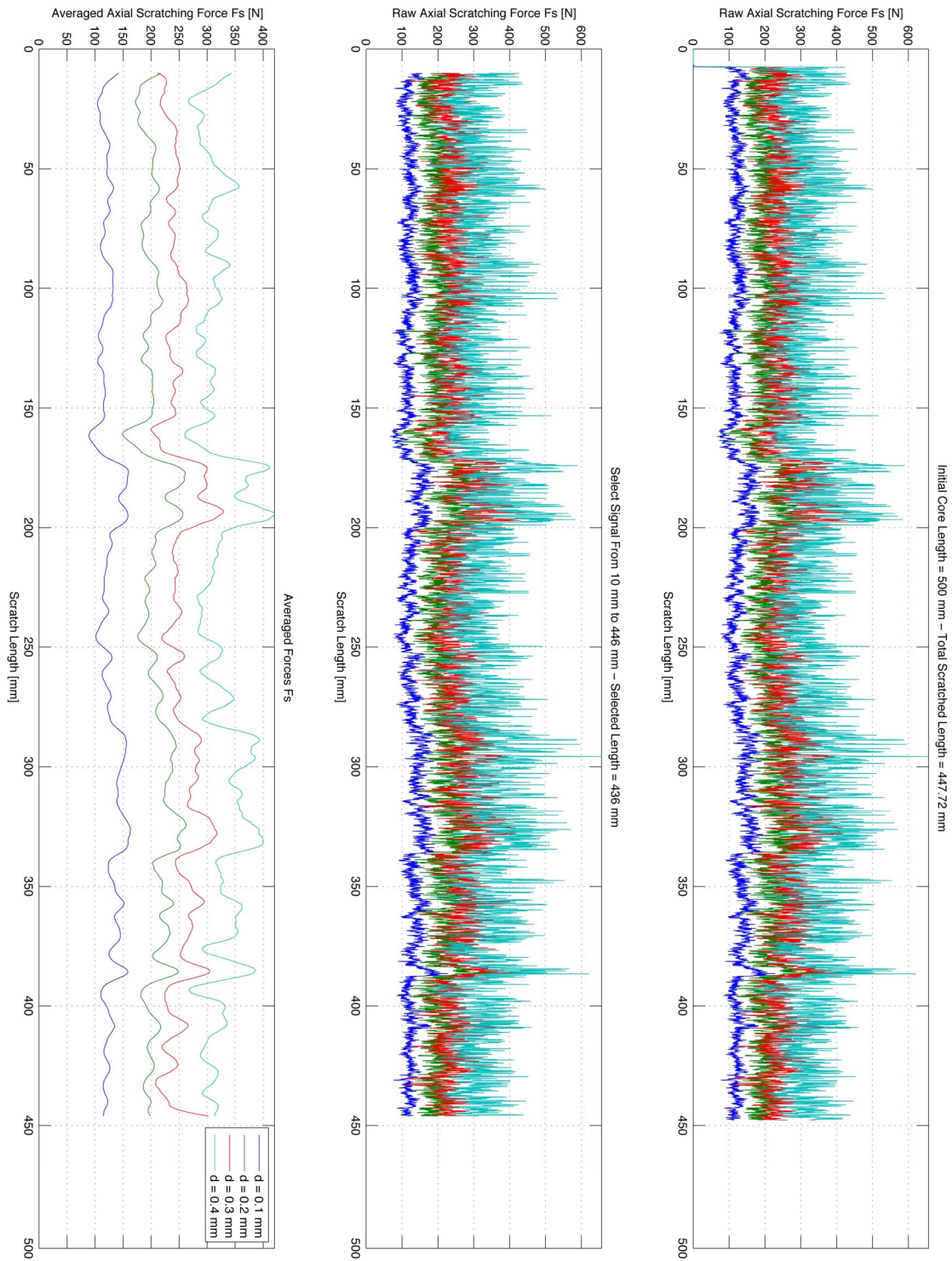


Fig 3-9: SCR03. Scratch test results: Four depths of cut have been used. The core have been scratched from the bottom to the top (right: original data; middle: cut-off of edge effects; left: moving average).

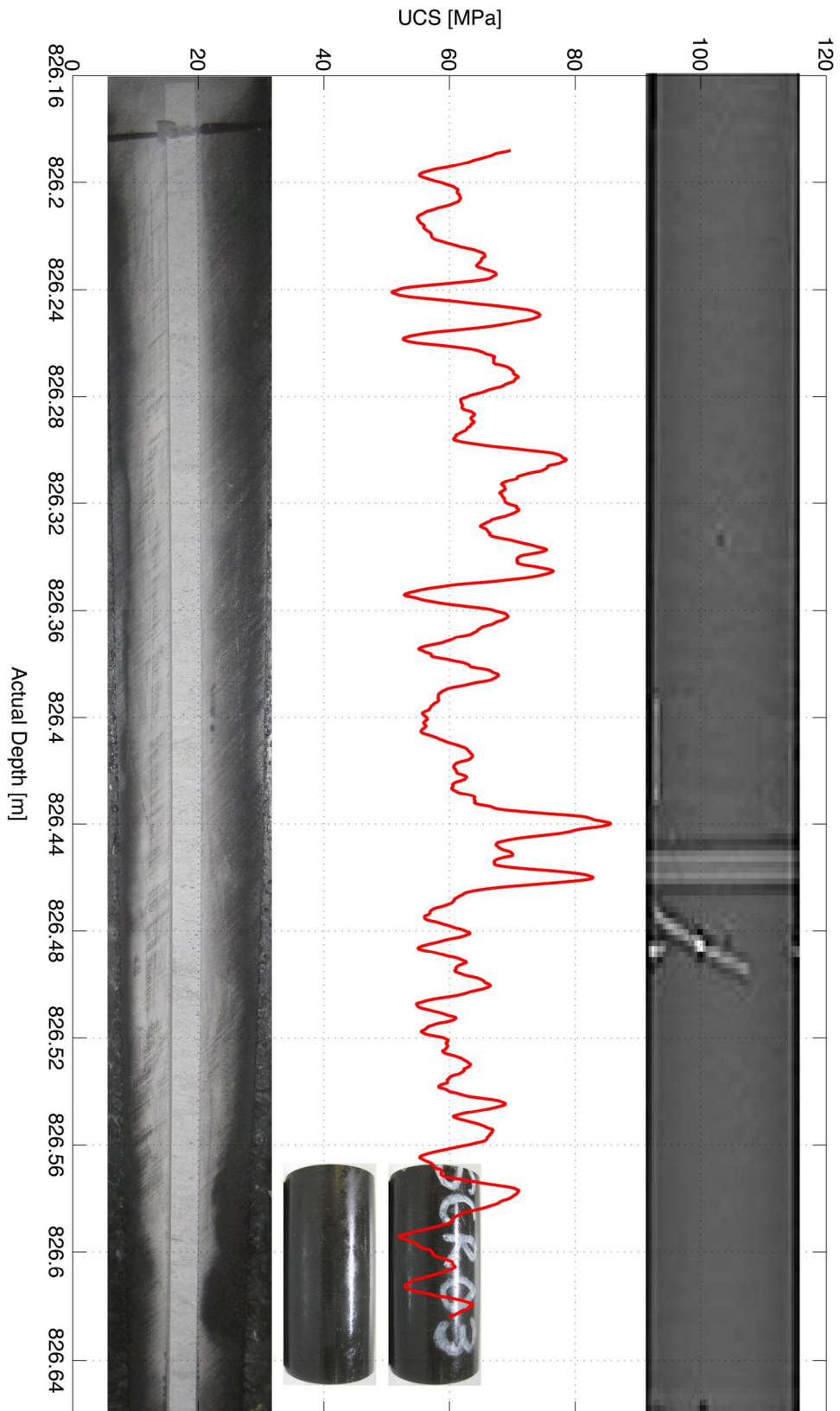


Fig. 3-10: SCR03. Unconfined compressive strength log (UCS log). The data for this test can be found in a digital format in the file Scratch-SCR03.xls.

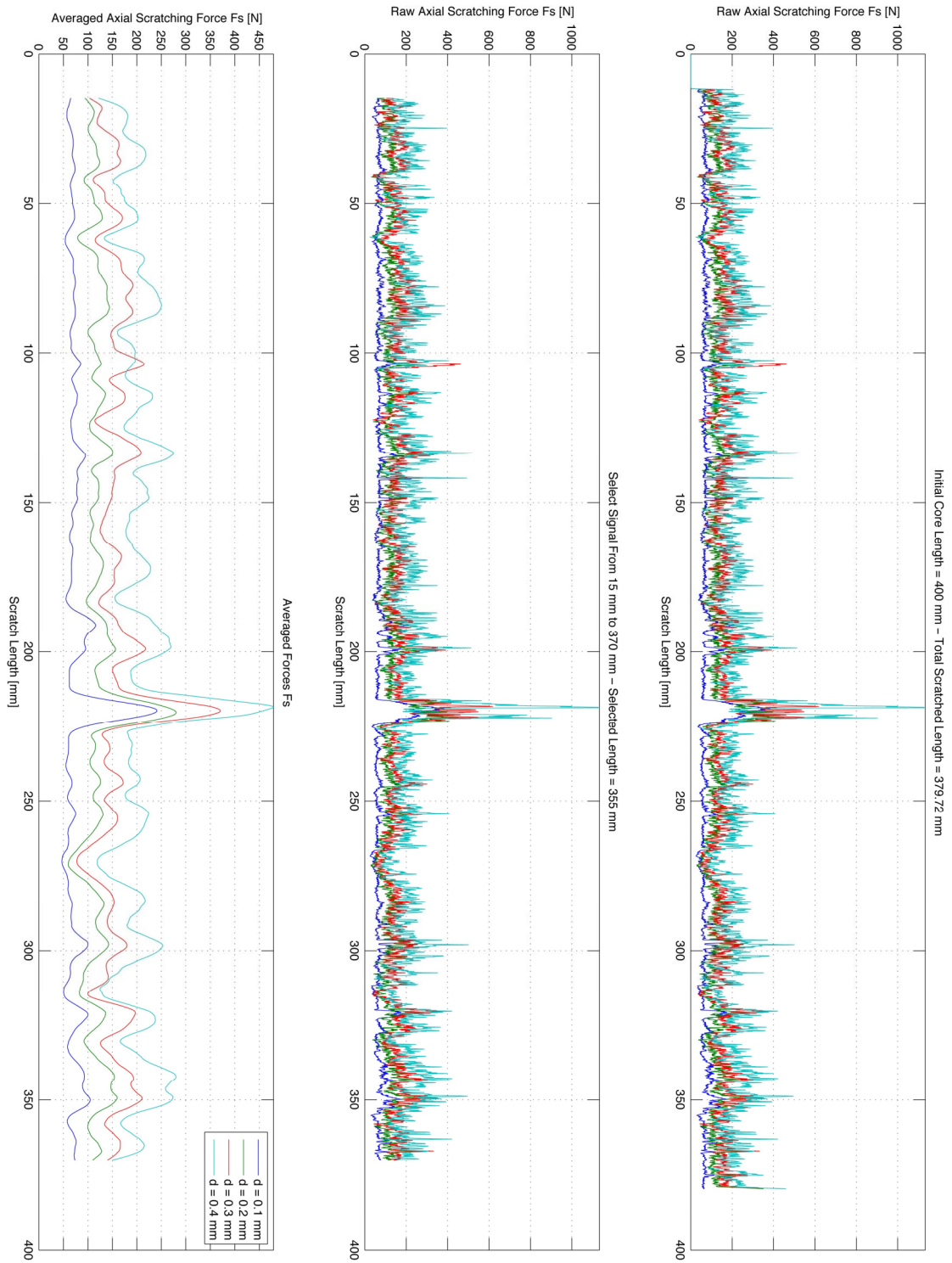


Fig. 3-11: SCR04. Scratch test results: Four depths of cut have been used. The core has been scratched from bottom to top bottom (right: original data; middle: cut-off of edge effects; left: moving average).

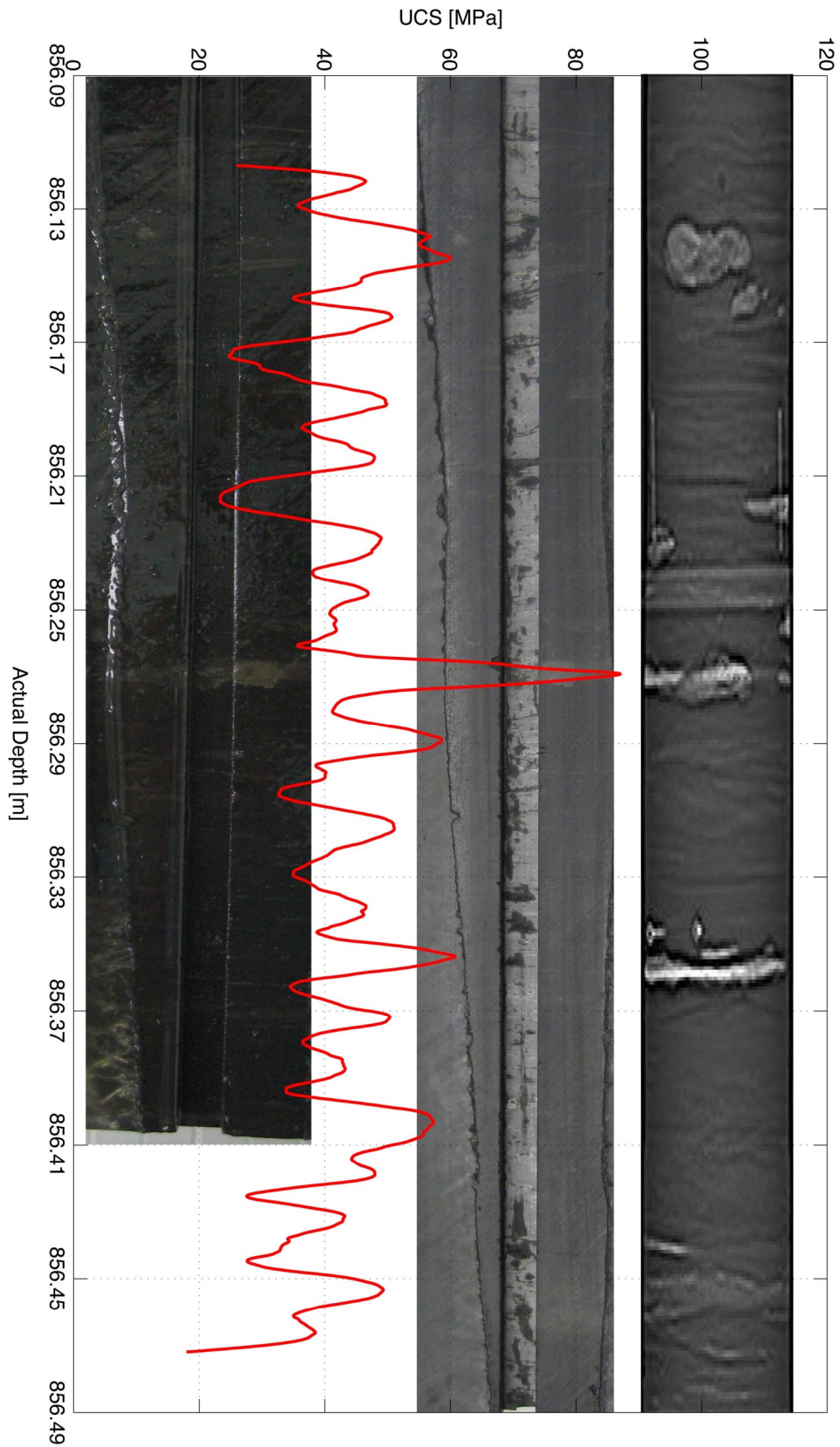


Fig. 3-12: SCR04. Unconfined compressive strength log (UCS log). The data for this test can be found in a digital format in the file Scratch-SCR04.xls.

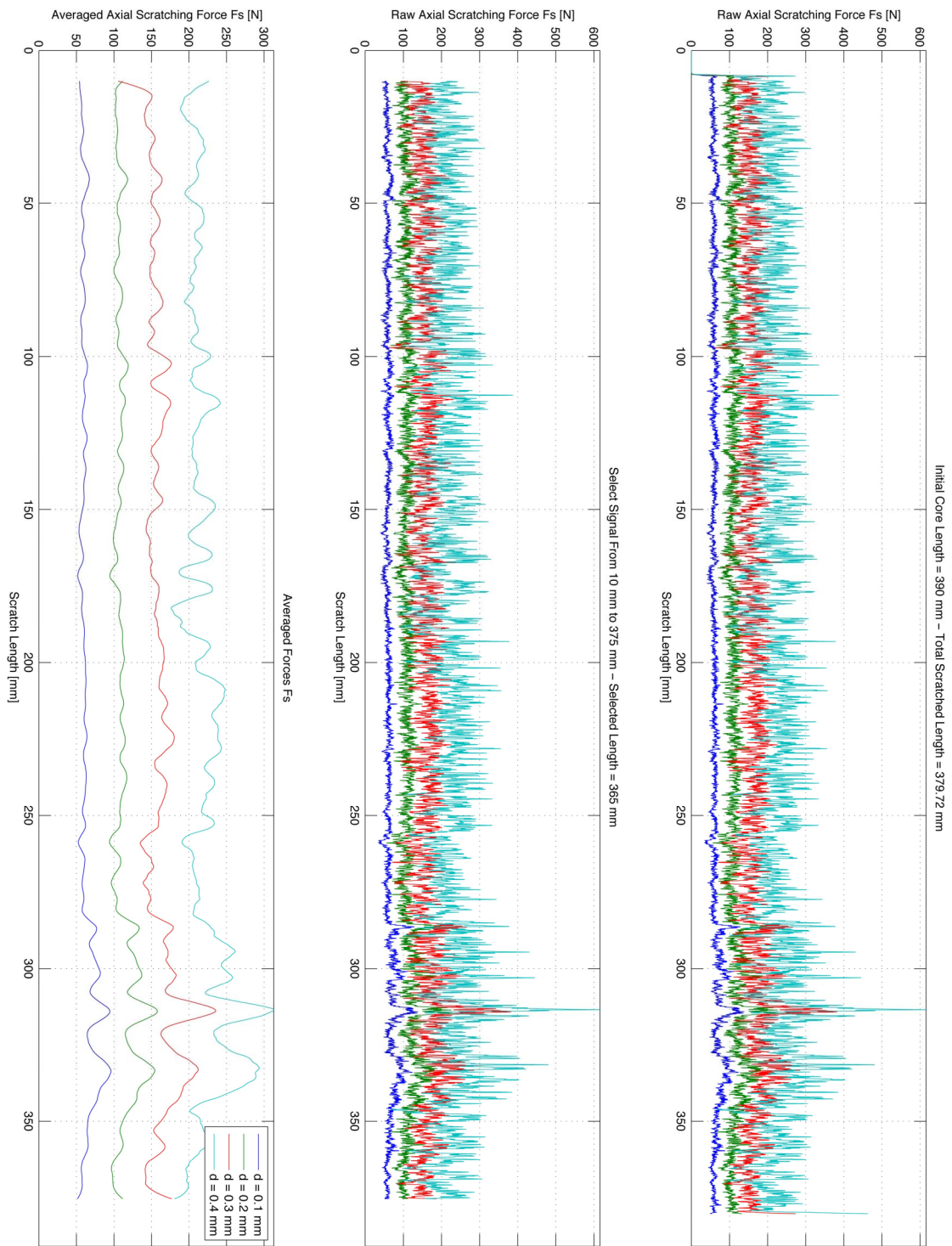


Fig. 3-13: SCR05. Scratch test results: Four depths of cut have been used. The core has been scratched from bottom to top.

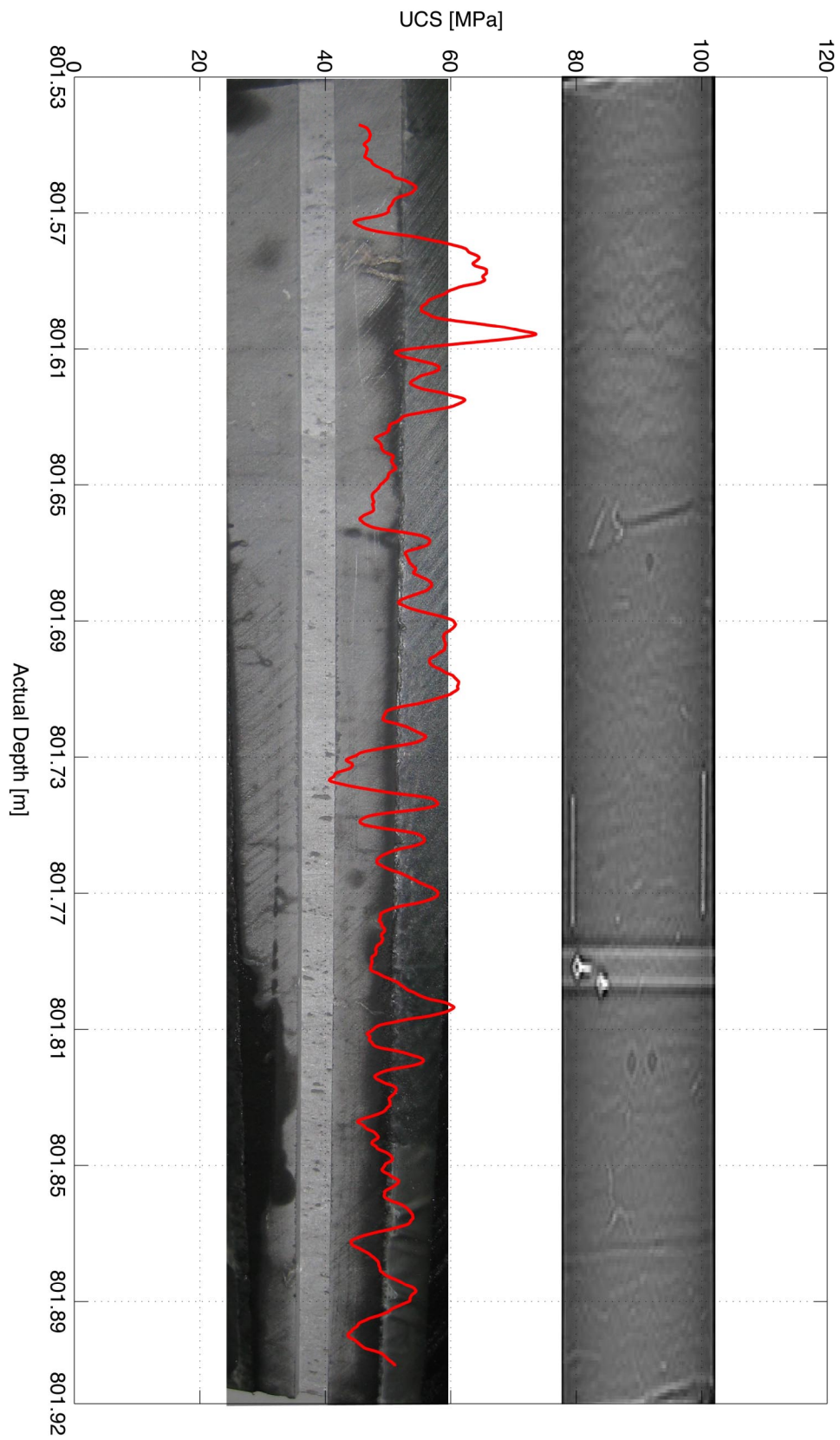


Fig. 3-14: SCR05. Unconfined compressive strength log (UCS log). The data for this test can be found in a digital format in the file Scratch-SCR05.xls.

### 3.3 Uniaxial Loading of Cylindrical Plugs

#### 3.3.1 Experimental Methodology

Plugs with dimension  $D = 38\text{mm}$  and  $L = 76\text{mm}$  have been sub-cored from the lower (deeper) part of each of the cores named SCR01, SCR02 and SCR03. UCS tests are conducted using a stiff computer-controlled uniaxial loading frame. The cylindrical rock sample is axially loaded at a constant displacement rate of  $0.39\text{mm/hour}$  until failure occurs and sufficient residual strength is observed. The specimen is equipped with (see Fig. 3-15): (i) two diametrically-opposed LVDTs (Linear Variable Differential Transformers) mounted between the sample end platens to measure axial displacement of the sample and calculate the average axial strain; (ii) four cantilever (orthogonal) radial gauges mounted at the mid-height of the sample to measure radial deformation; and (iii) a load cell located beneath the base platen to measure axial load;

Young's modulus and Poisson's Ratio are calculated from the axial and radial strain measurements taken throughout the test. Axial peak stress is used to determine the UCS of the specimen.

In this context it is worth commenting on the accuracy of LVDT's compared to strain gauges. For example, Olsen et al. (2008) showed that there was good agreement between  $E_{dyn}$  and  $E_{stat}$  of chalk when the latter was measured using strain gauges. However,  $E_{dyn}$  was found to be 1.3–5 times higher than the  $E_{stat}$  value obtained using LVDT's.

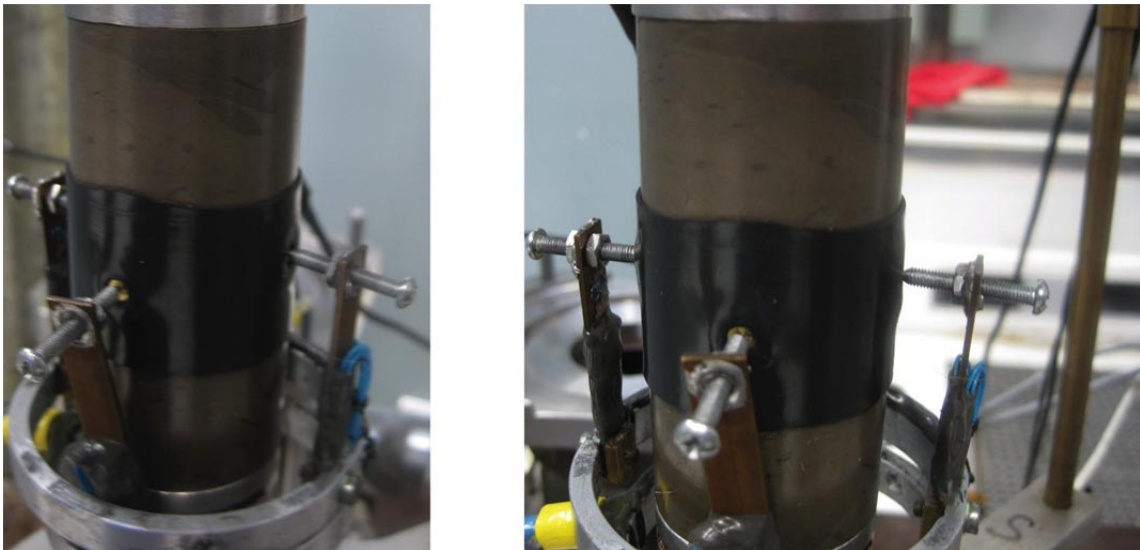


Fig. 3-15: Uniaxial stress loading of a cylindrical rock specimen for direct determination of the UCS. Specimen assembly including: (i) two orthogonal pairs of cantilevers for radial strain measurements; and (ii) a pair of diametrically-opposed axial LVDTs for axial strain measurements.

### 3.3.2 Results

A summary of the results of these tests is reported in Table 3-2 for each core SCR01 to SCR03, respectively. The details of the data can be found in a digital format in the files UCS-SCR01.xls, UCS-SCR02.xls and UCS-SCR03.xls. For the three tests, Fig. 3-16 displays the pictures of the specimen before and after testing.

For the plug extracted from SCR01, UCS = 170.8MPa, whereas the scratch test gives, in this area (bottom end of the core) UCS ~ 60MPa in average. For the plug extracted from SCR02, UCS = 36.5MPa, when the scratch test gives, in this area (bottom end of the core) UCS ~ 50MPa in average. For the plug extracted from SCR03, UCS = 66.3MPa, when the scratch test gives, in this area (bottom end of the core) UCS = 60MPa in average. Note that while the scratch test allows for the estimation of the UCS all along the core (similar to a borehole logging tool), uniaxial testing allows for the estimation of the UCS on a single plug extracted from this core. On the other hand, the scratch test only probes one “side” of the core, whereas the plug can be extracted from any location within that depth in the diameter of the core (see Fig. 3-17). Another source of uncertainty is the state of saturation of the test sample prior to testing. It is recommended to include suction measurements before/after testing as part of future test protocols for both scratch tests and UCS tests.

If the rock is ideally homogeneous, both test types should give the same results as experimentally demonstrated on more homogeneous rocks (see Fig. 3-3). Rock heterogeneity, as evidenced by the X-ray imaging in Fig. 2-1 and in attached image files for these cores is most probably responsible for the differences in estimation of the UCS by these two testing methods.

Tab. 3-2: Summary of the results of the uniaxial loading test on the specimen extracted from the deepest end of the cores SCR01, SCR02 and SCR03. Full dataset can be found in a digital format in the file UCS-SCR01.xls, UCS-SCR02 and UCS-SCR03.

	SCR01	SCR02	SCR03
Pretest dry density (g/cm <sup>3</sup> )	2.63	2.50	2.53
Effective confining stress (MPa)	0.0	0.0	0.0
Peak differential stress (MPa)	170.8	36.5	66.3
Young's Modulus (GPa)	21,8	4.6	12.6
Poisson's Ratio (-)	0.14	0.13	0.14



Fig. 3-16: Rock specimens extracted from cores SCR01 (a), SCR02 (b) and SCR03 (c) pre-testing and post-failure. Stress-strain data for these three tests can be found in digital format in the files UCS-SCR01.xls, UCS-SCR02.xls and UCS-SCR03.xls, respectively. Summary of the main results of these 3 tests are reported in Tab. 3-2.

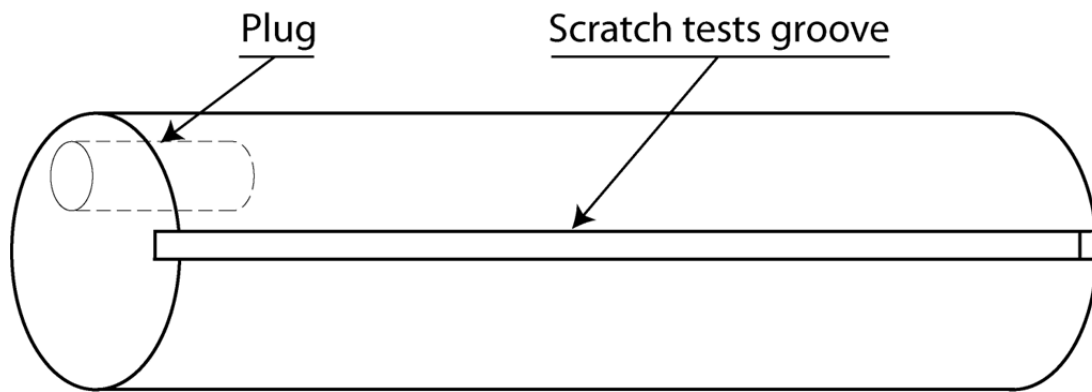


Fig. 3-17: Schematic explanation of the possible difference in the estimation of the UCS by the scratch test and the uniaxial loading methods for a heterogeneous rock core.

## 4 Petrophysics/rock physics characterization

We present in this section the results of water content from NMR, electrical properties such as resistivity, formation factor from low frequency and conductivity-dielectric from high frequency, pore water salinity extraction, ultrasonic velocity. All the main results are summarized in the conclusion part.

### 4.1 Nuclear Magnetic Resonance

Proton Nuclear Magnetic Resonance (NMR) measurements have been made on a preserved plugs collection to investigate water content, its relation with pore size and surface adsorption, microenvironment and mobility using a Maran-Ultra spectrometer at 2 MHz (Oxford Instruments Ltd.). NMR corresponds to a measurement of the response of atomic nuclei spin (i.e. spin precession) within an applied magnetic field. Only nuclei with an odd number of protons or neutrons can be measured such as hydrogen ( $^1\text{H}$ ), Carbon ( $^{13}\text{C}$ ) and sodium ( $^{23}\text{Na}$ ). The other types of nuclei responses are too small to be detected. Because hydrogen has only a single proton, no neutron (i.e. spin  $\frac{1}{2}$ ) and is very abundant in water and hydrocarbons, its NMR response gives a strong signal at accessible resonance frequencies. These properties of the proton make hydrogen the major element studied in petrophysics and in the petroleum business. Theory can be found in Dunn et al. (2002).

#### 4.1.1 Spin Polarization and Longitudinal Relaxation Time $T_1$

In natural conditions, all the hydrogen nuclei spins are randomly oriented in materials and fluids, until an external static magnetic field ( $B_0$ ) is applied which orients a fraction them in the same direction and generates a weak but important net magnetization along the magnetic field direction, which we conventionally denote the z axis. We call this phenomenon “polarization” along their longitudinal spin direction. This polarization does not occur immediately but rather grows with a time constant called the longitudinal relaxation time,  $T_1$ . ( $B_0$ ).  $T_1$  is defined as the magnetization reaches 63% of its final value, and  $3 \times T_1$  will reach 95% polarization (Fig. 4.1).

The magnetization  $M$  grows as:

$$M = M_o \cdot (1 - e^{-t/T})$$

$T_1$  is sometimes called the spin-matrix relaxation time: the matrix means the prevailing magnetic field in the “environment” or physicochemical surroundings of the particular atom in the particular molecule containing the particular hydrogen nucleus. Protons in different species and phases (and even different positions in the same molecule) have different  $T_1$  values: free water (long polarization time, on the order of seconds), oil (moderate) and gas (very long), or clay bound water (very short on the order of ms).

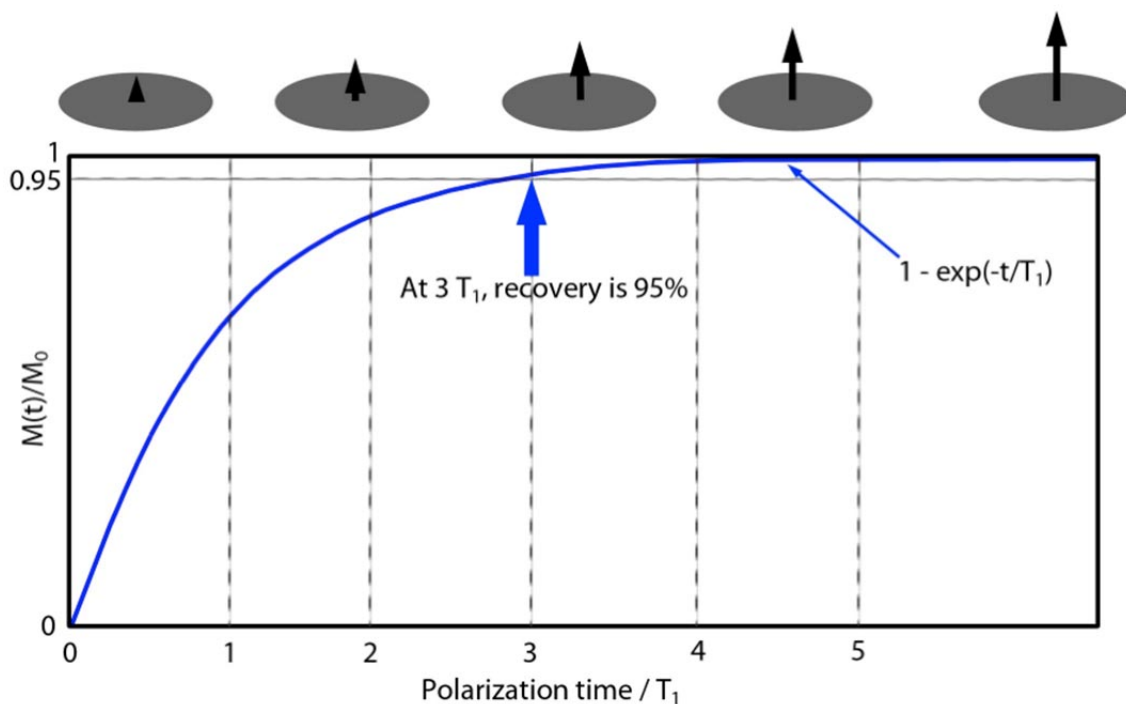


Fig. 4-1: Induced curve during Polarization  $T_1$ -relaxation (degree of alignment) as function of the time that hydrogen population is exposed to an external constant magnetic field.

#### 4.1.2 Spin Tipping onto the Measurement Plane and Free Induction Decay (FID)

If during polarization an external oscillating magnetic field ( $B_1$ ) having the Larmor frequency of the studied species (hydrogen by instance) is applied perpendicular to the polarizing static magnetic field ( $B_0$ ), it will tip the magnetization (i.e. direction perpendicular to the precessing plan) from the longitudinal direction towards a transversal plane. The tip angle is function of time or strength of  $B_1$  and becomes in phase with other protons precessing in the same plane. When the power and time of the  $B_1$  energy pulse is just sufficient to tip the magnetization into the transverse x-y plane, we call it a  $90^\circ$  pulse. The phasing generates a nuclear magnetic resonance *sensu-stricto* and increases the net magnetization in a direction that rotates like a lighthouse beam around the  $B_0$  or z axis. The x-y plane is the “measurement” plane in all NMR experiments; we don’t detect the magnetic field itself but rather the EM field radiated into space by the precessing spins induces a small but detectable electrical current in a conducting detector coil around the sample. So the detected NMR signal is zero until the spins are tipped over, and from that point, the evolution in time and further manipulation of the tipped spins constitute the NMR experiment. The spin manipulation is by means of EM pulses.

When the applied magnetic field  $B_1$  is removed, the resonating spins diphas (the beam spreads out AND spirals back towards the  $B_0$  or z direction) and the net magnetization in the x-y plane decreases with an exponential decay called Free Induction Decay (FID) with a very short relaxation time  $T_2^*$ . FID involving a polarization stage, a tip to 90 degrees with an RF pulse, and spiraling decay from the measurement plane, is the simplest possible NMR experiment.

### 4.1.3 Spin Refocusing, CPMG Pulse Sequence and Transverse Relaxation Time $T_2$ .

The de-phasing in the transverse plane can be re-focused when an external  $180^\circ$   $B_1$  field pulse is applied that will change the magnetization vector by  $180^\circ$  (Fig. 4.2). This transversal re-phasing generates a new magnetization pulse called a “spin-echo” at a certain time  $\tau$  after the pulse is applied. This  $180^\circ$  pulse can be applied repeatedly to re-phase the magnetization and generates a series of spin echoes separated by  $2\tau$  (= the Echo Spacing). The entire pulse sequence composed of a  $90^\circ$  pulse followed by a long series of  $180^\circ$  pulses is called a CPMG sequence invented by Carr, Purcell, Meiboom and Gill. The CPMG sequence preserves the signal amplitude from dephasing so that the true transverse relaxation time  $T_2$  ( $>T_2^*$  but  $< T_1$ ) related to spin-spin interactions can be measured so long as the magnetic field within the sample is sufficiently homogeneous.

The result is a decay curve with relatively good signal to noise, whose relaxation rate depends on a number of parameters:

$$\text{decayrate} = \frac{1}{T_2} + (\gamma \cdot \nabla H)^2 \cdot D \cdot \frac{\tau}{3}$$

$T_2$  is the intrinsic transverse relaxation time of the spin signal projected onto the x-y measurement plane. Thus if nothing else were to happen, the spin vector would spiral back up to the  $B_0$  direction, all the while decaying at the intrinsic decay rate dictated by  $T_1$  of the fluid.

$H$  is the magnetic field strength. So where the magnetic field is completely homogeneous in space, the additional decay rate owing to spin movements is zero. That is to say, the spins can move between the application of the tipping pulse and measurement pulse, but they will not de-phase because the magnetic field they experience is identical.

$\gamma$  is the gyromagnetic ratio for the nuclear species (for protons, the gyromagnetic ratio  $\gamma$  is 42.58 MHz per tesla).

$\tau$  is the time for the 90-180 degree pulse interval, equal to half the echo spacing of the CPMG sequence. The longer the spacing, the worse is the effect of magnetic gradients on transverse spin decay.

$D$  is the molecular diffusivity of the species wherein the proton resides. For bulk water this has a value of around  $2 \times 10^{-9} \text{ m}^2 \text{ s}^{-1}$ . Protons residing in gas and oil experience much higher and much lower diffusivities, respectively. Inside a shale,  $D$  varies according to the position of the water: in interlayer positions and within the ambit of charged mineral surfaces diffusivity may be orders of magnitude lower than in bulk water. The linear dependence of spin decay rate on  $D$  means that we can use controlled gradient experiments to study the complicated diffusivity of water within shales as we will explain later.

Aside from dephasing, spins can also be annihilated (euphemistically “relax”) by interaction with other spins, ions or surface sites-anything magnetic in fact. In cases of geological interest the main extra source of spin decay is relaxation at surfaces. Practically, this dominates  $T_2$  (and also  $T_1$ ) in most porous rocks, such that.

$$\frac{1}{T_2} \approx \rho \cdot \frac{S}{V}$$

Where  $\rho$  is the surface relaxation strength, and  $S/V$  the surface area to volume ratio of the pore space. It is easy to see that if the surface relaxation is constant, then relaxation in small pores will be much faster than in large pores, underpinning the application of NMR to estimation of pore size distribution. In shales, essentially all the NMR signal decays in a very short time due to this surface relaxation accentuated by local field gradients caused by contrasts between magnetic properties in the rocks and fluid.

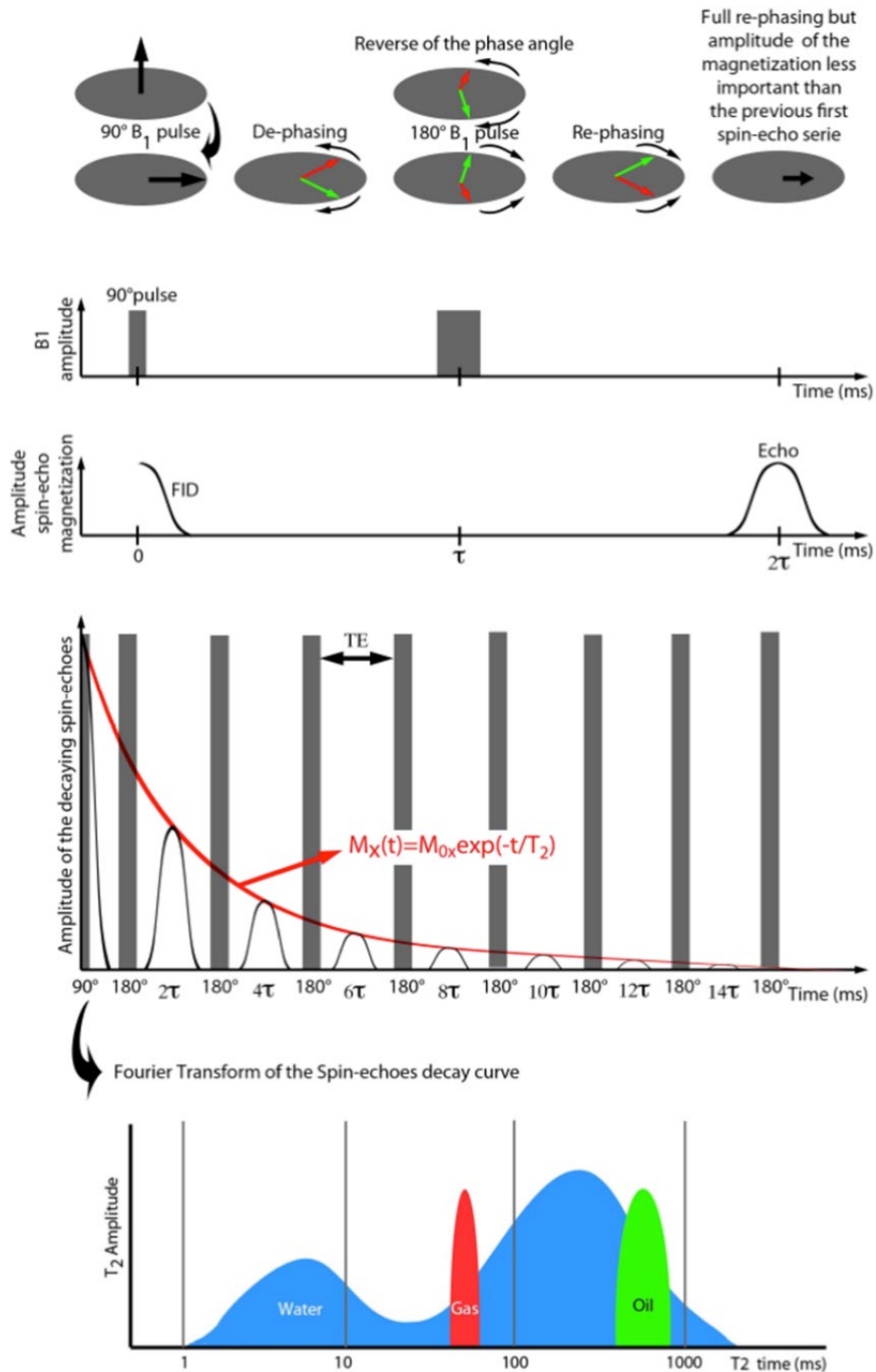


Fig. 4-2: Explanation of the CPMG pulse sequence to measure  $T_2$ .

#### 4.1.4 Plug preparation and methodology

The previous preserved plugs were subjected to NMR testing in order to record their water content before any further tests. The plugs were 1.5 inch in diameter and  $\pm 55$  mm in length. First, preservation oil was wiped out from the samples surface. The samples were then wrapped in transparent cling wrap and inserted in sealed plastic jars in order to prevent any water exchange with the room atmosphere during the testing. Eventually, the samples were slowly equilibrated at 35C (temperature inside the NMR apparatus) prior to any NMR measurement.

After initial calibration of the NMR apparatus (background noise recording and signal artefacts removal), a sample material with known NMR is first measured (pure water doped with NiCl). Three NMR sequences were chosen and applied to that particular sample of doped water: FID and CPMG using 256 scans, time delay of 2 seconds and receiver gain of 70%; and finally an Inverse Recovery (INVREC) using 8 scans, time delays from 150  $\mu$ s to 200 ms logarithmically spaced with 99 points, and 70% of receiver gain. The water calibration data are used to scale the actual rock sample tested under similar conditions, although for the actual rock samples a larger number of scans is used to improve the inherently low signal-to-noise ratio associated with the small amount of water present in clayrocks, i.e., FID with 1024 scans, CPMG with 4000 scans and INVREC with 64 scans. The NMR results scaled to doped water response, scan number and sample volume-mass allow for the computation the bulk water content and consequently the samples porosity (assuming a full saturation of the preserved samples). As a by-product of the NMR testing, water distribution along the pore size is also computed.

The timing for a full data acquisition on a given sample is:

- FID: 35 minutes
- CPMG: 2 hours and 15 minutes
- INVREC:  $\pm 4$  hours

The three consecutive NMR sequences require a full day/sample.

The plug mass is tracked before and after NMR acquisitions to record any water lost during the day of NMR data acquisition. Usually, the samples mass changes by less than 0.1%, which corresponds to less than 1% of the total porosity. The NMR amplitude is plotted along the time constant  $T_2$  from each NMR sequence, which represents water distribution as a function of pore sizes (not throats) in the rock's pore space, i.e. smaller  $T_2$  corresponds to smaller pore sizes). The total amount of water in mass and volume percentage for samples tested is summarized in Table 4.1.

As a complementary test, the sample measured by the evaporation method (see the following section 4.2) were NMR tested after drying in for 2 days at 65C, which induced about 90 to 99 % water lost (see Fig 4.12 for evaporation water details). In this context, it should be noted that the  $d$  at 65C has been compared with the higher temperatures (105C), commonly used in thermogravimetric analysis (e.g., Handwerger 2011). We expect to record from these NMR tests, the clay bound water remaining despite the heating process, which should only affect the free and weakly bound-capillary water. Such approach should help to properly extract the cut-off between the clay bound water from the movable water. This methodology could be applied to NMR logs to extract these amounts of water in situ and help computing permeability using Coates et al. (1999) model.

#### 4.1.5 NMR results

Raw data and data processed through Laplace inversion are plotted (example in Fig. 4-3; See all the similar processed data for each plug in file: NMR/NMR\_analysis):  $T_1$ ,  $T_2^*$  and  $T_2$  are plotted against relaxation time to evaluate the amount of water in each plug and its distribution

different pore sizes (i.e. Clay Bound Water versus capillary/weakly bound water and free water). Most of the samples present a bimodal distribution of relaxation times with a dominant one around 1 ms representing the capillary water and a minor one  $> 10$  ms related to the free water. The INVREC method seems to be the most efficient method to detect water within small pores (CBW / weakly bound water) but with low resolution however. The CPMG gives a better water distribution but misses part of the CBW which induces an over-estimation of the water content at short time.

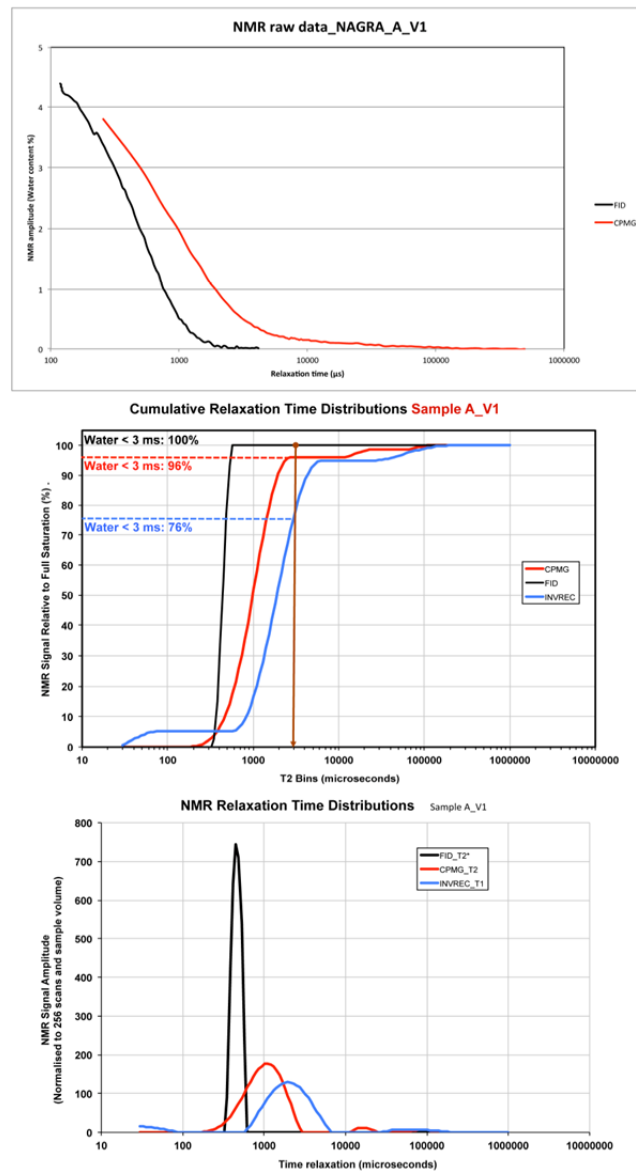


Fig. 4-3: Example of NMR distribution in NAGRA-A plug.

The top plot gives the raw signal NMR amplitude normalised to the volume of the plug to extract the water content at the first amplitude: maximum amplitude at the shortest time. The water content can be extrapolated to a time of  $0\mu\text{s}$ . The plot in the middle corresponds to the cumulative amplitude from the time distribution of the NMR signal (bottom plot) for each echo sequence method (FID/CPMG/INVREC). The "theoretical" water limit between CBW and capillary-free water is around 3 ms. Using this limit, it gives the amount of water in CBW for each plug. Note that INVREC sees in this example, two changes of slope: at short time (CBW) and long time ( $> 10$  ms: free water sensu-stricto).

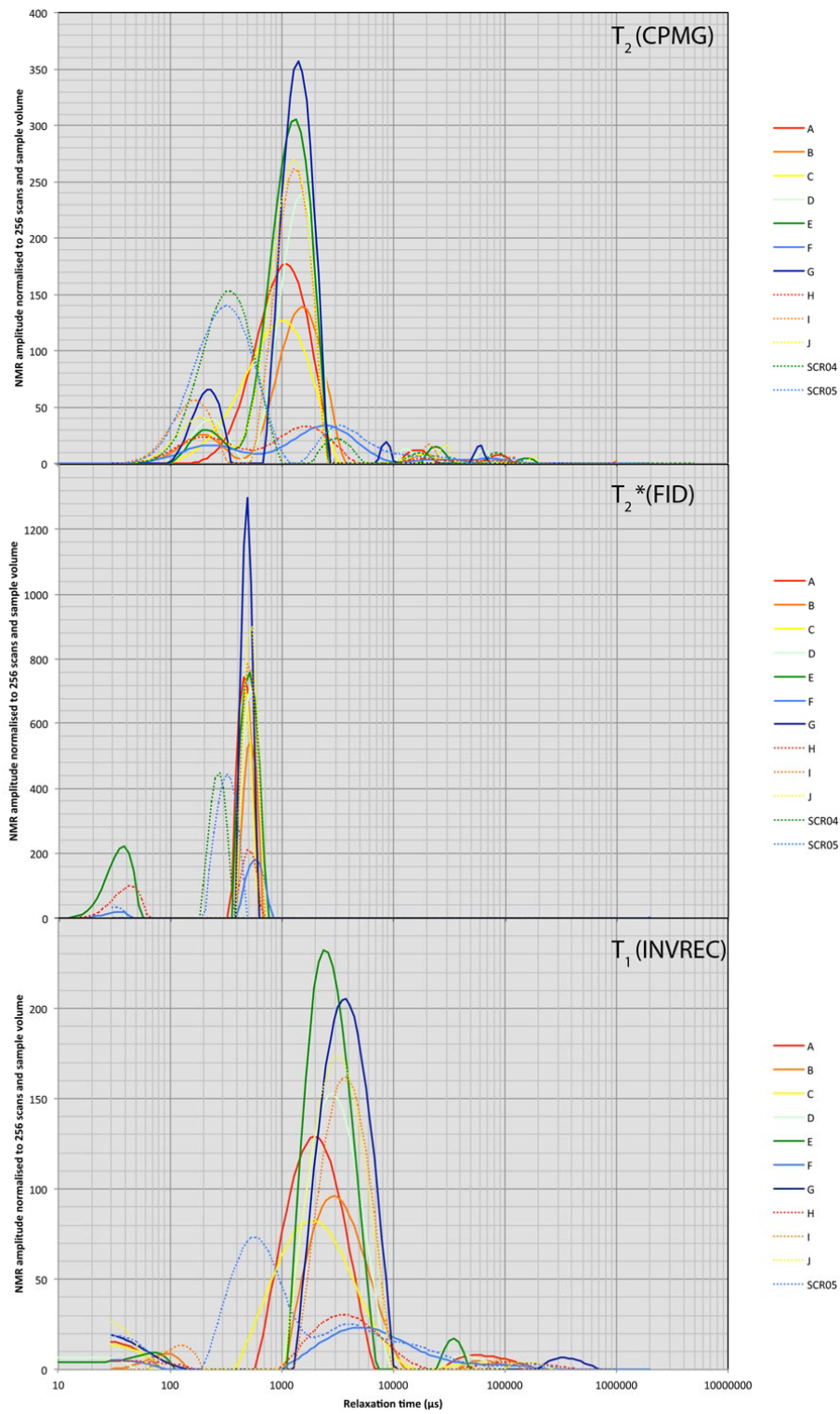


Fig. 4-4: NMR distribution from all the NAGRA collection with T2 distribution from CPMG (top), T2\* distribution from FID (middle) and T1 distribution from INVREC (Bottom).

All the NMR distributions from FID, CPMG and INVREC are plotted in the Fig. 4-4 to help visual comparisons and observe the appearance and time locations of water population. Note the large contrast in T2 distribution among SCR04/SCR05 and the other samples.

If we process the amount of data from each sample from the first NMR amplitude and from the integration of the full NMR time distribution for the 3 echo sequence editing: FID, CPMG and INVREC, we obtain a nice accuracy between the echo sequences for each samples but some tendency of overestimations from the integration method due to a lack of points of record at short time (i.e. CBW) at the Maran limits.

Tab. 4-1: Water content (%wt, mass normalized) from NMR using 1st amplitude and NMR time distribution with the 3 echo sequences for each NAGRA samples.

Sample #	NMR method	Water content 1st Amplitude (g)	Water (%)	Water content from T distribution (g)	Water (%)	Average 1st Amplitude (water %)	Average T distribution (water %)	Total average water content (%)
A	A FID	7.26	4.38	9.48	5.72	4.24	5.08	<b>4.66</b>
	A CPMG	6.30	3.80	8.30	5.01			
	A INVREC	7.51	4.53	7.44	4.50			
B	B FID	5.23	3.21	6.58	4.04	3.11	3.68	<b>3.40</b>
	B CPMG	4.66	2.86	6.19	3.80			
	B INVREC	5.31	3.26	5.24	3.21			
C	C FID	6.22	3.75	8.00	4.82	3.59	4.37	<b>3.98</b>
	C CPMG	5.29	3.19	7.41	4.46			
	C INVREC	6.39	3.85	6.34	3.82			
D	D FID	6.48	3.90	8.17	4.93	3.80	4.48	<b>4.14</b>
	D CPMG	5.76	3.47	7.51	4.52			
	D INVREC	6.67	4.02	6.60	3.98			
E	E FID	8.38	5.08	14.60	8.86	4.98	6.68	<b>5.83</b>
	E CPMG	7.56	4.58	9.87	5.99			
	E INVREC	8.67	5.26	8.57	5.20			
F	F FID	2.02	1.16	2.73	1.57	1.14	1.38	<b>1.26</b>
	F CPMG	1.82	1.05	2.47	1.42			
	F INVREC	2.12	1.22	1.99	1.15			
G	G FID	8.49	5.77	10.88	7.40	5.61	6.71	<b>6.16</b>
	G CPMG	7.52	5.11	9.92	6.74			
	G INVREC	8.77	5.96	8.83	6.00			
H	H FID	2.12	1.20	4.61	2.62	1.16	1.83	<b>1.49</b>
	H CPMG	1.83	1.04	2.88	1.64			
	H INVREC	2.16	1.23	2.16	1.23			
I	I FID	6.44	4.47	8.15	5.65	4.35	5.31	<b>4.83</b>
	I CPMG	5.72	3.96	8.24	5.71			
	I INVREC	6.69	4.64	6.61	4.58			
J	J FID	6.06	4.89	7.55	6.09	4.73	5.67	<b>5.20</b>
	J CPMG	5.27	4.25	7.34	5.92			
	J INVREC	6.25	5.04	6.20	5.00			
SCR04	SCR04 FID	4.23	2.62	6.54	4.04	2.30	4.04	<b>3.17</b>
	SCR04 CPMG	3.20	1.98	6.52	4.04			
	SCR04 INVREC							
SCR05	SCR05 FID	5.57	3.45	8.35	5.17	3.22	4.62	<b>3.92</b>
	SCR05 CPMG	4.30	2.67	8.31	5.15			
	SCR05 INVREC	5.73	3.55	5.69	3.53			

Table 4.1 synthesizes the water content (%) to evaluate a variability which appears to be < 0.3% of porosity (i.e. 10-15% in relative porosity). This reasonable accuracy is compared between the type of echo sequence in Fig. 4.5 where the FID and CPMG from time distribution have a tendency to over-estimate the water content of about 20% of the bulk water content due to a lack of good recording at NMR short time (i.e. CBW).

We used the water content from Fig. 4-6 or the equivalent porosity when the water mass is scaled with the sample volume considering a water density of 1 g/cm<sup>3</sup> (Fig. 4-7) to compute resistivity and formation factor in the section below dedicated to electrical properties (Section 4.3).

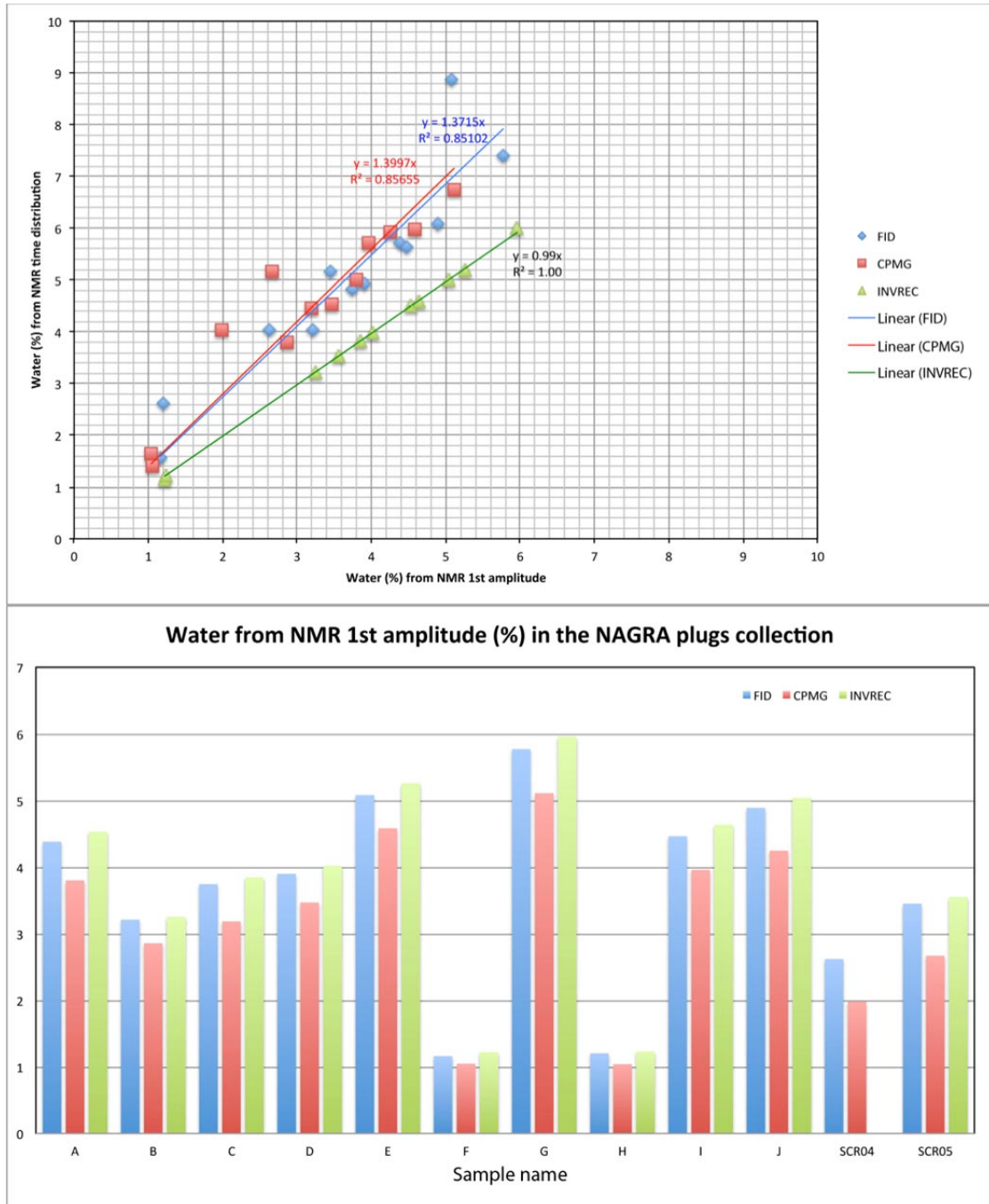


Fig. 4-5: Water content (%) from NMR with comparisons between the 3 echo sequences (FID/CPMG/INVREC) at the top, and presented under an histogram (bottom plot) to discriminate the specific plug sample with low or high water content.

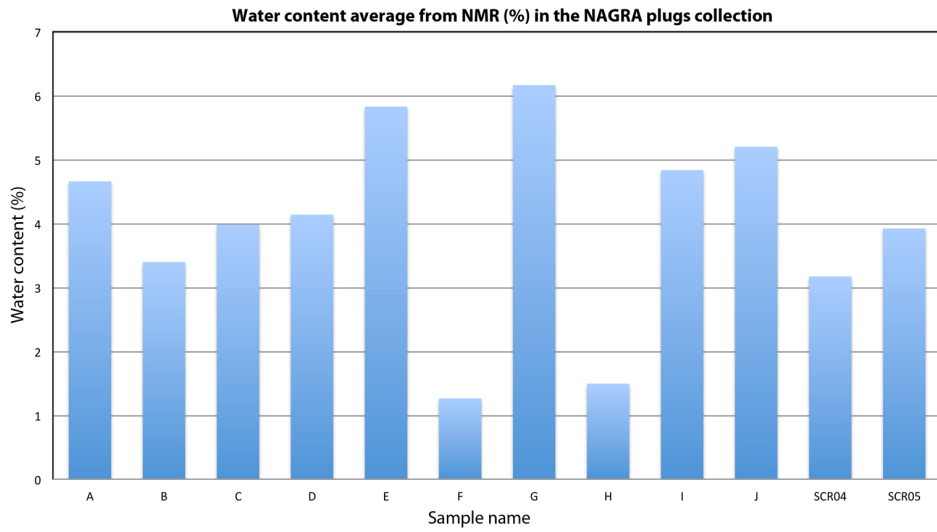


Fig. 4-6: Histogram of NMR water content (%) per sample averaged through the 1st amplitude and time distribution from each NMR methods. Note the very low content in plugs NAGRA-F and -H and the highest for NAGRA-E and -G.

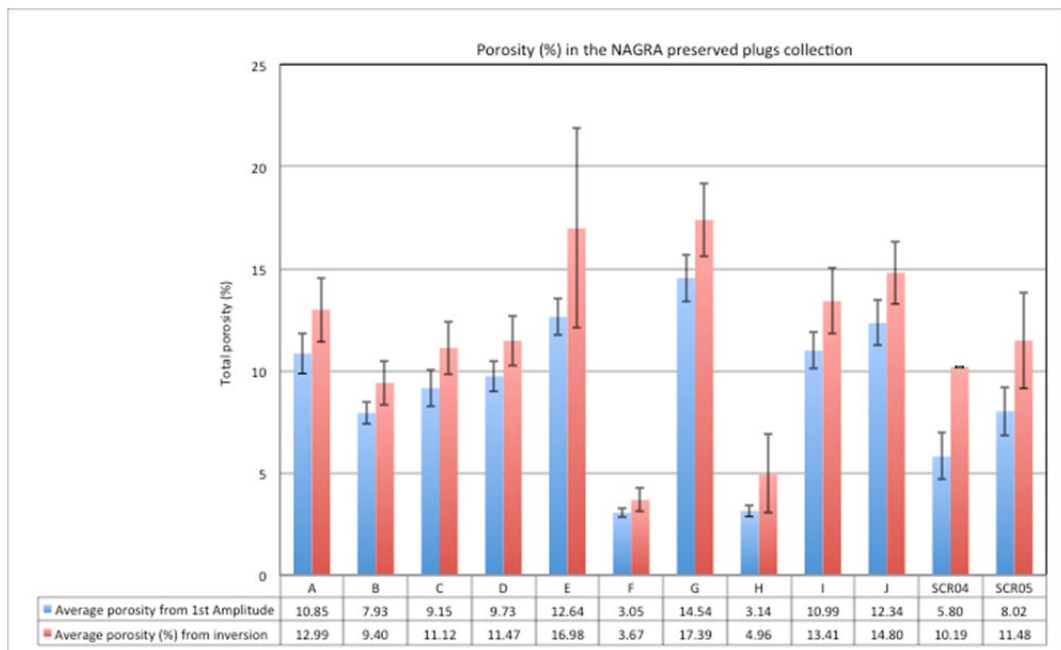


Fig. 4-7: Histogram of NMR total porosity (%) per sample computed from the previous water content normalized to the plug volume and averaged through the 1st amplitude (blue color) or through the inversion (red color) from each NMR methods (FID, CPMG and INVREC). Note the very low content in plugs NAGRA-F and -H and the highest for NAGRA-E and -G. The error-bars correspond to the standard deviation between the NMR methods applied on each plug sample.

We then tried to evaluate the Clay Bound Water (CBW) comparing the NMR results on preserved plugs against the NMR results on "thick" 1.5 inch diameter discs [with length between 9 and 30 mm, and used later on for evaporation tests, see the following section 4.2] after drying them for 2 days and rehydrating them at room conditions (RH ~ 35%) for 3 months. For the discs, we used the same NMR settings as for the preserved plugs but only applied the CPMG echo-sequence protocol because we are only tracking the water distribution versus pore size. The porosity distribution (Fig. 4-8) was re-calculated from the T2 distribution, scaling the NMR signal amplitude with the total porosity (%) obtained from the 1st amplitude signal. As expected, all the weakly bound water recorded under preserved condition around 1 ms disappeared after heating. Only the water strongly bound to the small pores (corresponding to T2 ~ 0.2 ms) remains or is recaptured from the room's atmosphere during the 3 months of rehydration. The relative humidity (RH) in the laboratory oscillated between 30% and 45% (mean around 35%), and the temperature was around 24-25 °C.

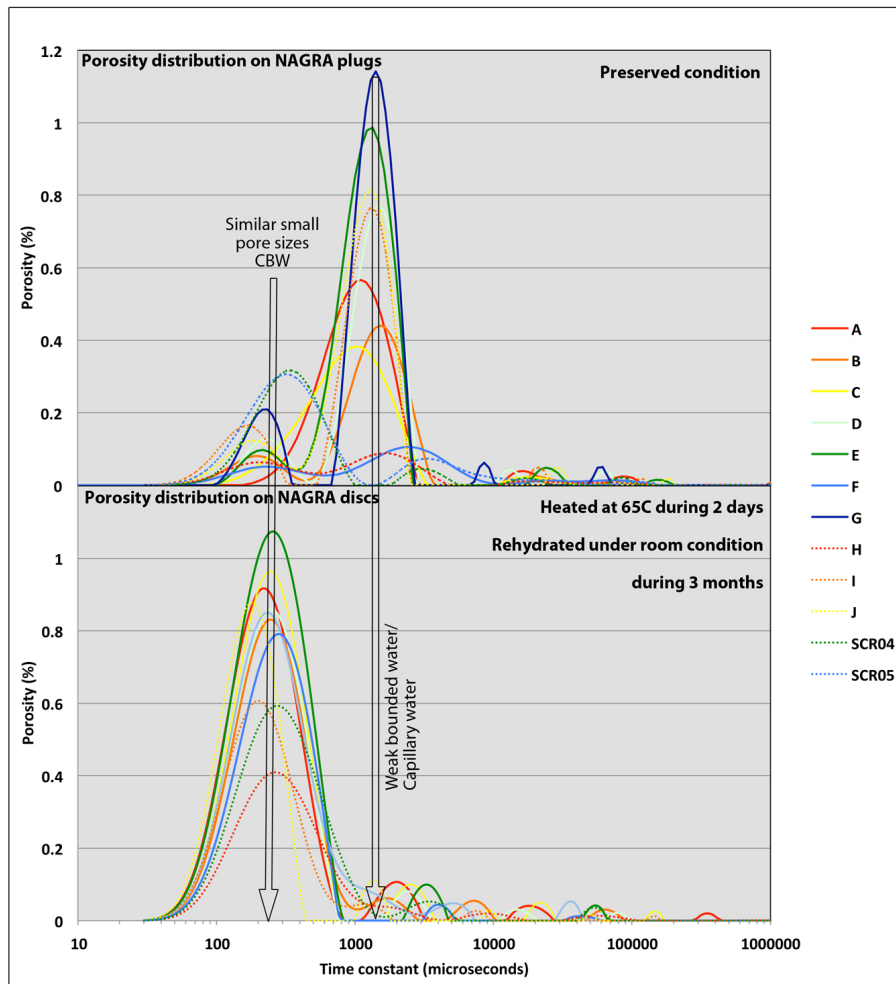


Fig. 4-8: Porosity distribution (%) from all the NAGRA sample collection along the time constant T2 from CPMG NMR method: distribution from preserved (top graph) and distribution from heat treated sample at 65C during 2 days and then rehydrated under room condition during 3 months (Bottom graph). Note how the weakly bound water disappeared after heat treatment whereas the CBW remains. Do not forget that T2 is related to the pore size with increase of the pore size when T2 increases.

The comparison of the computed NMR porosity using the CPMG protocol between preserved plugs and heated discs at 65 °C-rehydrated under room condition during 3 months are presented in Fig. 4-9.

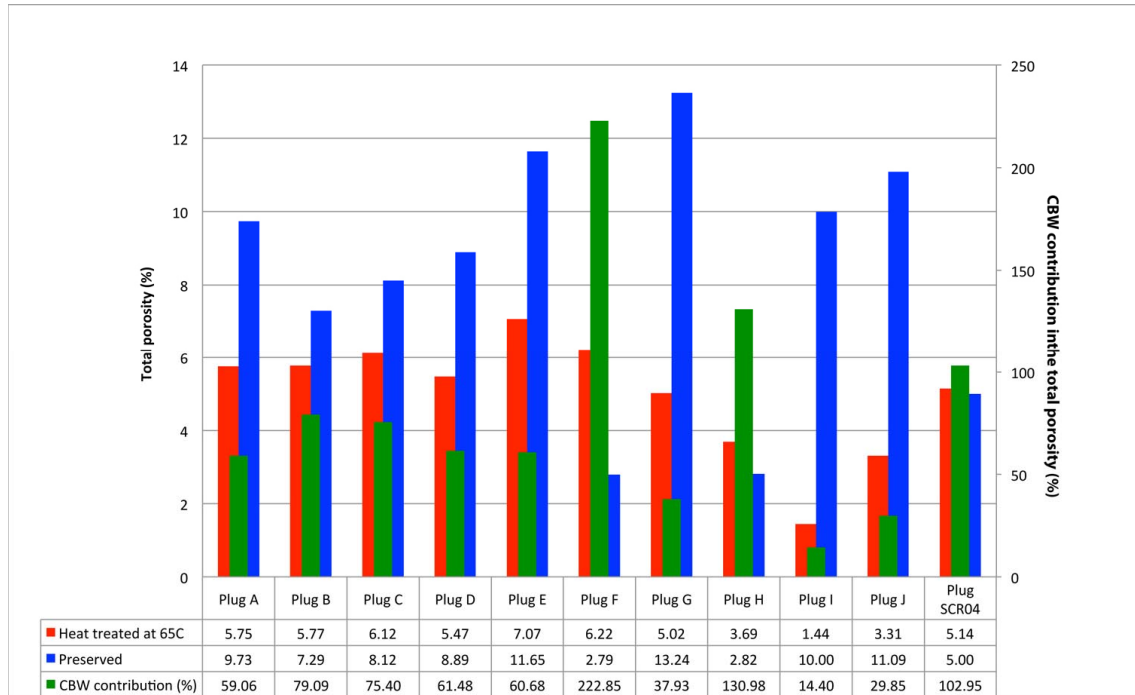


Fig. 4-9: Computed porosity of the NAGRA sample collection under preserved condition (plug samples in blue color), after heat treatment at 65C during 2 days and rehydrated under room condition during 3 months (disc samples in red color). The stick water or the suspected CBW contribution on the total porosity from preserve condition (%) is also presented in green color for each sample. Note the water absorption (CBW > 100%) for the samples F, H and SCR04; or the very low water absorption for the samples G, I and J.

If most of the samples lost ± 40% of their free water, statistically the CBW re-created during the rehydration process (3 months) gives values around 60-80% of contribution on the total porosity recorded by CPMG method.

The CBW contribution is calculated as follows:

$$CBW (\%) = [\text{porosity}_{\text{heat treated}} (\%) / (\text{Porosity}_{\text{preserved samples}} (\%))] * 100$$

The samples G, I and J record very low CBW contribution with values < 30% which should underline a very low content in clays. Interestingly, three specific samples (F, H and SCR04) record CBW contribution above 100% meaning occurrence of hydroscopic clays such as smectites.

We also observed an unexpected dependency of the water content (or porosity) on the sample length for the heated samples (Fig. 4-10a). A specific linear trend of  $y = 0.1x + 14.2$  appears with the highest remaining water porosity for the shortest samples. Intuitively, one should expect the opposite trend if only hydraulic diffusion within a sample and evaporation/condensation at its boundary in relation to heating is assumed to be occurring. At closer inspection, it is in fact surface-to-volume ratio (S/V) that effectively controls the rehydration

process and therefore the corresponding water content evolution with time, i.e., the higher S/V, the faster water content within the samples changes for a given relative humidity in the atmosphere (Fig. 4-10b).

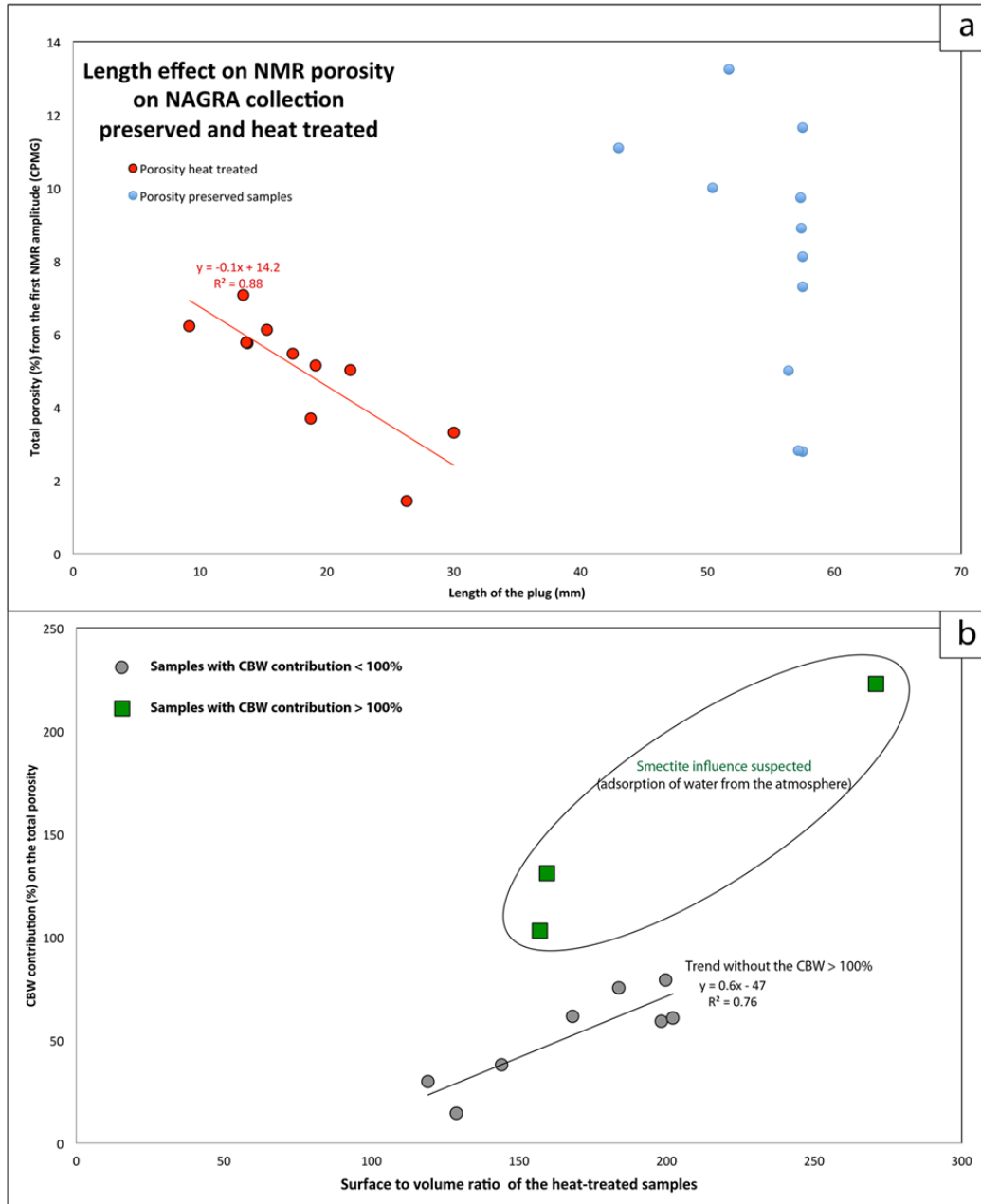


Fig. 4-10: Effect of sample size on the porosity evaluated from NMR CPMG first amplitude. (a) Porosity on the preserved and heat treated samples versus their length. Note the excellent linear trend for the heat treated samples; (b) Relation of the CBW contribution with the Surface to volume ratio of the samples heat treated. Note how the CBW > 100% (potentially smectite rich) are out of the trend.

## 4.2 Dry-wet water mass and grain density

To confirm the NMR water content and derived porosity and density, we performed on preserved discs from all the NAGRA collection a wet-dry weight technique (or evaporation technique). The method consists in weighing each disc under preserved conditions (i.e. water saturated) and weight the sample after drying at a specific temperature. A first test consisted in heating thick discs at 65 °C under vacuum during 24h and 48h. The difference in mass corresponds to water evaporated from the sample. The amount of lost water was also recorded during re-hydration at room condition to evaluate the delay and percentage of water that can be re-attracted after 3 months of exposure, before re-submitting these samples to a higher temperature 105 °C for the amount of time necessary for sample mass stabilization (maximum 1 month):

$$\text{Water content (\%)} = [(M_{\text{preserved sample}} - M_{\text{dry sample}}) / M_{\text{preserved sample}}] \times 100$$

with M corresponds to mass in gram;  $M_{\text{preserved sample}} - M_{\text{dry sample}} = M_{\text{water}} = V_{\text{water}}$  if we use a water density of 1 g/cc.

Derived porosity (%) from water content:

$$\emptyset = [(M_{\text{preserved sample}} - M_{\text{dry sample}}) * 100] / V_{\text{sample}}$$

with V for volume in cm<sup>3</sup>.

A first drying step at 65C followed by second one at 105C allows for the evaluation of the amount of Clay bound water. A 65C heating is also a perfect temperature to limit any chemical transformations between the water and mineral surface, and most of all, it avoids mineral transformation (structure and/or atomic substitution). Indeed, at 65C only the free water and weakly bound/capillary water is removed from the samples. In this context, the CBW remains electro-statically strongly attached to the surface of the clay minerals (so-called stern-layer). The comparison between samples in preserved conditions and after heat treatment at 65 °C provides a mean for estimating the amount of CBW as described in the previous section when comparing the NMR signal of such treated samples. The last heat treatment at 105 °C removes all remaining water (strongly bound).

The three heating tests (65C during 24h, 48h and 105C during 1 month) confirm that 24h heating at 65C already removed > 95% of the total amount of water and 99% after 48h heating when comparing to the 1 month results at 105 °C (Figs. 4-11 and 4-12). Only the samples H and SCR04 retain a bit of water after 48h heating at 65 °C or 105 °C with porosity lost of around 91 % and 94% respectively. Such behavior could refer to strong water bounding to clay such as smectite clays, even though evidence has been reported elsewhere that strongly bound water isn't released until higher temperatures, except in smectite (Handwerker 2011). The porosity lost (Fig. 4-12) during heating process was calculated as following:

$$\text{Porosity lost (\%)} = [\emptyset_{\text{preserved}} - \emptyset_{\text{dried}}] / \emptyset_{\text{preserved}}$$

$$\text{with } \emptyset_{\text{preserved}} = [(M_{\text{preserved}} - M_{\text{dried at 105C after 1month}}] / V_{\text{sample}} * 100$$

$$\emptyset_{\text{dried}} = M_{\text{preserved}} - M_{\text{dried at specific temperature and duration}}$$

The derived bulk and grain density are finally calculated as followed:

$$\text{Wet bulk density (g/cc): } M_{\text{preserved sample}} / V_{\text{sample}}$$

$$\text{Grain density (g/cc): } [M_{\text{preserved sample}} - M_{\text{water}}] / [V_{\text{sample}} - M_{\text{water}}]$$

We considered here a water density of 1 g/cm<sup>3</sup>, so  $M_{\text{water(g)}} = V_{\text{water(ml)}}$ . The  $M_{\text{water}}$  is estimated from the evaporation tests and the NMR CPMG data (preserved condition).

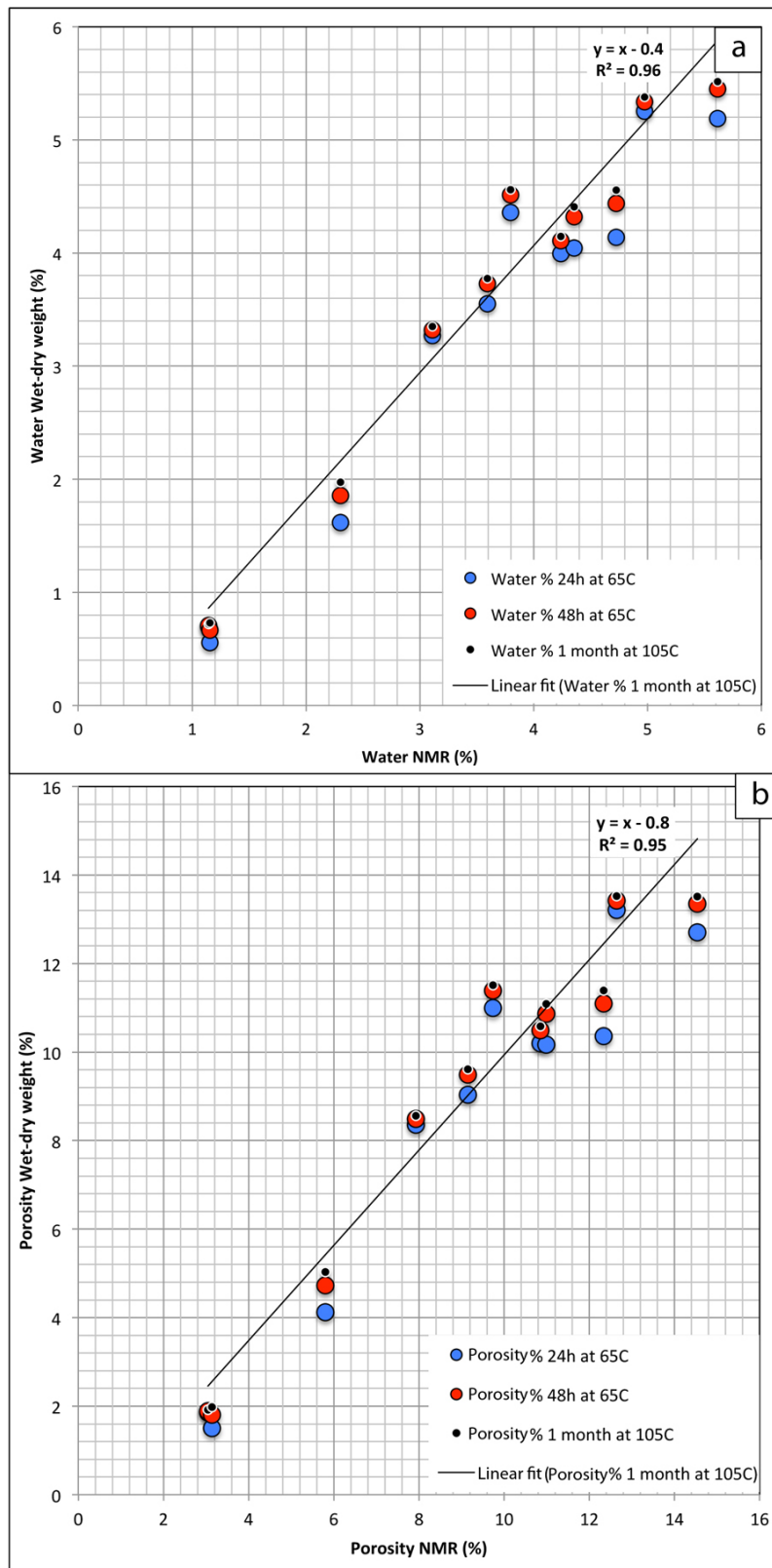


Fig. 4-11: Water from wet-dry method versus NMR CPMG after 24h and 48h oven dried at 65C and 1 month at 105C: (a) water content % and (b) derived porosity (%).

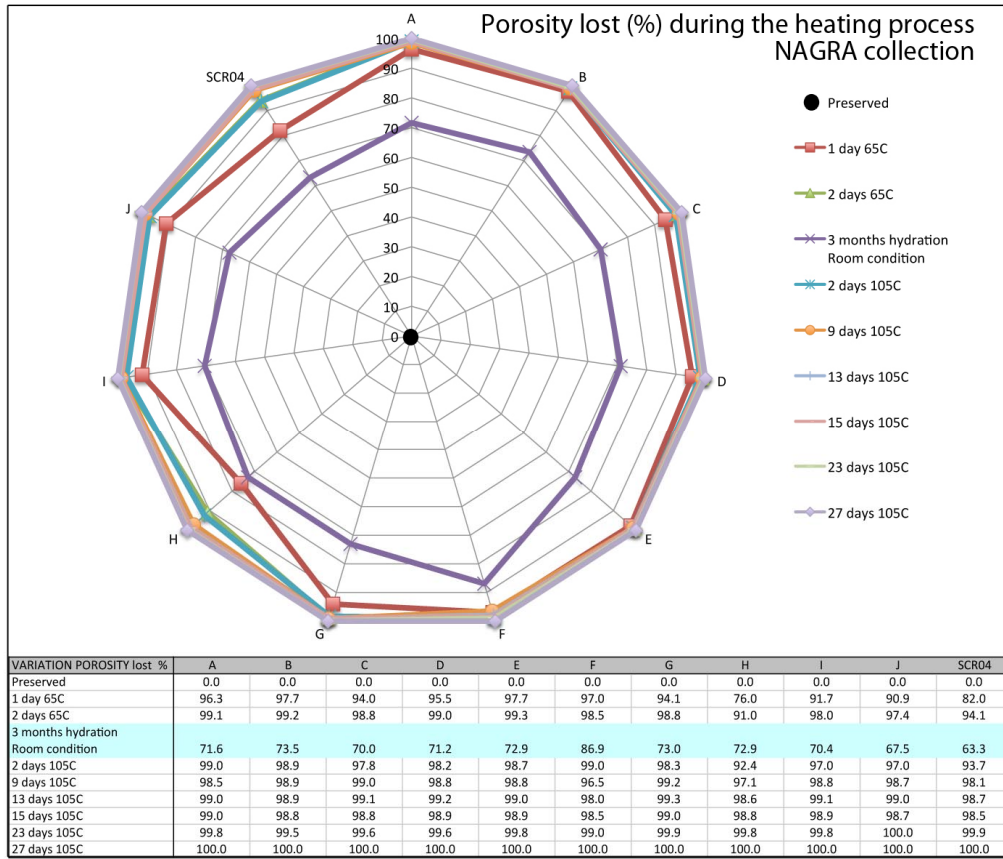


Fig. 4-12: Porosity lost during heating process compare to its related preserved condition during different duration of heating and temperature for each of the SLA-1 samples.

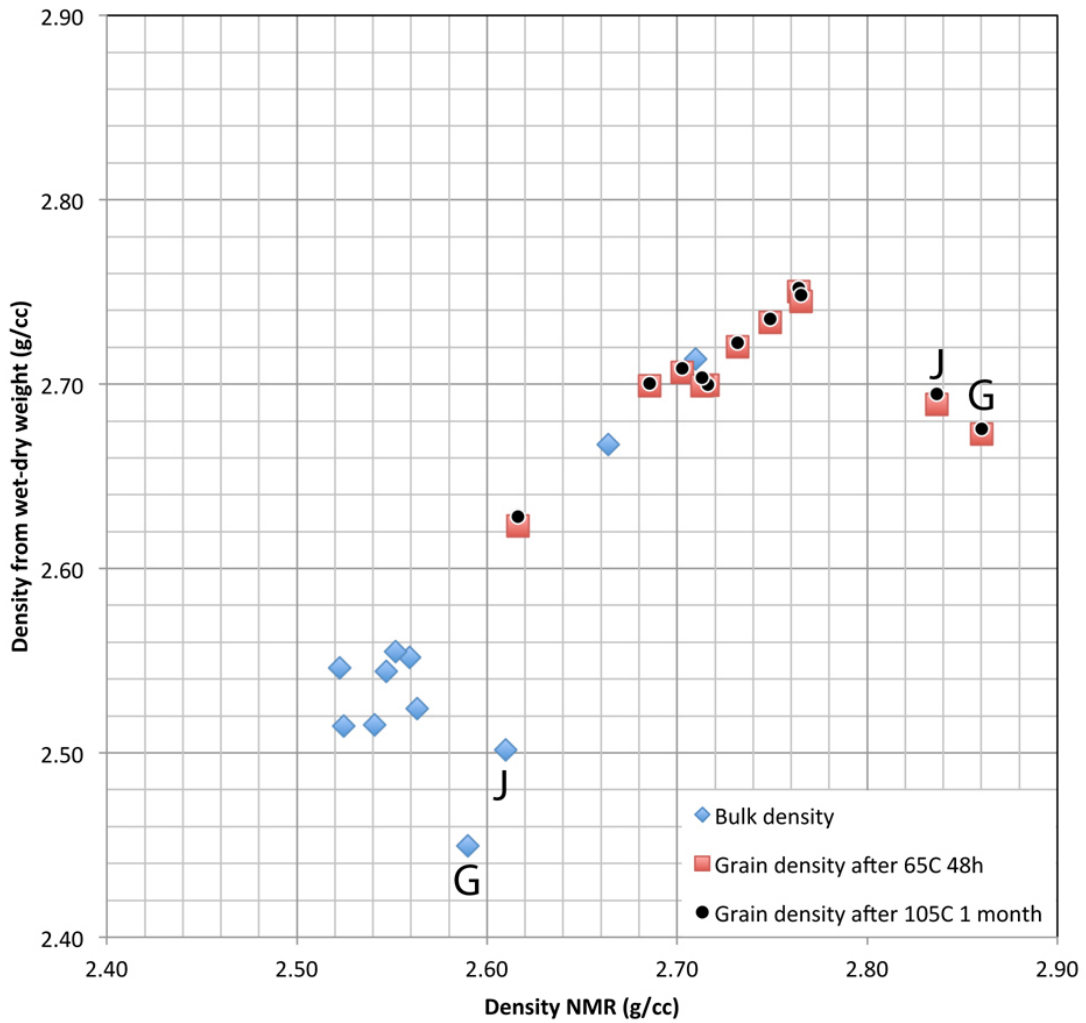


Fig. 4-13: Density calculated from water content on NMR and wet-dry method. The bulk density and grain density derived from these methods show over-estimation from NMR on grain density for the samples J and G as well as an under-estimation on bulk density from wet-dry method and correspond to the richest in clay minerals (see semi-quantitative XRD results: Smectite?).

Mass measurements have been performed after 24h and 48h of drying in order to check if residual water remains after 24h drying and before before a full dehydration under 105 °C was performed for 1 month. We also tested the re-hydration process by keeping the sample at room condition (RH ~ 35%)\_and measuring the weight intake after 20 min, 2 days and 3 months. The re-hydration response of the rock is admittedly controlled by moisture-sensitive clays (smectites).

The rehydration (R%) is calculated as follows:

$$R (\%) = [(M_{\text{rehydrated}} - M_{\text{oven dried}})/M_{\text{oven dried}}]*100$$

where R (%) is the water mass added to the sample from its dry condition,  $M_{\text{rehydrated}}$  is the mass of the sample after rehydration during a specific period of time (20mn, 2 days and 3 months) under room conditions (RH ~35%) and  $M_{\text{oven dried}}$  is the mass of the sample after 48h heating at 65C.

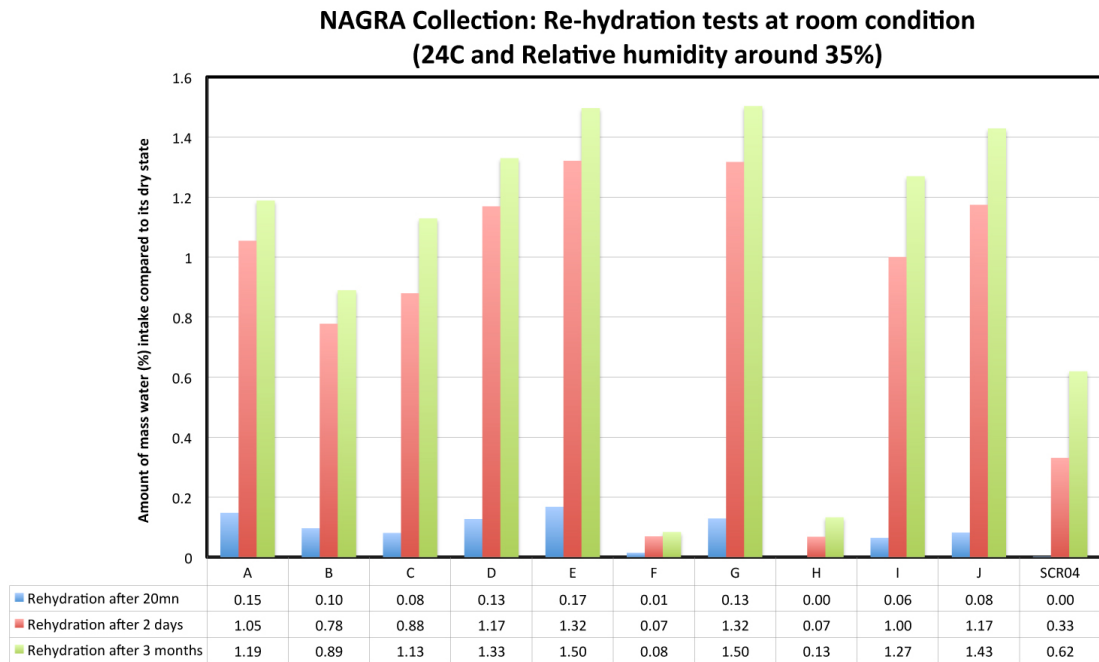


Fig. 4-14: Water re-hydration tests after heating at 65C during 48h and put under room condition 20mn, 2 days and 3 months. The water added by the humidity inside the sample from the room condition (RH at around 35% and 24C) is calculated as % from its dry mass status.

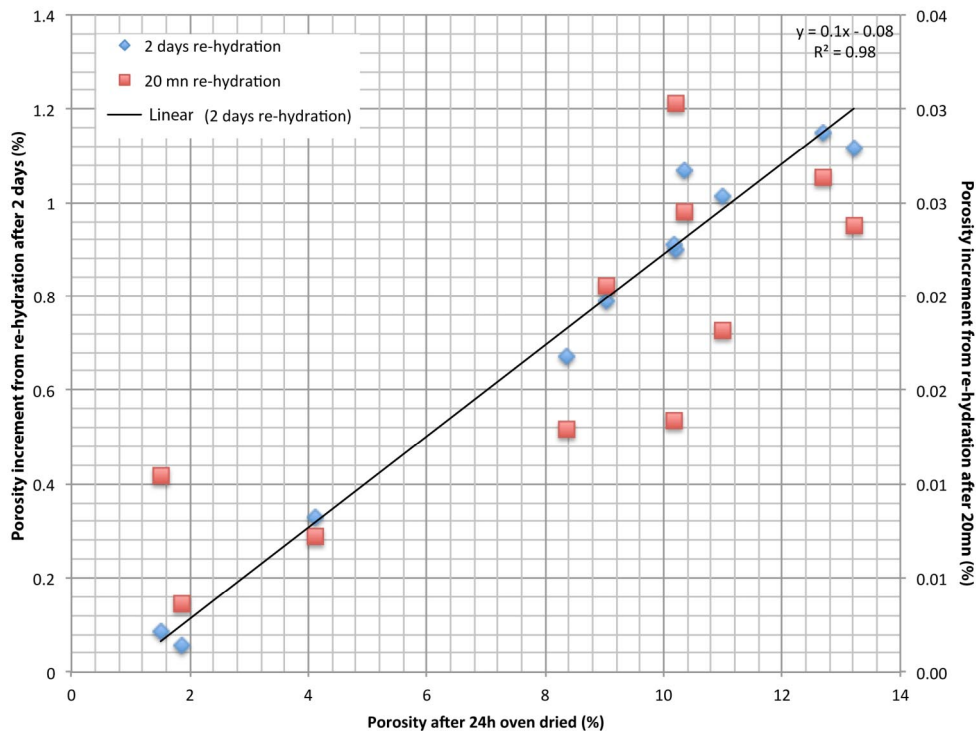


Fig. 4-15: Water re-hydration of samples oven-dried during 48h and the re-hydrated during 20 min and 2 days at room condition.

The water content (Fig. 4-11a) and derived porosity (Fig. 4-11b) after 24h and 48h qualitatively confirm the NMR results, although a slight under-estimation is observed with wet-dry tests as compared to the NMR tests. After 48h drying, residual water remains in the samples (Figs. 4-11 and 4-13). It seems that 24h and most probably even 48h drying is not enough to fully remove all the water from the rock, especially the one strongly attached to clay surfaces. The NMR method to estimate the total amount of water content is therefore more reliable as it does not rely on time-dependent drying process. Note however that the slight difference in water content estimated by the two methods does not affect the calculation of the samples density (Fig. 4-12). Note that 2 samples (G and J) seem to present discrepancies compared to the rest of the dataset. An over-estimation of the bulk density from wet-dry method and under-estimation of the grain density from NMR method could explain such difference.

Monitoring of the de-hydration-re-hydration processes with time (20mn and 2 days) at room conditions give consistent results, i.e., increase of amount of water intake during re-hydration with increasing samples porosity (Figs. 4-14 and 4-15). In all tests, most of the water intake is observed between the 20mn measurement and the 2 days measurement with very little variation afterwards. This confirms the hygroscopic nature of the clays occurring in these samples (probably smectites). If the results of Figs. 4-14 and 4-15 are combined, we can conclude that higher samples porosity implies larger amounts of residual water trapped (most probably by clays). The drying period in the oven is obviously also longer. When part of this water is removed by heating, it is quickly re-adsorbed from moisture in the laboratory’s atmosphere (RH ~ 35%). However, the absolute amount of water intake remains very low, less than 0.15% after 20mn of exposure. This observation implies that samples exposure to room conditions has a weak effect on laboratory sample handling during the petrophysical tests.

### 4.3 Mineralogy analysis

#### 4.3.1 Semi-quantitative XRD analysis

As part of the initial contract, a semi-quantitative XRD analysis was applied to the SLA-1 samples to estimate the carbonate, clay and quartz contents. The method is poorly indicative of quantities of clay and carbonate. Such XRD analysis must only be used as an indication of a dominant mineral phase. Table 4-2 synthesizes the mineral content in each plug sample and confirms the lithology description proposed by NAGRA except for one core: NAGRA-H indicated as a sandy claystone which is almost a pure carbonates (> 80%). The NAGRA-J core (Opalinus Clay, sandy claystone) is the richest in clay minerals and can we described as a shale.

Tab. 4-2: Semi-quantitative XRD analysis on the NAGRA plug samples.

CSIRO-ID	A	B	C	D	E	F	G	H	I	J	SCR04
Depth (m)	761.85	766.15	772.76	773.6	812.59	826.72	853.62	886.6	929.8	946.08	856.09
Total Clays	13	5	11	7	18	2	16	2	17	27	16
Total carbonates	40	59	47	61	21	79	27	87	25	24	25
Quartz	32	29	27	21	37	14	35	8	43	31	38
Total fedspars	16	7	12	8	21	4	19	1	14	16	18
NAGRA type	Marl	Marl	Marl	Carbonate	Shale	carbonate	shale	Shale	shale	shale	shale
CSIRO Type	Marl	Marl	Marl	Carbonate	Shale	carbonate	shale	Carbonate	shale	shale	shale

### 4.3.2 X-ray Diffractometry and Cationic Exchange Capacity methodology

A progress meeting was held in Perth in December 2011, emphasising a review of the preliminary results of the petrophysical and mineralogical characterization program. In this context, CSIRO's semi-quantitative XRD measurements were compared with Nagra's own mineralogical analyses of the Schlattigen-1 core samples (Mazurek 2011). The comparison displayed marked differences between the two. The discrepancies gave rise to a project extension in which CSIRO was requested to perform a full, high level XRD analysis of the core materials. In addition, CSIRO offered to conduct complementary CEC and specific surface area measurements. The experimental protocols and the results are presented in the subsequent paragraphs.

For quantitative XRD analysis, approximately 1.5 g of each oven-dried sample was ground for 10 minutes in a McCrone micronizing mill. The micronized samples were Ca saturated by dispersing the powder in deionized water (to remove excess chloride), then ethanol, and eventually washed twice with 10ml of a 1M CaCl<sub>2</sub> solution (centrifuging between each step). The resulting slurries were oven dried at 60°C then thoroughly mixed with an agate mortar and pestle before being lightly back pressed into stainless steel sample holders.

XRD patterns were recorded with a PANalytical X'Pert Pro Multi-purpose Diffractometer using Fe filtered Co Ka radiation, variable divergence slit, 1° anti-scatter slit and fast X'Celerator Si strip detector. The diffraction patterns were recorded in steps of 0.017° 2 theta with a 0.5 second counting time per step, and logged to data files for analysis. Quantitative analysis was performed on the XRD data from all bulk samples using the commercial package SIROQUANT from Sietronics Pty Ltd. The results are normalised to 100%, and hence do not include estimates of unidentified or amorphous materials.

The cation exchange capacity (CEC) was determined using the Methylene Blue Method (MB) with the tetra sodium pyrophosphate method reported by Wang et al. (1996). Each sample was oven dried at 105°C for several hours before carefully weighing 0.5 g of the clay into 70 ml plastic containers. 50 ml of a 2 % sodium pyrophosphate dispersant solution was added to the containers and vigorously shaken for 10 minutes in a Spex shaker mill. The dispersed clay was transferred with 150 ml of deionized water into a 250 ml conical flask and placed on a heating magnetic stirrer. The samples were gently boiled for 10 minutes then allowed to cool to room temperature. A fresh methylene blue (MB) solution was made by accurately weighing the equivalent of 3.74 g MB (gravimetrically determined to be 3H<sub>2</sub>O) into a 1000 ml volumetric flask and making up to volume with deionized water. The MB solution was transferred into a 25 ml burette placed above the clay suspension. While the clay suspension was being stirred, 0.5 ml of the MB solution was added. Stirring was continued for a minute before a drop of the liquid was deposited onto a filter paper using a small glass rod. A dark blue spot appeared on the filter paper surrounded by a clear liquid halo.

Additional 0.5 ml amounts of the MB were added to the constantly stirred clay suspension before the spot test repeated. This was done until the clear halo turned blue, after which another spot test was performed after stirring a further 2 minutes. If the blue halo disappeared then a further 0.5 ml of MB solution was added to the suspension and the spot test repeated. The end point was obtained when a blue halo remained after stirring for 2 minutes.

### 4.3.3 Principle and methodology of Specific Surface Area measurements

Because we anticipate the dielectric response of rock to be closely related to the specific surface area (as well as CEC), CSIRO has established the experimental instrumentation and procedures to determine SSA. The specific surface is a material property of solids which measures the total surface area per unit mass including internal area of grain boundaries. It is partly related to the grain size distribution and shape but also additional attributes such as grain texture and clay

interlayers in the case of swelling clays (Fig. 4-16). We expect SSA to be a determining factor for the geomechanical properties of the SLA-1 samples.

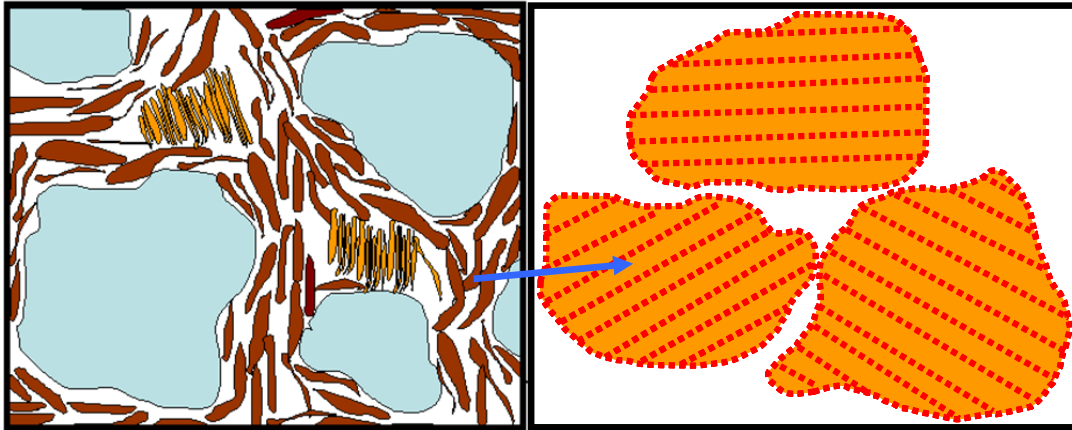


Fig. 4-16: Left) Shales typically are comprised of quartz, feldspar and lithic grains imbedded in an isotropic or anisotropic matrix of clay minerals with a contribution of other possible minerals including carbonates and pyrite. Right) The individual grains of swelling clays have additional surface area within the interlayers which may also be crucial to the petrophysical and geomechanical behaviour of the rock.

Specific surface area was determined using sorption of ethylene glycol monoethyl ether (EGME) (Kellomaki et al., 1987; Vic Roads, 1996; Cerato and Lutenecker, 2002; Tiller and Smith, 1990) which is chosen because of its suitability for investigating interlayer surfaces in swelling clays. Other methods for determining SSA include the use of nitrogen adsorption (sometimes called the BET method), but these methods determine external SSA only and do not cover clay interlayer. Hence they are not discussed in this report. EGME behaves more-like water and is able to penetrate into the same swelling interlayers that water penetrates during hydration. The EGME process essentially works on the principle that mass of the sample increases as a result of the adsorption of a molecular monolayer onto all of the accessible surfaces. The samples are first prepared as a powder and then dried at above 100°C to remove the mobile water. The samples are each quickly weighed and then immersed in EGME and then dried in a carefully prepared atmosphere to draw off the excess EGME and leave behind a monolayer of the EGME compound coating the surfaces. The process requires regular weighing of the samples to monitor the mass change and be sure that the excess EGME is completely removed. Given that a monolayer is created, the mass of EGME which remains with the samples is directly calculable to the specific surface area. The data is then normalised against a set of primary standards and secondary standards are used for quality control.

#### 4.3.4 Results: XRD, CEC and SSA

The lithological rock classification from NAGRA and the previous CSIRO analysis based on semi-quantitative XRD are compared to the new acquired XRD data on the same samples. Tables 4-3a/b display the total fractions of clay, carbonate, quartz and feldspars, along with the classifications of rock types provided by NAGRA and confirmed by CSIRO, respectively. The detailed results of quantitative XRD analysis comprise 12 mineralogical components in total as presented in Table 4-4. The new results give the same rock type results previously discriminated from semi-quantitative analysis at CSIRO. Only the absolute amount of clay, carbonates,

feldspars and quartz differ based on a different sample preparation and method for XRD analyses. The sample H is the only one that does not have the same rock type discrimination between the NAGRA analysis (Shale) and CSIRO (Carbonate). This sample is clearly a carbonate (> 85 wt% of carbonate minerals) as observed in both the semi-quantitative method and the newly reported, fully quantitative, XRD method. New XRD data have been added to the collection on the scratched cores as well (SCR-01, -02, -03 and -05). Cores B and D previously characterized as marls are, with the new XRD results, at the limit to be defined as carbonate types (around 48 wt% carbonate minerals) whereas core A is close to a shale type with 50 wt% of clay minerals. Most of the early interpretations based on mineral content from the semi-quantitative XRD method and their relationship with other petrophysical/rock physical parameters are confirmed. Note that the illite-smectite content (Table 4-4) is likely regular interstratified with approximate composition of 30% smectite and 70% illite layers.

As expected from the XRD analysis (Tables 4-3 and 4-4), the CEC results reflect the dominant mineral content of the rock with low CEC < 10 cmol/kg for carbonate-rich rock types, < 15 cmol/kg for marl rock types, and > 15 cmol/kg for shale rock types.

Tab. 4-3a: Semi-quantitative analysis of the SLA-1 collection with interpretation of the rock type by Nagra and CSIRO, respectively.

CSIRO-ID	Depth (m)	% Total Clays	% Total Carbonates	% Quartz	% Total Feldspars		NAGRA classific.*	CSIRO rock type
Nagra_A	761.85	13	40	32	16		Marl	Marl
Nagra_B	766.15	5	59	29	7		Marl	Marl
Nagra_C	772.76	11	47	27	12		Marl	Marl
Nagra_D	773.6	7	61	21	8		Carbonate	Carbonate
Nagra_E	812.59	18	21	37	21		Shale	Shale
Nagra_F	826.72	2	79	14	4		Carbonate	Carbonate
Nagra_G	835.62	16	27	35	19		Shale	Shale
Nagra_H	886.6	2	87	8	1		Shale	Carbonate
Nagra_I	929.8	17	25	43	14		Shale	Shale
Nagra_J	946.08	27	24	31	16		Shale	Shale
Nagra_SCR1	748.22	N/A	N/A	N/A	N/A		Carbonate	N/A
Nagra_SCR2	770.03	N/A	N/A	N/A	N/A		Marl	N/A
Nagra_SCR3	826.16	N/A	N/A	N/A	N/A		Marl	N/A
Nagra_SCR4	856.09	16	25	38	18		Shale	Shale
Nagra_SCR5	801.53	N/A	N/A	N/A	N/A		Marl	N/A

\* Nagra's (initial) classification based on lithology/sedimentology during core sampling.

Tab. 4-3b: Total fractions of clay, carbonate, quartz and feldspars, derived from the detailed XRD analysis of the SLA-1 collection with interpretation of the rock type by Nagra and CSIRO, respectively.

CSIRO-ID	Depth (m)	% Total Clays	% Total Carbonates	% Quartz	% Total Feldspars	CEC (cmol/kg)	NAGRA classific.*	CSIRO rock type
Nagra_A	761.85	50	27	19	3	12.7	Marl	Shale-Marl
Nagra_B	766.15	24	48	25	3	7.0	Marl	Marl (Mild Carbonate)
Nagra_C	772.76	41	35	20	3	12.7	Marl	Marl
Nagra_D	773.6	32	49	16	2	9.9	Carbonate	Carbonate (Mild Marl)
Nagra_E	812.59	61	11	23	4	16.0	Shale	Shale
Nagra_F	826.72	7	71	21	3	3.3	Carbonate	Carbonate
Nagra_G	835.62	72	5	21	2	18.3	Shale	Shale
Nagra_H	886.6	6	86	7	0	3.3	Shale	Carbonate
Nagra_I	929.8	64	10	24	3	16.4	Shale	Shale
Nagra_J	946.08	72	10	16	2	16.5	Shale	Shale
Nagra_SCR1	748.22	2	95	3	0	2.8	Carbonate	Carbonate
Nagra_SCR2	770.03	53	20	22	4	16.0	Marl	Shale
Nagra_SCR3	826.16	20	33	42	5	6.1	Marl	Marl
Nagra_SCR4	856.09	53	16	27	3	11.7	Shale	Shale
Nagra_SCR5	801.53	42	31	24	2	17.4	Marl	Marl

\* Nagra's initial classification based on lithology/sedimentology during core sampling.

Tab. 4-4: Detailed XRD analysis with CEC and SSA results on the full NAGRA collection.

Sample	Depth (m bg)	Stratigraphy	Calcite	Dolomite / Ankerite	Side-rite	Albite	Microcline / Orthoclase	Pyrite	Anatase	Kaolin	Chlo-rite	Mica / Illite	Illite-Smectite	Qtz	CEC cmol/kg	SSA (m <sup>2</sup> /g)	Analytical SSA (m <sup>2</sup> /g)
A	761.85 - 762.06	Varians	19	8	0	1	2	1	<1	14	1	5	30	19	12.7	89.2	84.2
B	766.15 - 766.52	Varians	46	2	0	1	2	1	<1	6	<1	2	15	25	7.0	41.5	41.4
C	772.76 - 773.00	Parkensoni-Württembergica	31	4	0	1	2	2	<1	11	<1	4	25	20	12.7	80.9	69.8
D	773.60 - 773.90	Parkensoni-Württembergica	45	4	0	1	1	2	<1	8	<1	3	20	16	9.9	58.3	55.4
E	812.59 - 812.86	Wedelsandstein	8	1	2	2	2	1	<1	13	1	7	40	23	15.9	121.5	110.2
F	826.72 - 827.00	Wedelsandstein	69	2	0	2	1	<1	<1	1	<1	0	4	21	3.3	17.5	10.48
G	835.62 - 835.89	Murchisonae	2	<1	2	1	1	1	<1	19	1	7	45	21	18.3	103.5	125.2
H	886.60 - 886.88	Opalinus Clay	85	1	0	0	0	2	0	2	0	0	3	7	3.3	11.9	8.36
I	929.86 - 930.10	Opalinus Clay	8	<1	1	2	1	<1	<1	18	1	8	37	24	16.4	106.3	105.24
J	946.08 - 946.37	Opalinus Clay	8	1	1	1	<1	1	<1	21	1	8	42	16	16.5	110.1	119.04
SCR1	748.22 - 748.62	Effingen Beds	91	4	0	0	0	0	0	2	0	0	0	3	2.8	16.3	0.8
SCR2	770.03 - 770.44	Parkensoni-Württembergica	16	4	0	2	2	2	<1	9	<1	4	39	22	16.0	105.7	104.28
SCR3	826.16 - 826.66	Wedelsandstein	29	4	0	3	2	1	<1	3	<1	3	13	42	6.1	26.0	35.76
SCR4	856.09 - 856.40	Opalinus Clay	11	1	4	2	1	1	<1	14	1	5	33	27	11.7	68.4	91.76
SCR5	801.53 - 801.93	Blagdeni	30	1	0	1	1	2	<1	3	<1	2	36	24	17.4	87.3	93.12

The major contributors to SSA are illite-smectite, which typically accounts for 20 – 40 %, Kaolinite (SSA = ~ 40 m<sup>2</sup>/g) which typically accounts for 0 – 20 % and illite-mica which typically accounts for 0 - 8 %. Other minor constituents in the SLA-1 samples include calcite and dolomite, which are present in significant amounts in approximately 1/3rd of the samples. Published values of SSA for smectite are typically 700 m<sup>2</sup>/g, and Illite ranges from 10<sup>3</sup>s – 100<sup>3</sup>s m<sup>2</sup>/g (Kellomaki et al., 1987; Cerato and Lutenegger, 2002; Tiller and Smith, 1990). We except a value of SSA for illite of 60 m<sup>2</sup>/g, based on measurements of Ward illite (68 % illite and 28 % quartz from XRD). Typical SSA for the Nagra samples is the vicinity of 100 m<sup>2</sup>/g (Table 4-4), which would be rather low if the mixed layer illite-smectite were in fact a pure smectite end member; however, a lower value is attributable to the approximate composition of 30% smectite and 70% illite in the regularly interstratified mixed layer illite-smectite. Apart from direct measurement of the specific surface area using EGME, it is also possible to obtain an approximate value of SSA (Analytical SSA or An. SSA) using the mineralogical constituents determined from XRD. The XRD based analytical expression that we use is based on published and commonly accepted values of SSA for the existing minerals:

$$\text{Analytical SSA} = 700 * \% (\text{Illite-Smectite}) + 60 * \% (\text{Mica-Illite}) + 40 * \% (\text{Kaolinite}) \quad [\text{Eq. 1a}]$$

Taking into account the probable illite-smectite ratio of 70-30, equation 1a becomes:

$$\text{An. SSA} = 700 \times 0.3 \% (\text{Illite-Smec}) + 60 \times \% (\text{Mica-Illite}) + 0.7 \times \% (\text{Illite-Smec}) + 40 \times \% (\text{Kaolinite}) \quad [\text{Eq. 1}]$$

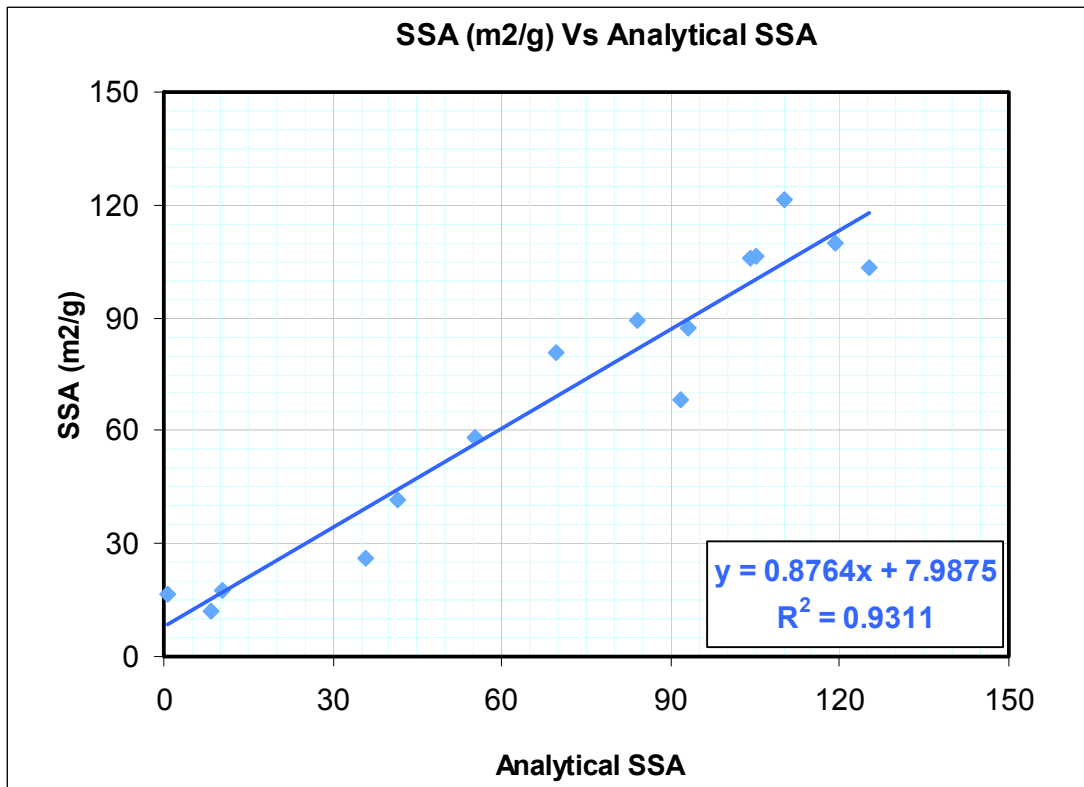


Fig. 4-17: The correlation observed between specific surface area determined by direct measurement in the laboratory using the EGME method and an indirect method analytically determined from XRD mineralogy. There is a good correlation between the analytical SSA determined using XRD and the measured value from sorption of EGME.

The correlation between Analytical SSA and measured SSA is very strong (better than 93%). Fig 4-17 displays the strength of the correlation which lends support to the validity of both the SSA data and the XRD data: two completely different measurement methods have been used to determine the SSA. One based on published direct measurement procedures using the EGME method and a second determination based on analytical values and XRD.

#### 4.4 Electrical properties at low frequency

When properly calibrated, electrical properties at low frequency (< 10 MHz) are usually a good parameter to track fluid saturation and cracks network that could be connected through the whole sample (or formation). The electrical resistivity (or at the opposite, the electrical conductivity) is a classical parameter that can help log calibration to estimate water saturation and porosity profile along a well. Because the electrical properties are frequency dependent as well as the temperature, having a broad range of frequency spectrum for electrical resistivities (or conductivities) can help to better choose the most appropriate frequency for specific electrode configuration to only record water signal instead of conductive mineral effects (metals, iron-sulfides or iron-oxides) or electrode polarization... Most of the electrical logging tools work at 1 kHz and derivative porosity can be extracted through the basic empirical Archie's law (Archie, 1942):

$$C = \frac{1}{a} \cdot C_w \cdot \phi^m \cdot S_w^n$$

with C for the electrical conductivity of the fluid saturated rock (or 1/C for the electrical resistivity),  $\phi$  for porosity,  $C_w$  for the electrical conductivity of the brine,  $S_w$  is the brine saturation, m is the cementation exponent of the rock (usually between 1.5 and 2 in rocks), n is the saturation exponent (usually 2) and the constant "a" is the tortuosity factor.

The resistivity can then be expressed as followed:

$$R = \frac{a}{\phi^m} \cdot \frac{R_w}{S_w^n}$$

with R for the fluid saturated rock and  $R_w$  for the brine resistivity. But if the rock is fully water saturated R becomes  $R_0$  as the resistivity of the rock for a fully saturated condition ( $S_w=1$ ) and the previous equation becomes the Formation factor (F):

$$R = F = \frac{a}{\phi^m} = \frac{R_0}{R_w}$$

#### 4.4.1 Experimental methodology

Electrochemical Impedance Spectroscopy (EIS) is a measure of the resistivity of the rock in low frequency broadband to evaluate the inductive and/or conductive aspects of the rock under a specific brine saturation. The instrument used to measure impedance for low frequency measurements is an Autolab FRA 30 potentiostat-frequency response analyser made by Ecochemie (Netherlands). The instrument can measure impedance in 2, 3 or 4 electrode configuration over a very wide range, from milliohms to Gigohms, in the frequency range  $10^{-4}$  Hz to 1 MHz. In two electrode mode, the current electrodes are used to detect the potential as well as inject current. While this can lead to electrode polarization problems, it is a useful quality control step to always make both two and four electrode measurements. A typical measurement cycle commences with a measurement of the brine-filled cell. This should return the known value for brine resistivity when corrected for temperature (monitored continuously with a PT100 resistance element), and zero signal phase.

The measurements for this study were generally made using 31 logarithmically distributed frequencies in the range 1 Hz to 1 MHz. The data above 10 kHz were not used in the analysis because of capacitive effects appearing at the electrode interface. The raw measurements are collected in terms of spectra of impedance magnitude (ohms) and phase angle (degrees). Brine is not dispersive and has a flat spectrum of impedance with frequency below 1 MHz. Clean sands have an almost flat impedance spectrum with phase angles less than 0.5 degrees at low frequency. The presence of conducting inclusions is apparent in an elevated phase angle and complexity of the shape of the impedance spectrum. Clays depress impedance at low frequency and can be manifest as relatively large phase angles or peaks in the phase angle. This is principle behind impedance spectroscopy. While impedance spectroscopy is a frequency domain technique, we also routinely measure the time stability of the measurements by conducting time scan acquisitions at three spot frequencies (100 Hz, 1kHz and 10 kHz) as we set up and condition the samples inside the cell. Again, this monitoring is very important to ensure reliable and repeatable results. When under confining pressure, the small cracks close and the time scan shows an increase of resistivity until stabilisation. When we reach the stabilisation, we can start the electrical spectrum recording under this confining pressure. That is why it is always important to record time scan when pressure is applied to be sure of the relevant stress environment and electrical signal.

The sample cell used was a new custom designed two and four electrode core holder capable of applying an overburden pressure to the samples of up to 5000 psi under water/brine saturation (Fig. 4-18). However, measurements in this study were all made under ambient conditions (100 psi confining pressure) for reasons of speed. Two ultrasonic transducers are also integrated in the middle of the electrodes to perform ultrasonic Vp-Vs measurements during the electrical tests with or without confining stress along the core axis only. This Vp-Vs are equivalent to benchtop method along the axis of the plug but offers the advantages to record with confining pressure, under saturation and recorded simultaneously with electrical properties. The electrode configuration consists of solid silver disc electrodes carrying current placed at each end platen, and silver wire ring electrodes picking up the electrical potential circumferentially, at a spacing of 25mm located symmetrically in the middle section of the sample. The electrochemical behaviour of silver in brines is significantly better than that of other metals such as steel, copper, brass or bronze.

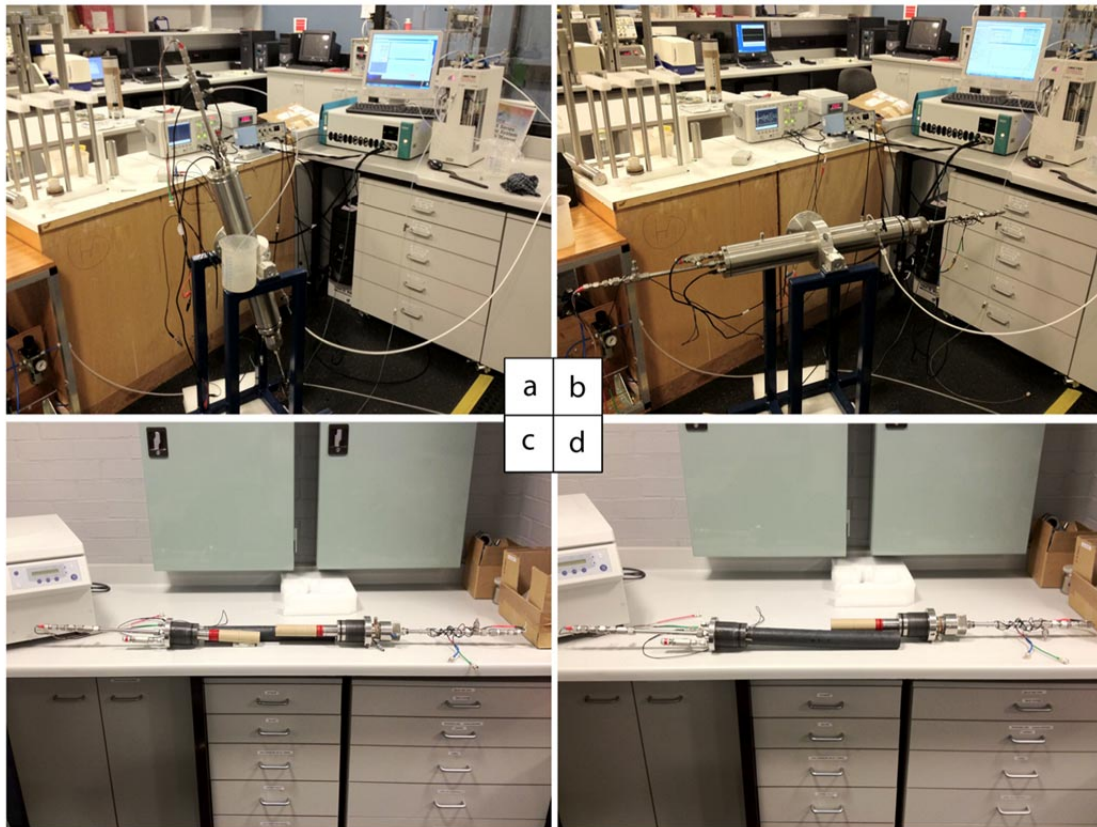


Fig. 4-18: New electro-acoustic rig to perform low frequency electrical resistivity spectrum and axial ultrasonic records under confining stress and fluid saturation. (a) Cell under brine filling to remove the air bubbles; (b) cell ready for measurements; (c) electrodes with transducers and spacers (in red) to adapt the length of the sample; (d) Sleeve with 2 electrode rings in its middle and inserted in one of the electrode part.

#### 4.4.2 Pore water salinity

To measure the impedance of each plug, the pre-saturated sample was placed into the core holder, which was assembled and flooded with brine to remove any trapped air. Two-electrodes and four electrodes impedance spectra were recorded without confining pressure to evaluate the resistivity with potential cracks. Then the confining pressure was applied and a time scan was recorded in four electrodes configuration until stabilisation. After stabilisation, the 2 and 4 electrodes impedance measurements spectra were repeated. The sample was unloaded and the brine drained out to be collected. The brine used in this exercise was based on the NAGRA description for artificial pore water (Traber 2011). We spent a bit of time in this pore water salinity because of issues of shale/marl/carbonate stability in such brine. It appeared that some samples after testing under brine were completely destroyed. After applying the synthetic pore water, the conductivity was around 19.25 mS/cm (equivalent NaCl).

We calculated the theoretical electrical conductivity of such artificial porewater (Tables 4-5 and 4-6):

Tab. 4-5: Recipe for the pore water NAGRA collection (from Report AN 11-159). Note that the mass correction of kg/kg of water as volumetric units of kg/L of water is ignored because of a negligible deviation smaller than analytical uncertainties.

Component	g/kg H <sub>2</sub> O
NaCl	6.7356
NaHCO <sub>3</sub>	0.0456
CaCl <sub>2</sub> 2H <sub>2</sub> O	1.7510
KCl	0.1902
MgCl <sub>2</sub> 6H <sub>2</sub> O	1.8635
Na <sub>2</sub> SO <sub>4</sub>	3.4089

The electrical conductivity of such artificial pore water can be calculated based on molar ionic conductivity at room conditions (Table 4-6):

Tab. 4-6: Electrical conductivity (I) from anion/cation. Database compiled from Shugar and Dean, 1990; Atkins, 1986; Berezanski, 1997; Sawyer et al., 1995; Holler and Enke, 1996.

Cations	H <sup>+</sup>	Ca <sup>2+</sup>	K <sup>+</sup>	Na <sup>+</sup>	Mg <sup>2+</sup>
I at 25C(mS.m <sup>2</sup> .mol <sup>-1</sup> )	34.96	11.9	7.35	5.011	10.612

Anions	OH <sup>-</sup>	SO <sub>4</sub> <sup>2-</sup>	Cl <sup>-</sup>	NO <sub>3</sub> <sup>-</sup>	HCO <sub>3</sub> <sup>-</sup>
I at 25C(mS.m <sup>2</sup> .mol <sup>-1</sup> )	10	16	7.63	7.14	4.45

The electrical conductivity of a saline solution is:

$$S_i = \sum I_i \cdot [C]_i$$

with I the molar ionic conductivity of the cation and/or anion and C its concentration. So, The electrical conductivity of the artificial pore water is then as following:

$$S = ([NaCl] \times 5.011 \times 7.63) + ([NaHCO_3] \times 5.011 \times 4.45) + ([CaCl_2 \ 2H_2O] \times 11.9 \times 2 \times 7.63) + ([KCl] \times 7.35 \times 7.63) + ([MgCl_2 \ 6H_2O] \times 10.612 \times 2 \times 7.63) + [Na_2SO_4] \times 2 \times 5.011 \times 16)$$

$$S = 1435.58 \text{ mS.m}^{-1}$$

$$S_{\text{theory}} = 14.35 \text{ mS.cm}^{-1}$$

$$S_{\text{measured}} = 19.25 \text{ mS.cm}^{-1}$$

Our brine preparation is in the same range of conductivity with a slight over-estimation, which is good to limit destruction from swelling etc. In parallel, we conducted pore water extraction from the NAGRA samples. Powders from NAGRA samples were prepared from cuttings after removing the oil film using dichloromethanol (DCM) and dried under 65°C. The dried samples were immediately crushed to create a fine powder. 10g of each shale powder were then mixed with 25 ml of DI water. These preparations were done on 2 similar set: (i) for short chemical equilibrium of around 5-10 mn and (ii) regularly shaken during 2-3 days for longer chemical equilibrium. After centrifugation, the extracted brines (Fig. 4-19) were immediately measured for their electrical conductivity to calculate the salinity of the pore water on a portable Orion conductivity meter probe (Orion 550, 4 electrode pH/conductivity meter). The results are summarized in Table 4-7.



Fig. 4-19: Brine extraction from NAGRA samples after centrifugation. Note the different colors of the brine due to occurrence of organic matter (yellowish color) and in some of the sample a black oil film at the surface of the water also related to oily organic matter.

Tab. 4-7: Results of salinity and electrical conductivity of the brine extracted from the NAGRA sample collection.

Sample name	CSIRO ID	Conductivity brine µS/cm	Obs brine extracted	Obs substrat	Salinity dilution corrected (g/l NaCl)	Conductivity corrected (mS/cm)
Nagra-761.85m-fast	A	1026	Yellow	Thin black film on top of dark grey	11.32	19.75
Nagra-766.15m-fast	B	817	Strong Yellow	Thin black film	8.95	15.72
Nagra-772.76m-fast	C	1046	Slight yellow with slight oil film	Very thin black layer	11.54	20.10
Nagra-773.6m-fast	D	876	Yellow with oil film	Thick layer of black	9.62	16.99
Nagra-812.59m-fast	E	1024	Yellow with slight oil film	Thick black layer	11.25	19.63
Nagra-826.72m-fast	F	715	Super clean with lots of oil film	No black layer and light grey	7.82	14.01
Nagra-835.62m-fast	G	1403	Super clean with lots of black oil film	Very thick black layer	15.59	26.52
Nagra-886.6m-fast	H	952	Very clean	No black layer in light grey	10.47	18.37
Nagra-929.86m-fast	I	1011	super yellow with lots of black oil film	Thin black layer	11.13	19.44
Nagra-946.08m-fast	J	1050	Slight yellow with lots of blackish oil film	Black lauer	11.59	20.18
Nagra-856.09m-fast	SCR04	1573	Clean with slight oil film	No black layer in dark grey	17.54	29.54
Nagra-761.85m-long	A	1272	Very slight yellow	Thick black film on top of dark grey	14.02	24.06
Nagra-766.15m-long	B	981	Strong yellow	Very thin black film	10.81	18.92
Nagra-772.76m-long	C	1203	Clean	Thin black layer	13.28	22.89
Nagra-773.6m-long	D	1120	slight yellow	Thick black layer	12.40	21.47
Nagra-812.59m-long	E	1112	Very clean	Very thick black layer	12.27	21.27
Nagra-826.72m-long	F	930	Super clean	No black layer in light grey	10.21	17.96
Nagra-835.62m-long	G	1537	Super clean	Ultra thick layer black	17.18	28.98
Nagra-886.6m-long	H	1168	Very clean	No black layer in light grey	12.94	22.34
Nagra-929.86m-long	I	1166	Very clean	Black layer	12.92	22.31
Nagra-946.08m-long	J	1158	Slight yellow	Black layer	12.79	22.11
Nagra-856.09m-long	SCR04	1892	Clean with slight oil film	No black layer	21.26	35.22

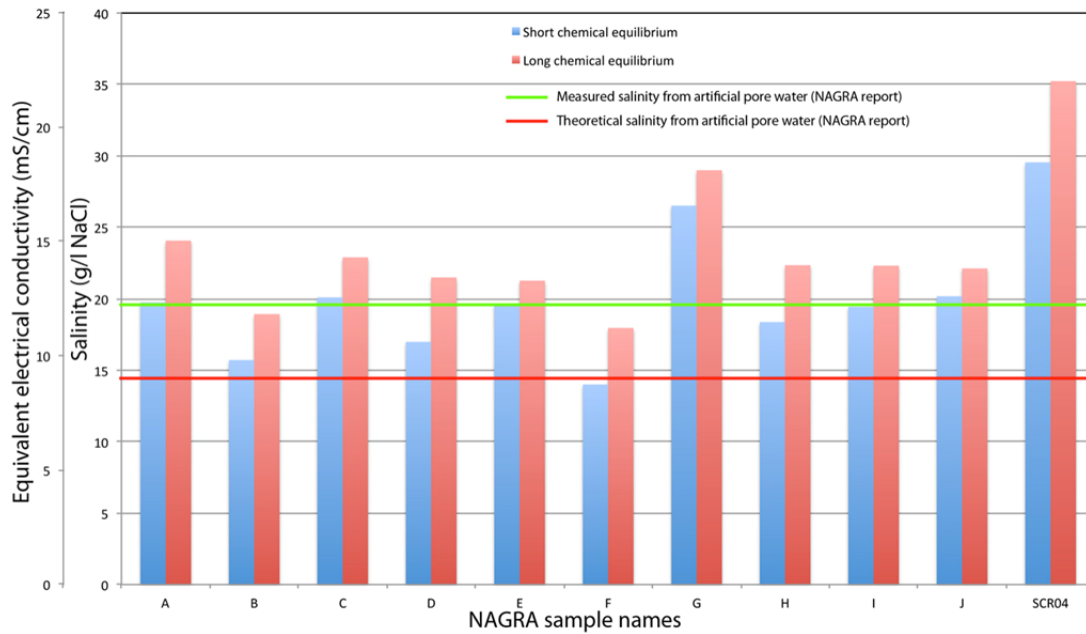


Fig. 4-20: Histograms of the pore water salinity in each NAGRA sample. Note the perfect match between the artificial brine from NAGRA and the extracted brine from each sample with some few exceptions: NAGRA-G and SCR04 (higher) and NAGRA-NAGRA-B-D and -F (lower).

The 2 batches (few minutes days and 2-3 days) give the same shift of  $\pm 16\%$  difference between the short and long time of chemical equilibrium. The long time results are quite close to the "measured artificial pore water" (Fig. 4-20). Despite the good match some samples were destroyed after electrical tests under synthetic brine saturation. It is then worth to test such samples in sea water brine to get read of the uncertainties on chemical and swelling effects for future tests (not the case in this exercise).

#### 4.4.3 Results

The saturated resistivities  $R_0$  (corrected to  $25^\circ\text{C}$  using Arps' equation; Serra, 1984) are cited for a single frequency of 1 kHz. The Arp's equation is used for a constant solution that saturate the sample (i.e. brine of 19.25 mS/cm supposedly the salinity of the fluid filling the pores in these SLA-1 samples):

$$R_1(T_1 + 21.5) = R_2(T_2 + 21.5)$$

with T in degree C;  $T_1$  is the targeted temperature correction of  $25^\circ\text{C}$  in our case,  $R_1$  is the resistivity corrected from the temperature and  $R_2$  is the measured resistivity at the  $T_2$  lab temperature.

$$\text{So } R_1 \text{ (ohm.m)} = R_2(T_2 + 21.5)/(T_1 + 21.5)$$

This is common practice (see Lasswell 2006), as for many rock brine systems, the minimum in the phase angle between electrical current and potential is found to lie at around 1 kHz. This was the case for all the samples tested: at 1 kHz essentially a "resistivity" is being measured,

and the difference between the two electrode and four electrode resistivities is small. In fact, this is an excellent quality control check. We also performed the measurements under three distinct voltage excitations (10 mV, 100 mV and 200 mV) on few samples to check the sensitivity limits of the acquisitions and the linearity of the system. Note that the resistances differ in the data tables because while the 2 electrode configuration measures through the whole length of the plug (around 55 mm typically), the 4 electrode method only measures the impedance between the central section between the ring electrodes (25 mm).

We started the sequence with no confining pressure recording Vp-Vs and electrochemical spectrum from 1Hz to 10 kHz with 2 and 4 electrodes. Then we started a Time scan of three frequency (100 Hz, 1 kHz and 10 kHz) using 4 electrodes tracking the evolution of the impedance when applying a confining pressure of 100 Psi. When the impedance stabilised under the new stress, we then recorded the resistivity spectrum in 2 and 4 electrodes as well as Vp-Vs. Figure 4-21 gives an example of testing different voltage excitation on the impedance spectrum without confining pressure.

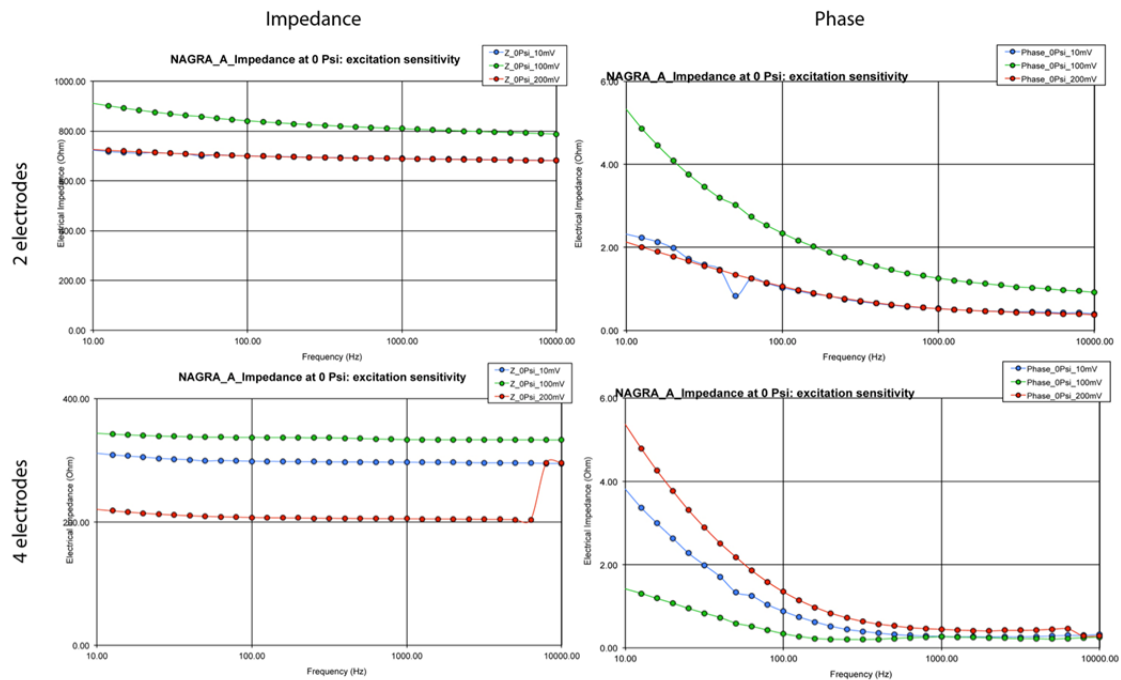


Fig. 4-21: Electrical spectrum on NAGRA-A with 2 and 4 electrodes under no confining pressure.

After temperature and length correction, we obtain a resistivity spectrum in ohm.m very flat for most of the sample. Example for NAGRA-A is provided in Fig. 4-22. The other similar plots and data are available in the file : EIS/NAGRA\_EIS\_analysis.

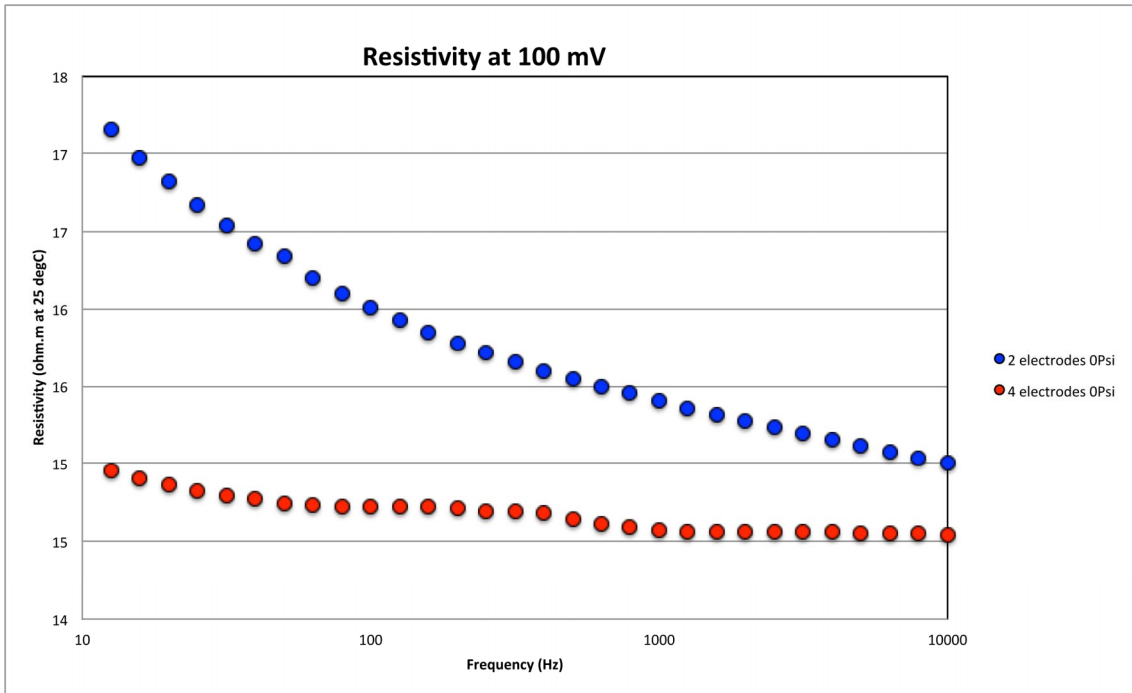


Fig. 4-22: Resistivity spectrum on NAGRA-A at 2 and 4 electrodes with no confining pressure.

The time scan under 4 electrodes during confining pressure shows on example NAGRA-B (Fig. 4-23) a stabilisation of the resistivity after 1000 s (i.e. 16 mn).

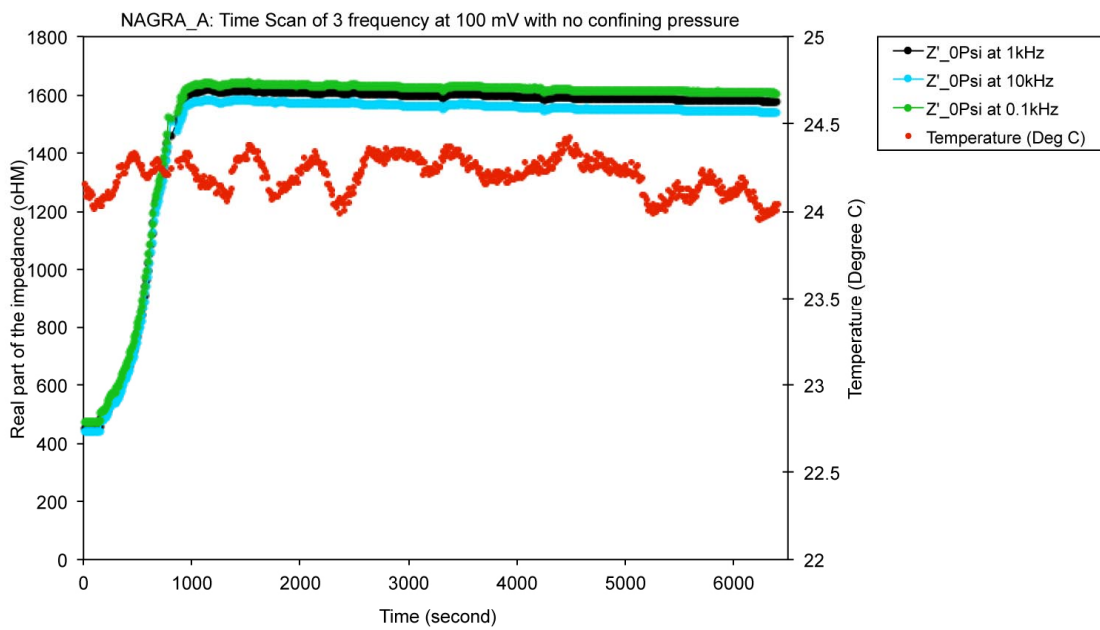


Fig. 4-23: Time scan of the electrical impedance at three frequency (100Hz, 1 kHz and 10 kHz) with temperature on NAGRA-B.

With confining pressure, the spectrum remains very flat but shift toward higher resistivity due to bedding/cracks closing effect by the stress (example Fig. 4-24) which takes in this example 1000 seconds. Surprisingly, there is a factor 2 to 4 between the 2 and 4 electrodes.

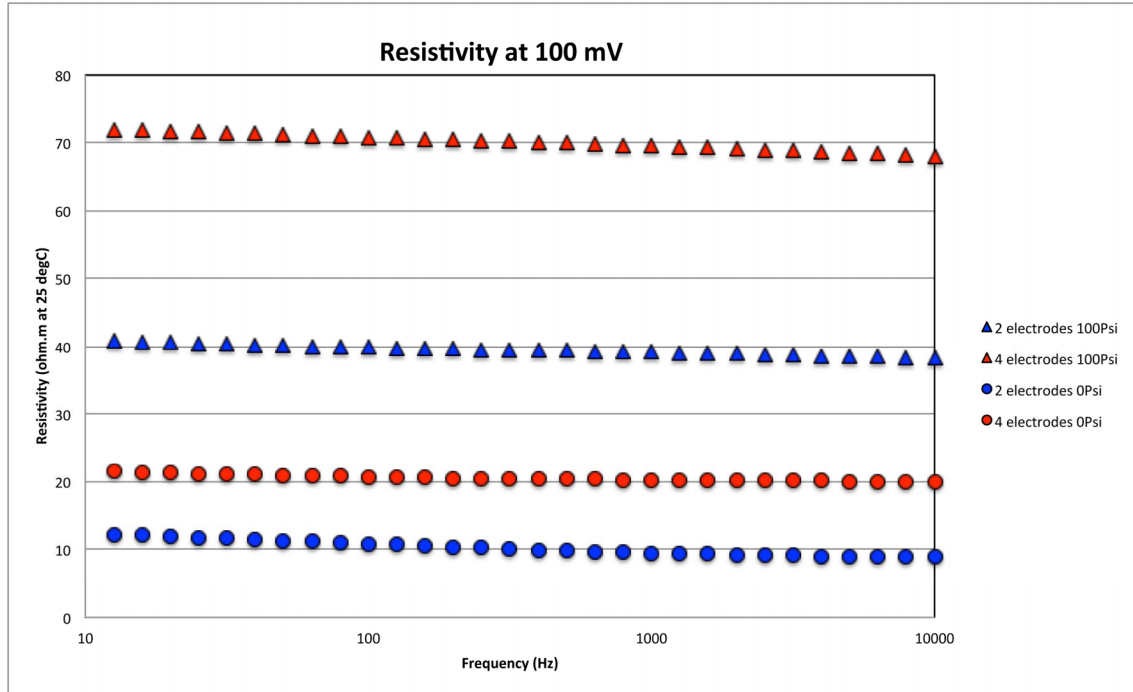


Fig. 4-24: Resistivity spectrum with and without confining pressure on 2 and 4 electrodes for the NAGRA-B.

We synthesize the results of resistivity at 1kHz in the following Table with Archie's law data (see introduction for equation details) using the porosity from NMR (averaged from the three methods) and the brine conductivity from NAGRA recipe measured in laboratory (i.e. 19.25 mS/cm) (Table 4-8):

Tab. 4-8: Electrical resistivity results from the NAGRA plugs.

Sample #	Depth (m bg)	Resistivity at 1 kHz 2 electrodes (Ohm·m)	Resistivity at 1 kHz 4 electrodes (Ohm·m)	Resistivity at 1 kHz / average (Ohm·m)
B	766.15-766.52	39.13	69.53	54.33
C	772.76-773.00	53.88	-	53.88
D	773.60-773.90	54.72	59.31	57.01
E	812.59-812.86	22.29	23.05	22.67
F	826.72-827.00	335.24	661.91	498.57
G	835.62-835.89	40.62	71.79	56.20
H	886.60-886.88	584.43	292.78	438.61
I	929.86-930.10	38.99	27.41	33.20
J	946.08-946.37	46.21	62.18	54.20
SCR04	856.09-856.40	544.30	70.00	57.15

The samples NAGRA-F and -H are highly resistive around 300-600 ohm.m whereas the others remain around 30-50 ohm.m. Note that sample A was measured only at 0 Psi because it destroyed inside the cell before to apply the confining pressure. The brine was clearly not good for it. A problem of 4 electrodes appeared on the sample C and could not be repeated because of destruction as well of the sample by the brine.

In fact, the samples A, C, D, F, I and SCR04 were discing and breaking after electrical tests under synthetic brine. We think such brine is not reliable enough to be used as an equilibrated brine for all the NAGRA collection.

We also computed some archie's parameters [dimensionless] to give the tortuosity, cementation exponent and formation factor (Table 4-9 and Fig. 4-25) with the following formulae (as presented in the introduction of this section):

$$\text{Formation factor: } F = \frac{a}{\Phi^m} = \frac{\text{Resistivity of the rock (supposedly fully saturated)}}{\text{Resistivity of the brine}}$$

(Resistivity of brine: 19.25 mS/cm).

$$\text{Cementation m exponent: } m = \frac{1}{\Phi} \log \frac{F}{a}$$

with  $\phi$  from NMR on preserved plugs (averaged from the three NMR methods using the first amplitude)

$$\text{Tortuosity: } a = F \cdot \Phi^{-m}$$

Tab. 4-9: Archie's parameters computed from electrical resistivity at 1 kHz under 100 psi confining pressure and brine saturation of 19.25 mS/cm.

Sample	Formation factor 2 electrodes	Formation factor 4 electrodes	Archie m exponent 2 electrodes	Archie m exponent 4 electrodes	Achie tortuosity 2 electrodes	Achie tortuosity 4 electrodes
A						
B	8	13	0.6	0.8	221.6	393.7
C	10		0.7		260.6	
D	11	11	0.7	0.8	254.4	275.7
E	4	4	0.5	0.5	73.6	76.1
F	65	127	1.0	1.1	5121.7	10112.5
G	8	14	0.7	0.9	126.9	224.3
H	113	56	1.1	1.0	7550.6	3782.6
I	8	5	0.7	0.5	155.4	109.2
J	9	12	0.7	0.8	171.1	230.2
SCR04	9	13	0.6	0.8	269.0	425.1

We remind that Archie's parameters must be taken with extreme precaution. In permeable rocks such as sandstones, Archie's EMPIRICAL law is working quite well. But in shales with very low permeability, the electrical conductivity can become dominated through surface of the clays instead of the pore network filled by fluid. Moreover, the computed parameters used a brine conductivity of 19.25 mS/cm following the pore fluid extraction results and averaged. Nothing guarantee that such brine is the exact same brine inside the pores of the preserved tested shales. And most of all, we are not sure of the fully saturated condition of these shales despite all the care given for handling them under preservation condition. In conclusion, these results should be used as a guide for very rough estimate of formation factor to apply on electrical logs to compute porosity and water saturation.

Nevertheless, the results seem somehow coherent with expected behavior with low cementation (m) due to a low diagenetic cementation mechanism in shales but very high tortuosity (a) underlined by the complex structures of clay organisations. The formation factor (F) is around 10, excepted for two samples: F and H recording values up to 100 (i.e. one order of magnitude higher). These two very resistive shales correspond to the previously recognised high CBW effect (Figs. 4-9 and 4-10).

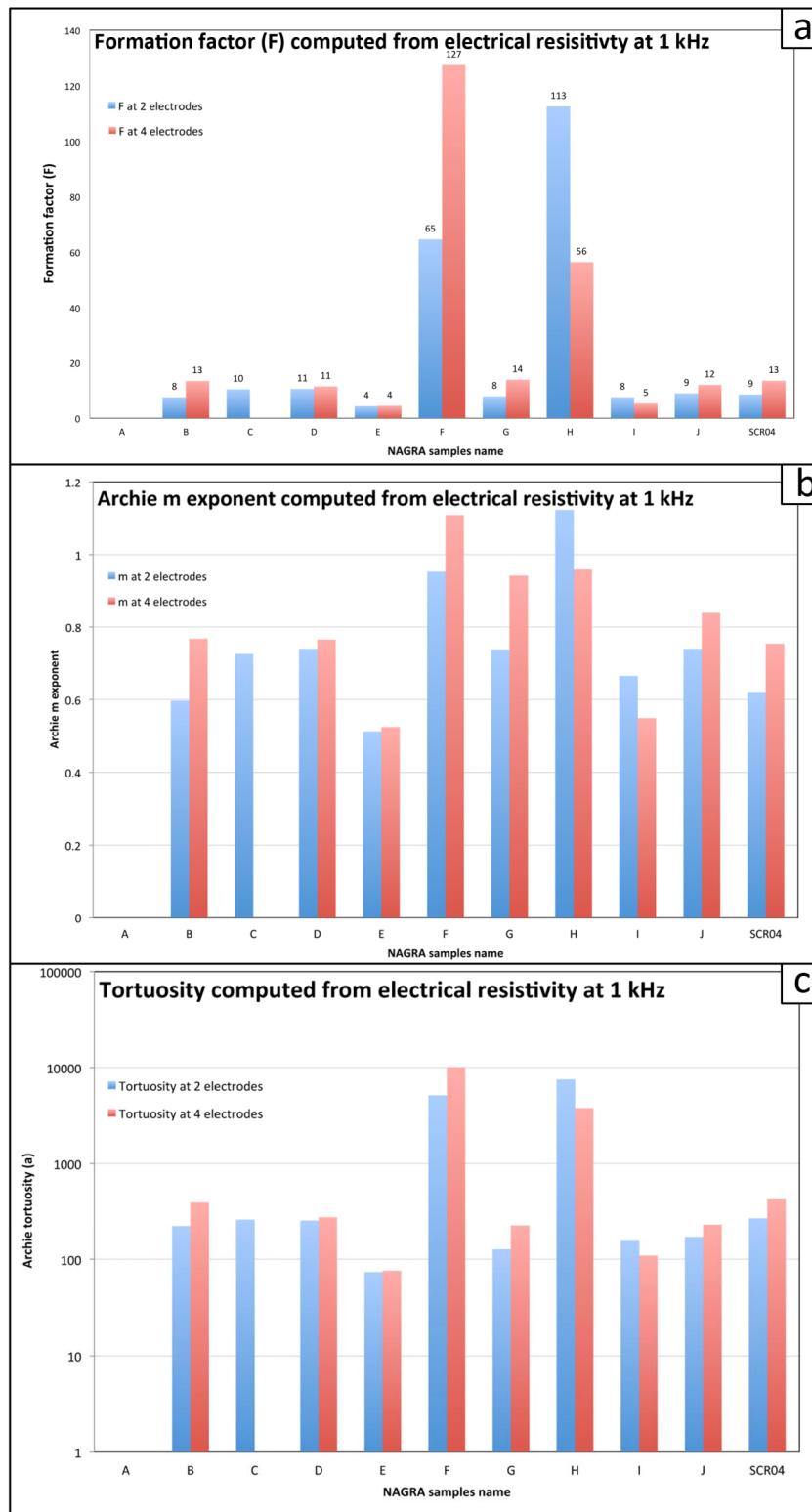


Fig. 4-25: Archie's paramaters computed on the SLA-1 collection plugs from electrical resistivity at 1 kHz under 100 psi confining pressure under brine saturation at 19.25 mS/cm.

When we compare the electrical resistivity from low frequency (and the resistivity derived from conductivity measurements during dielectric tests against the water content from NMR (see Section 4.3), it appears that a power law fit very well the relationship between water and sample resistivity (Fig. 4-26). The samples with the lowest water content record the highest resistivity (NAGRA-F and -H) at 1 kHz. We observe a good fit with a logarithmic curve being similar in 2 and 4 electrodes confirming the validity of the measurements. This aspect also matches the grain density and velocity measurements (see Section 4.6, Table 4-13 and Fig. 4-42) with stiff and well cemented samples corresponding to NAGRA-F and -H.

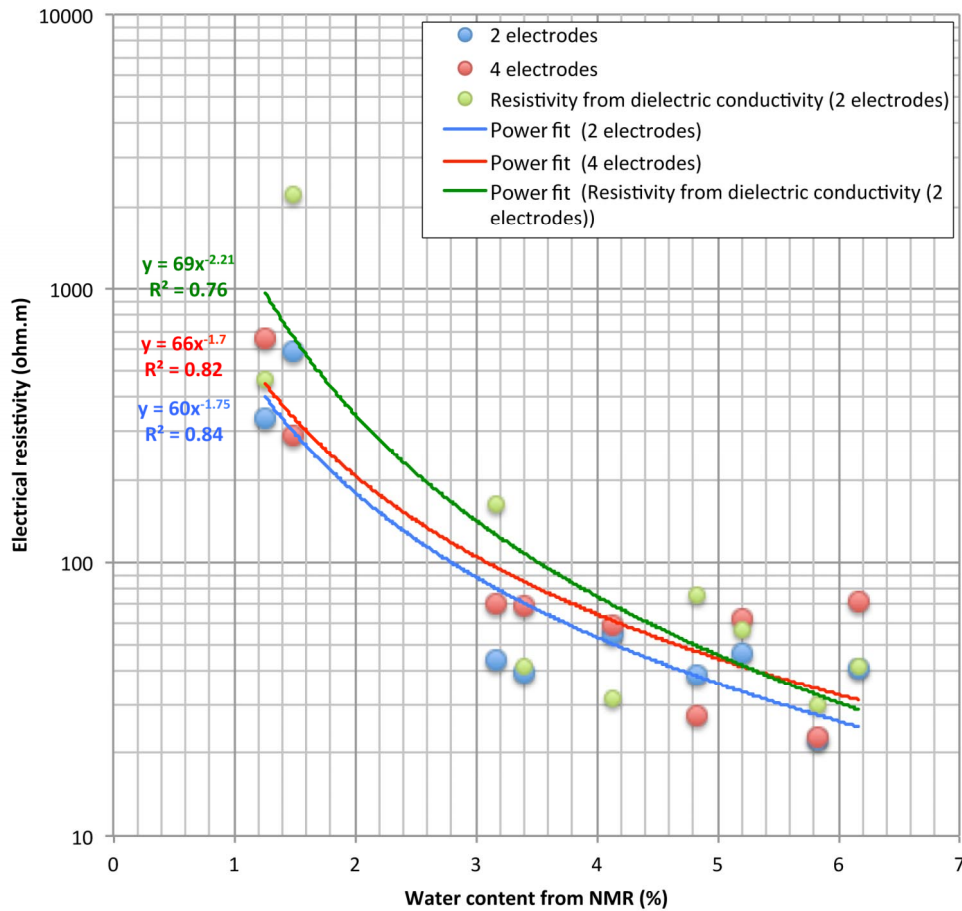


Fig. 4-26: Compilation of all the NAGRA plugs measured for their resistivity at 1 kHz (ohm.m) against the water content from NMR (%).

## 4.5 Electrical properties at high frequency

### 4.5.1 Principle of dielectric measurements

The dielectric constant is a measure of the electrical polarisability of a material (Von Hippel, 1954). When a sample is placed in an electric field, the charge carriers within the sample may flow through the sample (conduction) or undergo temporary displacement or reorientation that results in an induced field within the sample (electrical polarisation). Polarisation processes in single-mineral materials or fluids occur when opposite charge carriers are bound to one another in an atom, a crystalline lattice, or a molecule, meaning that the charged entity does not

experience a net force in an electric field. In such cases, the displacement of the electrical charges is small, fast and completely reversible and the polarization mechanisms operate at high frequency (practically  $> 1$  GHz). The greater the magnitude of the polarization field, the higher the relative permittivity, or dielectric constant of the material.

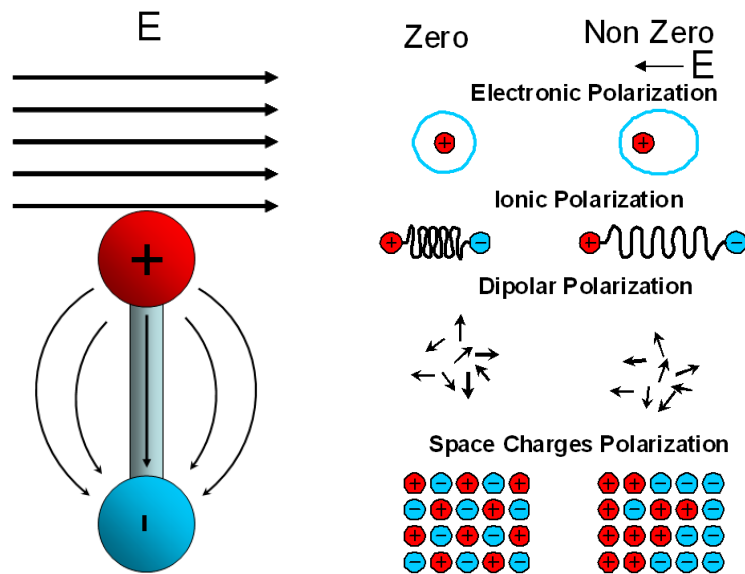


Fig. 4-27: Dipolar molecules can rotate to align with the applied electric field. But other charge polarisation processes exist as well.

In composite materials like rocks, we also see space charge polarization mechanisms wherein ions are only weakly bound to surfaces (most importantly mineral-fluid interfaces) within the sample, and under the electric field these charges slowly migrate away from their equilibrium positions and generate an induced polarization field of increasing size over time. These space-charge processes, being relatively slow, only affect the lower frequency electrical behaviour of rocks such that from 1 GHz down to 1 MHz and below we typically see a large increase in dielectric constant in rocks with appreciable amounts of chargeable surfaces. The ions involved in space charge polarization may be the same as, or may exchange with, those ions involved with conduction. At low enough frequency ( $<$  approx. 10 kHz), space charge polarization is often completely swamped by conduction process.

Dielectric experimentalists are dealing with a number of different polarisation and loss mechanisms. The sum of these processes must be interpreted to resolve the magnitude of each individual polarisation mechanism. In dealing with this problem researchers have developed a number of models to describe the process of polarisation. The simplest of these is the Debye model which isolates one single dielectric polarisation mechanism and treats it as an electric dipole (regardless of true nature of the process). The dipole experiences force and torque resulting from the electric field interacting with the charged components of the dipole, however the dipole has mass and rotational inertia so it must also obey the kinematic equations of motion that require energy to be consumed in driving the dipole. The Debye model specifies a low frequency dielectric polarisation ( $\epsilon'_{r}$  low) where polarisation of the discrete process is unimpeded; a high frequency dielectric polarisation ( $\epsilon'_{r}$  high) which is the sum of processes occurring when the dipole has stopped contributing, and a characteristic time constant ( $\tau$ ) where the transition occurs.

$$\varepsilon^*(\omega) - \varepsilon_\infty = \frac{\varepsilon_s - \varepsilon_\infty}{1 + i\omega\tau} \dots\dots \text{(Debye)} \quad [\text{Eq. 2}]$$

On its own, the Debye model provides a first order fit to much of the dielectric data that is produced from dielectric spectroscopy, however experimentalists have found that the transition generated by the Debye model occurs too quickly to fit experimental data. To overcome this, the Cole-Cole model was developed which adds a smoothing parameter  $\alpha$  to broaden the transition.

$$\varepsilon^*(\omega) - \varepsilon_\infty = \frac{\varepsilon_s - \varepsilon_\infty}{1 + (i\omega\tau)^{1-\alpha}} \dots\dots \text{(Cole - Cole)} \quad [\text{Eq. 3}]$$

In the following example (Fig. 4.28), two dielectric responses have been generated using these two models to demonstrate the effects of the 3-4 parameters. In this example  $\varepsilon_r$  low = 1000,  $\varepsilon_r$  high = 10,  $\tau = 1\mu\text{s}$  and in the case of Cole-Cole  $\alpha = 0.15$ .

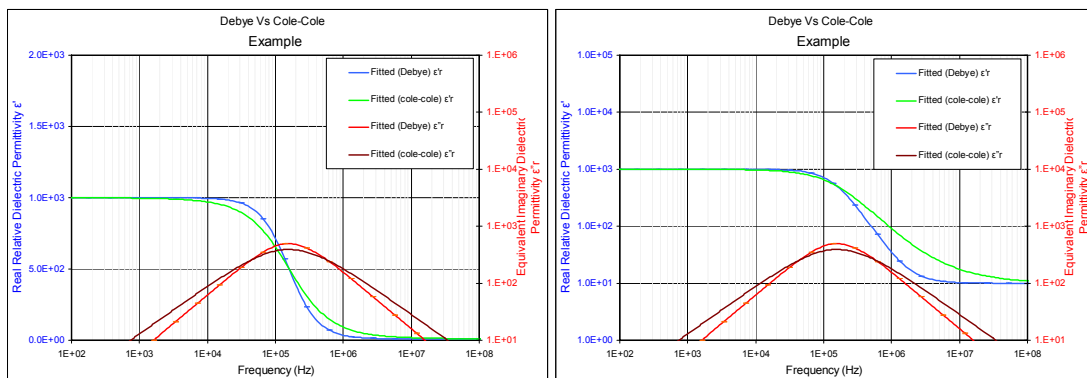


Fig. 4-28: An example of a dielectric response based on the models of Debye and and Cole-Cole.  $\varepsilon_r$  low = 1000,  $\varepsilon_r$  high = 10,  $\tau = 1\mu\text{s}$  and in the case of Cole-Cole  $\alpha = 0.15$ . Both data sets presented are the same but they are plotted on Left) linear magnitude and Right) log magnitude.

It is self evident how the individual parameters effect the generated data and this is probably why Cole-Cole is one the most commonly used models in dielectric spectroscopy. There are however, a number of considerations when using these models. They only include polarisation processes, they do not include conduction. Although it is possible to include a conduction parameter to the fit, we have found that dealing with shales that polarisation processes and conduction processes should be determined using different techniques (ie cling film and brine coupling). The cling film coupled measurement completely removes the possibility of conduction processed so these models are ideal for fitting the cling film coupled data. The dielectric response of a rock sample may have multiple polarisation processes occurring and in the case a Maxwell Wagner polarisation, there is no discrete single sized dipole.

As a petrophysical parameter, dielectric constant has been of interest mainly to quantify water, which is a fixed electrical dipole molecule. In an electric field, the water molecule does not experience a net translational force (i.e. no electrical conduction), but easily rotates to align with the electric field to become polarised. As most solid substances are less easily polarised than

water, moisture content is readily determined from dielectric constant measured at high frequency (e.g. 10 MHz – 1 GHz) and examples can be found in both the petroleum industry and agriculture (Schwank et al., 2006). Petroleum industry dielectric logging (Hizem et al., 2008; Gilmore et al., 1987) was developed on the premise that the dielectric constant of water/oil mixtures is not strongly dependent on salinity and provides a reliable determination of water-filled pore space, and therefore hydrocarbon content, where porosity is independently known. In the laboratory, the complete dielectric vs frequency response is governed by multiple processes that occur within the rock and each process is characterised by the speed at which it occurs (Gueguen and Palciauskas, 1994). In rocks with high surface area like muds and clays it is observed that even at quite high frequencies up to 100's of MHz, there is a significant space-charge polarization effect from the clays overprinting the molecular polarization effect. For instance, while the high frequency dielectric response (above ~1 GHz), is strongly correlated to total water content (i.e. porosity x water saturation), the low frequency dielectric response (below 50 MHz) is more strongly related to the mobile ions which are liberated onto the clay grain surfaces (i.e. the cation exchange capacity or CEC) (Leung and Steiger, 1992). In addition, it is likely that hydration of the clay grain boundaries affects the mechanical connection between the rock grains and therefore the acoustic coupling. We expect that the dielectric response, which correlates very strongly with grain boundary hydration processes (Fig. 4.29), is likely to correlate with acoustic propagation parameters such as the P and S wave velocity and also the geomechanical behaviour of the rock.

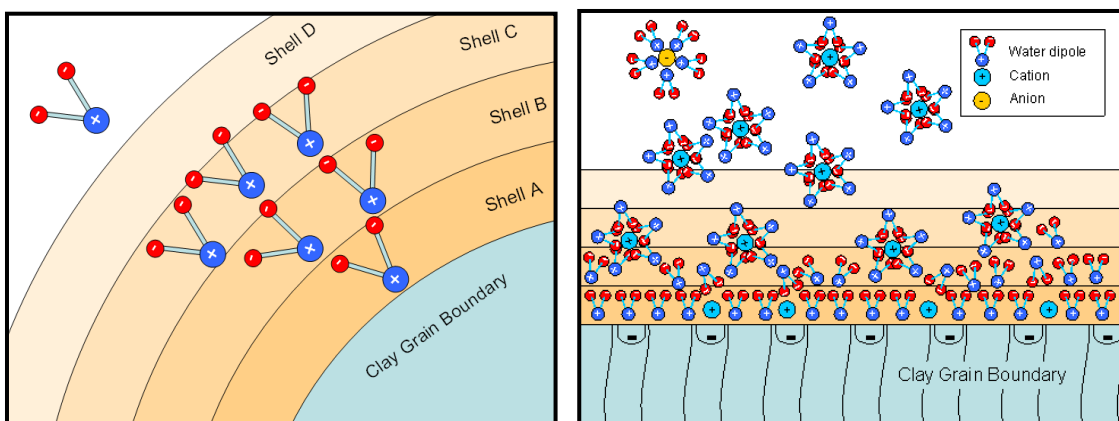


Fig. 4-29: Example model of the hydration of clay grain interfaces as water attaches itself to the exposed charge sites at the outer edge of the clay mineral boundary. Cations and anions in the water can also attach themselves to the clay grain and are able to participate in both conduction and polarisation processes when an electric field is applied.

#### 4.5.2 Experimental methodology and results

**Parallel plate dielectric measurement** (Fig. 4-30; Von Hippel, 1954) is ideal for frequencies from 10 kHz up to 110 MHz. A small quantity of sample material prepared as a thin disc (typically a 5 mm slice of preserved core plug) is placed in the parallel plate measurement cell, prior to measurement with an Agilent impedance analyser (4294A). The sample is simply removed from preserving oil, ground to remove the outer layer of oil contaminated rock. There are two methods for running this instrument depending on the data that is required.



Fig. 4-30: Parallel plate dielectric measurement cell. The instrument consists of a three terminal capacitor for which parallel faced disc samples are prepared. The cell can be placed in a load cell to insure good coupling between the sample and the electrodes.

1) Cling film coupling. The real and imaginary components of dielectric permittivity are best determined by placing a current blocking film (cling film food covering, trade name Glad wrap) between the sample and the electrodes to eliminate current flow but enhance polarisation effects. This data is suitable for determining the Cole-Cole parameters.

2) Brine Coupling. Conductivity is best determined by allowing the sample to soak for a brief period of time in weak brine (~10% seawater strength 3.5 g/l NaCl), however with many shale samples, this tends to break them, so we only allow the sample to soak in brine for 5 seconds. This provides the high frequency conductivity which is often useful to correlate with the low frequency 4-terminal measurement which are more commonly recognised in petrophysics.

In Tables 4-10 and 4-11, the real and imaginary dielectric permittivity and the conductivity are tabulated for the parallel plate measurements on the Nagra collection. The results include both the brine coupled and the glad coupled measurements. The complete frequency sweep data is also presented (Fig. 4-31).

Tab. 4-10: Dielectric analysis of the SLA-1 samples including the real dielectric permittivity, the equivalent imaginary dielectric permittivity and the equivalent conductivity for all the preserved samples. Measurements were made using the parallel plate dielectric cell and cling film coupling.

Cling Film Coupled									
	$\epsilon'_{r@1MHz}$	$\epsilon'_{r@10MHz}$	$\epsilon'_{r@100MHz}$	$\epsilon''_{r@1MHz}$	$\epsilon''_{r@10MHz}$	$\epsilon''_{r@100MHz}$	$\sigma@1MHz$	$\sigma@10MHz$	$\sigma@100MHz$
NagraA	208.95	42.88	16.53	112.05	51.87	11.05	0.0064	0.0296	0.0627
NagraB	222.49	36.38	14.59	155.90	52.63	10.85	0.0089	0.0300	0.0616
NagraC	229.55	35.94	15.36	195.91	51.69	10.15	0.0112	0.0295	0.0576
NagraD	233.57	45.05	16.44	108.68	60.32	12.85	0.0062	0.0344	0.0730
NagraE	288.63	42.28	16.74	187.34	64.99	12.13	0.0107	0.0371	0.0689
NagraF	37.81	15.05	9.90	36.13	9.29	2.54	0.0021	0.0053	0.0144
NagraG	209.72	34.10	15.10	142.53	46.65	9.10	0.0082	0.0266	0.0517
NagraH	37.35	18.18	12.07	26.04	8.61	3.10	0.0015	0.0049	0.0176
NagraI	113.38	32.10	13.90	45.27	29.65	7.20	0.0026	0.0169	0.0409
NagraJ	166.89	29.51	13.70	183.99	41.91	8.77	0.0105	0.0239	0.0498
NagraSCR2	138.88	28.62	13.25	142.88	33.81	8.10	0.0082	0.0193	0.0460
NagraSCR3	43.03	14.87	8.59	26.17	9.78	2.96	0.0015	0.0056	0.0168
NagraSCR4	88.48	23.32	11.33	65.84	21.16	5.90	0.0038	0.0121	0.0335
NagraSCR5	112.62	25.43	12.28	160.28	31.49	7.37	0.0092	0.0180	0.0419

Tab. 4-11: Dielectric analysis of the Nagra samples including the real dielectric permittivity, the equivalent imaginary dielectric permittivity and the equivalent conductivity for all the preserved samples. Measurements were made using the parallel plate dielectric cell and brine coupling.

Brine Coupled									
	$\epsilon'_{r@1MHz}$	$\epsilon'_{r@10MHz}$	$\epsilon'_{r@100MHz}$	$\epsilon''_{r@1MHz}$	$\epsilon''_{r@10MHz}$	$\epsilon''_{r@100MHz}$	$\sigma@1MHz$	$\sigma@10MHz$	$\sigma@100MHz$
NagraA	84.18	34.85	16.54	486.25	66.19	13.15	0.0279	0.0378	0.0747
NagraB	64.85	29.78	15.05	495.11	62.12	10.76	0.0284	0.0354	0.0611
NagraC	68.66	30.95	15.42	497.13	63.30	12.11	0.0285	0.0361	0.0688
NagraD	72.75	34.10	17.08	644.14	78.38	13.36	0.0369	0.0447	0.0759
NagraE	71.15	33.29	16.74	658.51	80.04	14.37	0.0377	0.0457	0.0816
NagraF	31.19	15.58	10.36	55.99	10.56	2.20	0.0032	0.0060	0.0125
NagraG	60.07	29.72	15.66	477.67	59.53	11.52	0.0274	0.0340	0.0654
NagraH	40.59	19.74	12.72	40.42	10.48	2.98	0.0023	0.0060	0.0169
NagraI	54.08	28.29	14.11	272.52	38.73	8.86	0.0156	0.0221	0.0503
NagraJ	43.01	28.74	14.62	361.34	48.39	9.35	0.0207	0.0276	0.0531
NagraSCR2	65.90	27.41	13.68	278.58	40.17	8.92	0.0160	0.0229	0.0507
NagraSCR3	32.08	15.97	9.41	86.27	14.49	3.24	0.0049	0.0083	0.0184
NagraSCR4	47.95	21.09	11.30	153.70	24.65	6.07	0.0088	0.0141	0.0345
NagraSCR5	56.45	25.05	12.68	232.66	34.50	7.18	0.0133	0.0197	0.0408

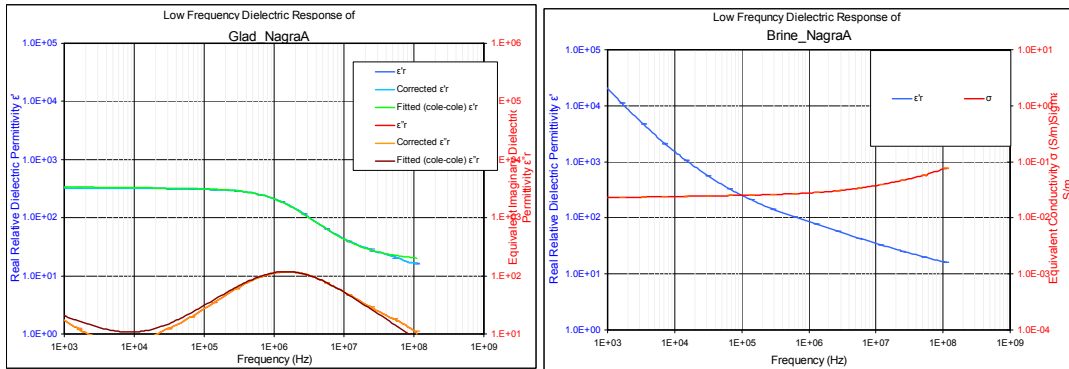


Fig. 4-31: Example measurements for Nagra sample A. Top) Real and equivalent imaginary dielectric permittivity responses determined using cling film coupling with Cole-Cole fitting. Bottom) Real dielectric permittivity and conductivity determined using brine coupling (3.5 g/l NaCl). Using cling film coupling we observe a plateau in real dielectric permittivity below 100 KHz of approximately  $\epsilon''_r = 300$  which transitions rapidly to a lower value from 100 KHz to 100 MHz. There is a corresponding peak in the dielectric loss (the imaginary component) associated with this transition. The brine coupled real dielectric permittivity is decreasing with increasing frequency; however the conductivity we observe with the brine coupled measurement is generally very flat across the frequency range ( $\sigma = 0.02$  S/m), but increases slightly above 1 MHz, as a result of additional dipolar loss mechanisms adding to the conduction loss.

Typically we observe that brine-coupled measurements and cling film coupled measurements converge to similar permittivity values at high frequency where electrode polarisation effects are less pronounced. At low frequencies ( $\sim 1$  MHz or less), electrode coupling strongly influences the apparent dielectric response and we use cling film to decouple the DC current through the electrodes into the sample and allow a more correct evaluation of dielectric permittivity. Furthermore, the brine coupled measurement combines conduction loss and dipole loss into a single equivalent conduction (or  $\epsilon''_r$ ) term. Cling film, however, blocks the DC current and only the dipole loss mechanism can contribute to the equivalent conduction (and  $\epsilon''_r$ ). The results presented in Fig. 4-32 demonstrate that all measurements procedures are equally valid at 10 MHz and 100 MHz. At 1 MHz, where electrode coupling affects dielectric permittivity measurement and where DC conduction is removed from the total charge transport, we observe that correlation breaks down significantly.

The dielectric and conductivity data for the complete set of Nagra samples is presented in Fig. 4-33 a-c. We observe that the real dielectric permittivity @ 10 KHz ranges from  $\sim 80$  to  $\sim 600$ , which is relatively high for geological samples, but consistent with shales. We observe some differences between the samples with clearly low brine coupled conductivity ( $< 0.01$  S/m) in NAGRA-SCR04, -SCR03, -F and H when soaked in brine. The remaining samples have conductivity of around 0.02 S/m. Samples, NAGRA-SCR04, -SCR03, -F and H, also show typical cling-film coupled dielectric permittivity of approximately 100 @ 10 KHz compared to the remaining samples which show a typical dielectric permittivity of approximately 600 @ 10 KHz. Samples, NAGRA-SCR04, -SCR03, -F and H also showed the highest resistivity during 4-terminal measurement (Section 4.1 and 4.2), and additional testing indicated that they had lowest water contents.

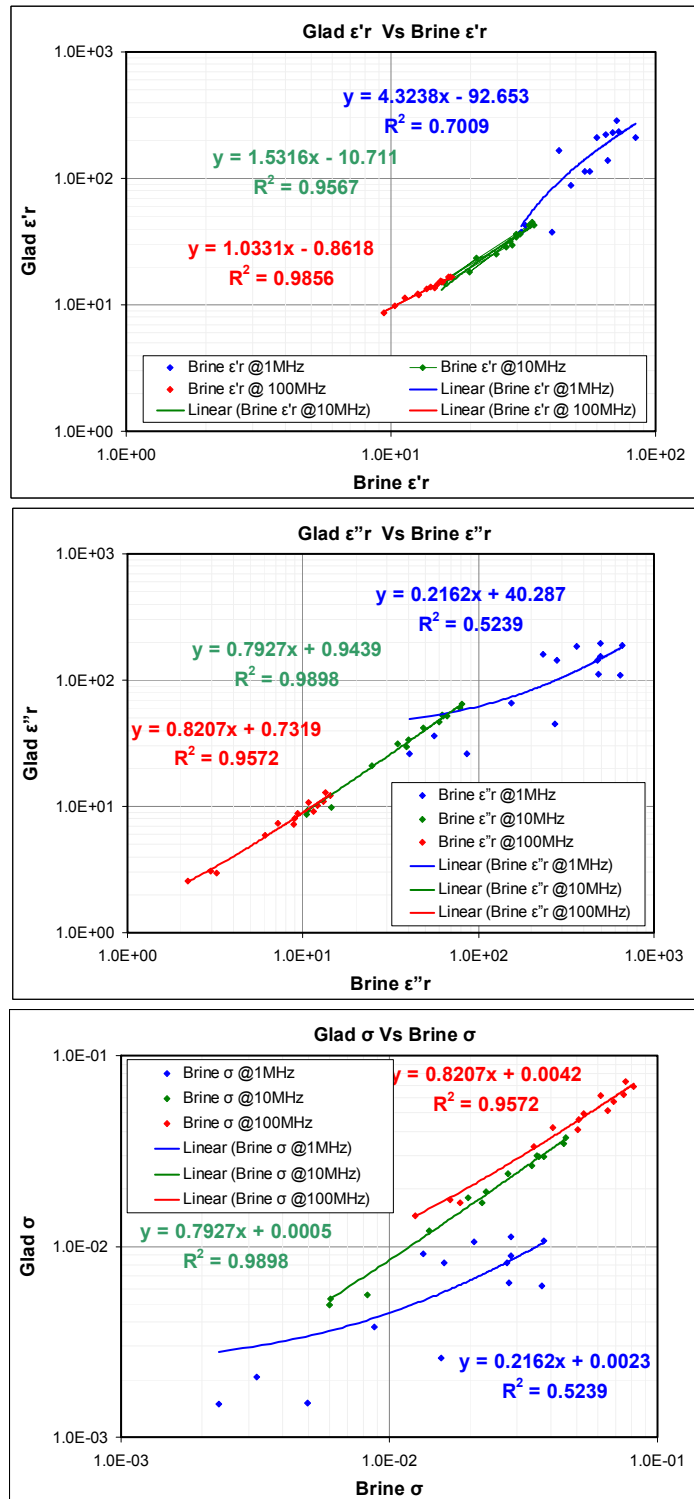


Fig. 4-32: Comparison of the cling film versus brine treatment measurement procedures for the dielectric parameters  $\epsilon''r$  (real dielectric permittivity),  $\epsilon''r$  (equivalent imaginary dielectric permittivity) and  $\sigma$  (equivalent conductivity). Generally the cling film (Glad) and Brine coupled measurements correlate with one another, however the transition from 1 MHz up to 10 MHz improves the correlation from typically  $\sim 0.6$  up to better than 0.95, which is retained at 1GHz.

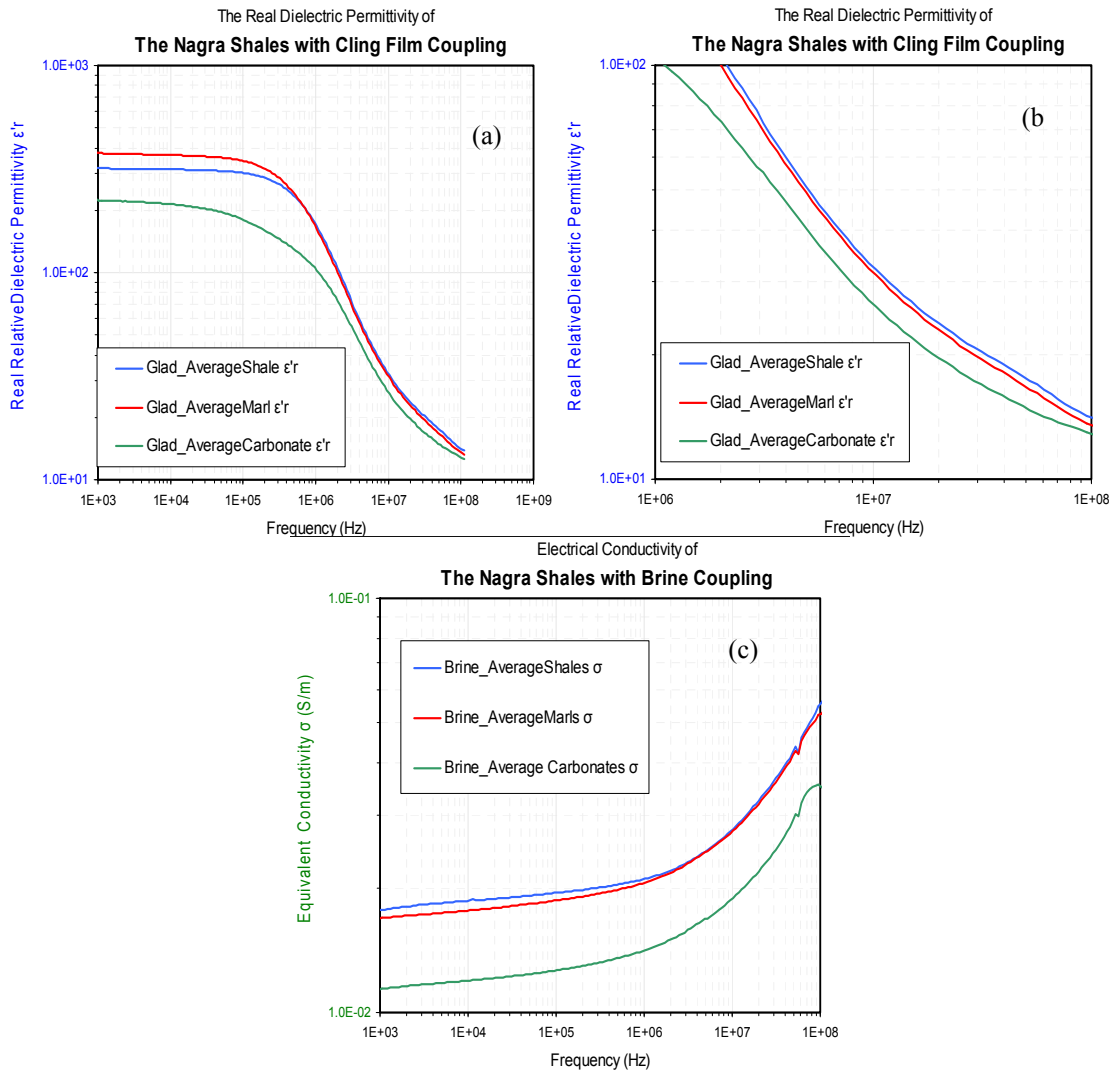


Fig. 4-33: The real dielectric permittivity determined for the averaged “Carbonates” “Shales” and “Marls” from the Nagra Samples. (a) The broad frequency sweep and (b) the 1 MHz to 100 MHz frequency sweep. Below 1 MHz, marls have the highest dielectric permittivity closely followed by the shales and the carbonates are much lower. Above 1 MHz the shales have the highest dielectric permittivity, closely followed by the marls but the carbonates have much lower dielectric permittivity. (c) The conductivity determined for the average “Carbonates” “Shales” and “Marls” from the Nagra Samples. Brine is used to improve DC coupling through the sample. Across the entire frequency range shales have the highest conductivity closely followed by the marls but the carbonates have a much lower conductivity.

We expect the dielectric permittivity and conductivity to reflect the clay content of the rocks and the results presented in Fig. 4-33a-c indicate that we are able to confirm the XRD categorized rock types. In later discussion, the dielectric results will be cross correlated against the XRD determined quantities.

**16mm Coaxial transmission line dielectric measurement** (Fig. 4-34) is ideal the purpose of measuring drill cuttings and small quantities of powdered samples [Nicholson and Ross, 1970; Weir, 1974; Baker-Jarvis Vanzura and Kissick 1990]. The cell can also be used for rock cores 40 mm long, 16mm diameter with a 7mm hole (drilled) coaxially through the centre [Josh et al, 2007]. The cell is connected to an Agilent E5070B network analyzer to measure the reflection and transmission scattering (S) parameters from 300 KHz to 3GHz. With lossy samples typically provided by the petroleum industry, the cell is easily capable of measuring the entire frequency range.

A subset of four of the Nagra samples (NAGRA- I, -H, -G and -SCR04) were prepared as dry powder samples and measured using the 16mm coaxial transmission line to compare with the parallel plate measurements previously discussed. The powdered samples are also ideal for Specific surface area testing, and as such an identical sample is provided for both testing procedures.



Fig. 4-34: CSIRO 16 mm coaxial transmission line cell. Small coaxial samples of solid rocks are specially prepared for the cell, but more typically the cell is used for analysing drill cuttings which are packed into the coaxial volume after being prepared as a fine powder or a paste.

A small number of the samples were tested using the 16mm coaxial cell on powdered versions of the samples and these data are summarized in Table 4-12.

Tab. 4-12: Data from electrical high frequency on a selection of the NAGRA collection: real dielectric permittivity, equivalent imaginary dielectric permittivity and equivalent electrical conductivity from discs preserved in glad film and in brine and from powders (specific collection: NAGRA-G, -H, -I and -SCR04).

16mm Coaxial on Dry Powder												
	$\epsilon'_{r@1MHz}$	$\epsilon'_{r@10MHz}$	$\epsilon'_{r@100MHz}$	$\epsilon'_{r@1GHz}$	$\epsilon''_{r@1MHz}$	$\epsilon''_{r@10MHz}$	$\epsilon''_{r@100MHz}$	$\epsilon''_{r@1GHz}$	$\sigma_{@1MHz}$	$\sigma_{@10MHz}$	$\sigma_{@100MHz}$	$\sigma_{@1GHz}$
NagraG	48.78	21.21	9.79	5.24	169.54	25.90	7.22	0.37	0.0093	0.0151	0.0394	0.0215
NagraH	9.85	7.34	5.89	3.40	3.01	1.52	0.95	1.20	0.0002	0.0009	0.0052	0.0701
NagraI	48.33	20.84	9.55	4.98	151.86	24.16	6.96	0.35	0.0083	0.0141	0.0380	0.0203
NagraSCR4	16.98	9.59	5.75	3.11	9.92	4.10	2.09	0.43	0.0005	0.0024	0.0114	0.0252

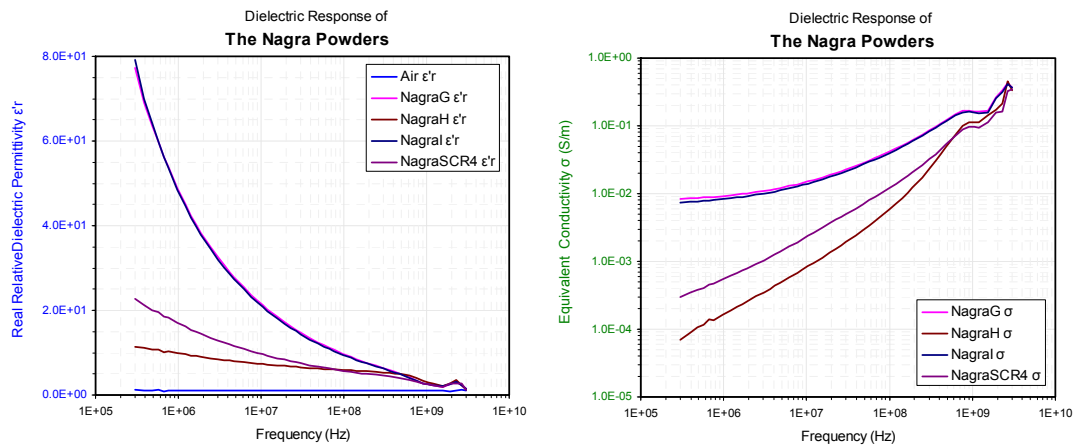


Fig. 4-35: Dielectric and conductivity measurements of the samples NAGRA-G, H, I and SCR04. The samples were prepared as powders and then tested using the 16 mm coaxial transmission line cell. The dielectric response reduces almost perfectly linearly with an increase in frequency. Samples G and I are particularly similar and they are also generally categorized as “shales according to their XRD response. Nagra H is categorized as a carbonate according to XRD data and it has the lowest dielectric response of all the samples tested. The conductivity generally increases with increasing frequency which indicates that polarisation loss  $\epsilon''_r$  is significant.

The dielectric response determined using the 16 mm coaxial transmission line with the powdered sample compares quite well with both the glad coupled and brine coupled parallel plate measurements which are provided in Figures 4-32 and 4-33. We expect all 3 to converge as the frequency is increased, because electrode polarisation occurring with the brine coupled parallel plate sample is becoming less significant. At 100 MHz ( $1e+08$ ), the measurements all converge to a dielectric permittivity of approximately  $\epsilon'_{r} = 6 - 10$ . Likewise the conductivity of the brine coupled parallel plate measurement on disc sample agrees well with the 16 mm coaxial transmission line measurement.

**Endloaded coaxial transmission line dielectric measurement (Fig. 4.36)** is based on an inversion algorithm for the scattering parameters measured for a section of coaxial transmission line terminated against the surface of the sample. Probes of this nature are described by Burdette, Cain and Seals (1980) and Stuchly and Stuchly (1980), and Agilent have their own commercially available instrument (85070E). While not particularly accurate and with limited bandwidth, the end-loaded probe is a rapid measurement system, which makes it perfect for large batches of drill cuttings (cf. Leung and Steiger, 1992).



Fig. 4-36: Photograph of the end-loaded transmission line probe.

The powdered samples that were used for the 16 mm coaxial transmission line dielectric measurement were prepared as pastes using a procedure developed at CSIRO. The powders are mixed with a known quantity of water then centrifuged and the excess water canted off to leave behind a thick paste. This method forces the sample to retain a small content of water which is later determined using drying and weighing. The paste is then pressed against the open end of the coaxial transmission line and the dielectric response can be measured (Fig. 4-37).

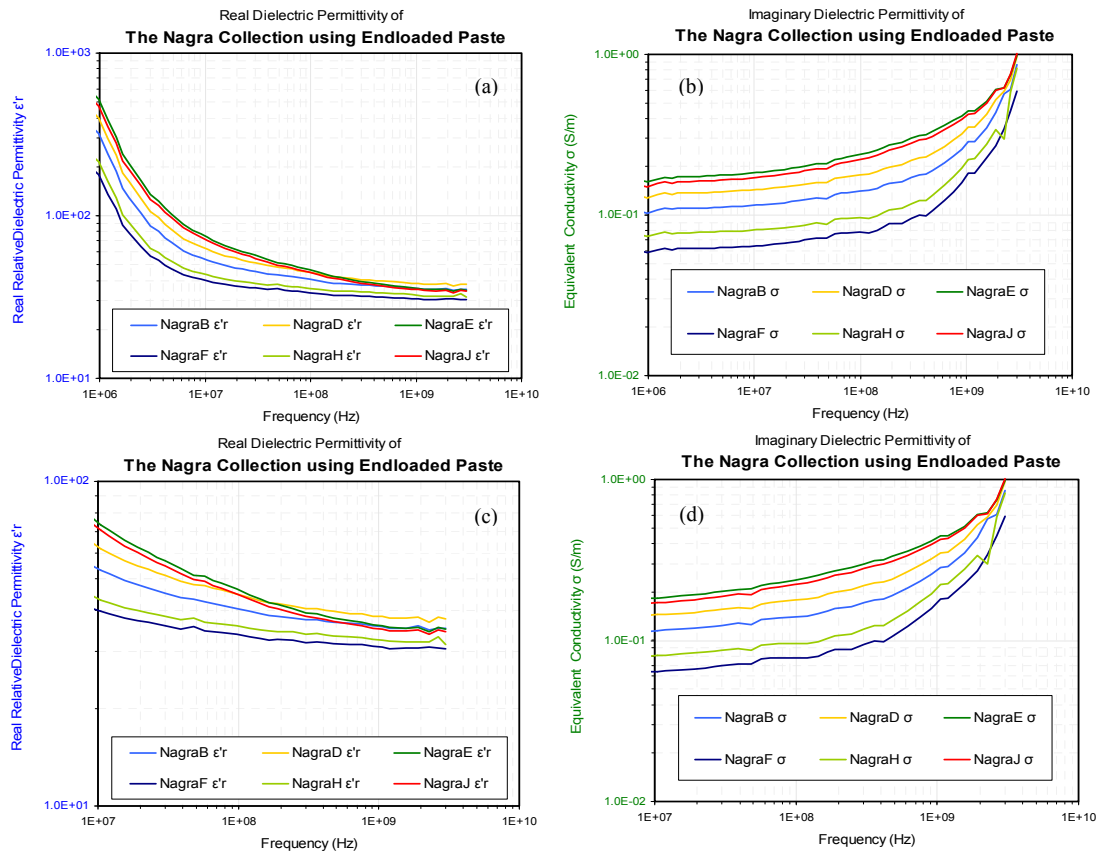


Fig. 4-37: The (a) dielectric and (b) conductivity measurements of a subset of the Nagra samples with the complete frequency range.

The samples were prepared as pastes and then tested using the endloaded coaxial transmission line. The dielectric response of the samples is decreasing with frequency to a plateau value of approximately 30-40 at 1 GHz, which is much greater than the dry powder response but is expected because of the increased water content resulting from preparation. The conductivity is quite flat across the frequency range up to around 300MHz after which polarisation loss dominates the measurement. The (c) dielectric and (d) conductivity measurements of a subset of the Nagra samples as per Fig. 4-37a, with a zoomed in frequency range.

The real dielectric permittivity reduces rapidly with an increase in frequency which is typical of wet shale samples and is attributable to the mobility of water molecules and ions in the rock fabric. The mobility of the polarisable charge carriers is likely to reduce as the frequency is increased and consequently the real dielectric permittivity decreases. The conductivity of the samples is typically quite flat across the frequency range up to ~ 100 MHz but 100 MHz we observe a mild increase in equivalent conductivity which becomes strongly apparent above 1 GHz. This is consistent with two different loss mechanisms coexisting in the sample. Firstly, simple conduction resulting from the flow of monopole charge carriers through the sample. This has a characteristically flat response across the frequency range. Secondly, dipole loss resulting from work required to polarise the water molecules. This has a characteristic increase with frequency but is often lower in magnitude than the conduction loss. The two sum together in the equivalent conductivity to form a flat response up to 100 MHz beyond which the dipole loss processes dominate. Overall the dielectric and conductivity responses of the Nagra samples as determined using the endloaded coaxial transmission line are higher than for the other measurement techniques (Fig. 4-37 a-d). This is simply related to the additional water content of

these samples resulting from the paste preparation technique that is used. The following figure provides an example of the preserved and non-preserved measurement techniques.

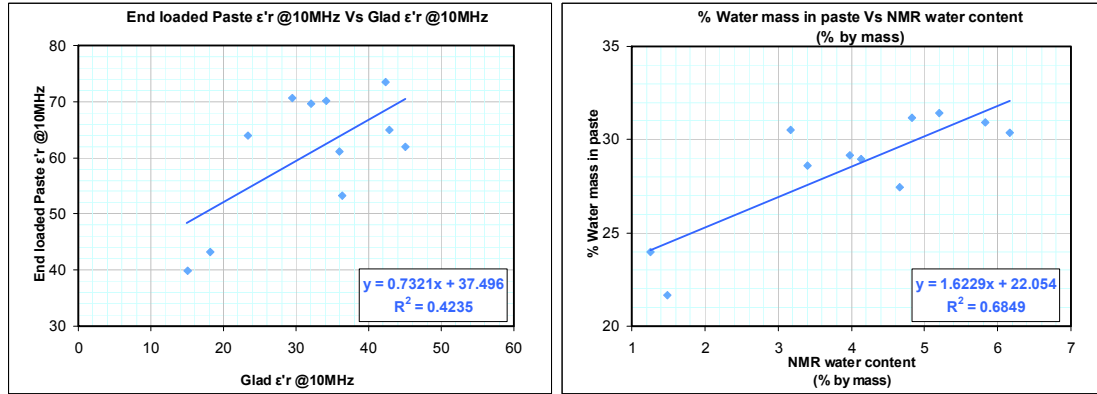


Fig. 4-38: Comparison of real dielectric permittivity at 10 MHz measured using endloaded transmission line measurement on paste prepared from the preserved sample against a cling film coupled measurement on the preserved sample (left).

Generally we see that the endloaded paste measurement is higher than its equivalent glad coupled parallel plate measurement on a preserved sample, but this is consistent with the additional water present in paste sample. The correlation is not particularly strong. (right) Comparison of the water content in the paste sample with the water content in the original preserved sample determined using NMR. We also observe that the water content of the paste (typically 20 – 35 % by mass) exceeds the water content of the preserved sample (typically 1 - 7 % by mass).

The grinding process which is used to prepare the powder and paste samples completely destroys the micro structure above approximately 20 μm. During paste preparation, the content of water added is significantly greater than would occur in a preserved rock sample. Furthermore, the moisture contained within the paste is certain to be more well connected than in a preserved sample. At 10 MHz (Fig. 4-38 left), the dielectric processes which are associated with cation exchange are still able to occur. It is therefore probable that the cations exchanged into the water within the paste sample are more free to move in larger droplets and this leads to an increase in the dielectric response when compared to the preserved sample. The correlation observed ( $R^2 = 0.4235$ ) is weak. It is likely that the different minerals from which each of the Nagra samples is composed (and there is a large variation in dominant mineralogy) has a different affinity for water. Hydration during paste preparation is not necessarily related to the initial preserved sample water content (Fig. 4-38 right) and we observe that the correlation between preserved sample water content and paste water content ( $R^2 = 0.6849$ ) do not strongly correlate either. This would suggest the dielectric permittivity measured for cling film coupled preserved sample could be used to determine the paste measurement. If for instance the water component of the sample facilitates CEC processes that cause increases in the dielectric response, then it would be proper to assume that:

$$\epsilon'_{r(paste @ 10 MHz)} = A * (\epsilon'_{r(glad @ 10 MHz)} + B * CEC * (\% Water in Paste - \% Water in Preserved)) + C \quad [Eq. 4]$$

In other words the paste measurement equals the dielectric response of the preserved sample plus a constant (B) multiplied by the propensity for cations to transfer into the additional water that is added to the preserved sample to achieve a paste (Fig. 4-39).

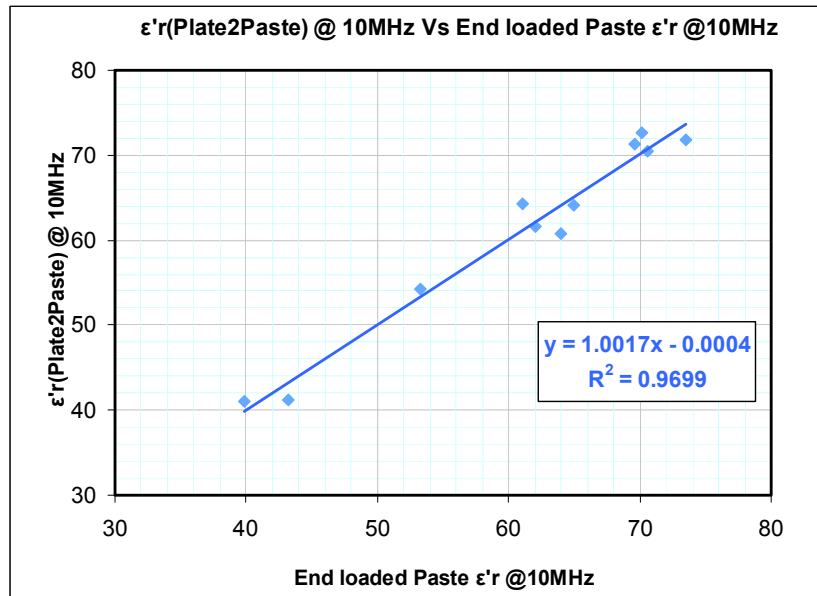


Fig. 4-39: This is an attempt at converting a preserved measurement into a paste measurement. The initial preserved sample dielectric response is increased by an amount calculated from the increase in moisture and CEC. The results demonstrate a very strong 1-to-1 correlation can be achieved and therefore we can substitute the ease of a paste style measurement for the quality of a preserved style measurement.

Although our initial paste measurements versus preserved measurements (Fig. 4-38 Left) could not identify a clear relationship, it is actually simply explained by the increase in moisture occurring in the sample when it is converted into a paste and the CEC which ultimately liberates ions into that additional water. The tweaking parameters to achieve a 1-to-1 relationship are  $A = 0.284$  and  $C = 31.386$ , the correlation is optimised when the mixing factor  $B = 0.25$ . Surprisingly, this leads to a correlation of nearly 97% which is a huge improvement on the original 42% correlation achieved without the use of a CEC based rock fabric correction. Furthermore, it is consistent with the simplest of rock fabric models. Ideally, it is desirable to deliver petrophysic measurements on preserved samples where both the rock constituents and the rock fabric (or assembly of mineralogy) is consistent with the in-situ nature of the rock. However, the availability of good quality preserved rock depends on extensive coring and preservation procedures which are expensive and rarely completed. Consequently, companies are often reluctant to make this material available. The paste preparation measurement typically requires 20 g of rock fragments (large and uncontaminated by drilling mud), but this is typically much easier to acquire than preserved core. Pastes are also typically easier and faster to prepare and measure and we have found that paste measurement is quite repeatable. By establishing a strong correlation from powder based measurements to preserved measurements, we can deliver much better quality data from cheaper and more readily available cuttings samples. It is also a critical step in determining formation dielectric response from drill cutting samples, which are also much more readily available than core.

### 4.6 Ultrasonic wave velocities

Ultrasonic P- and S-waves were propagated along the cylindrical plug axis within the electro-acoustic cell. The samples were saturated with synthetic pore water and subjected to a slight radial stress (100psi / 0.69 MPa) to improve the coupling of the ultrasonic transducers to the rock sample end faces and therefore increase the signal-to-noise ratio of the recorded waveforms. Examples of ultrasonic waveforms are given for a P-wave (Fig. 4.40) and for an S-wave (Fig. 4.41) on the plug NAGRA-B. The arrival time of the P- and S-phases are picked and used to calculate the P- and S-wave velocities, respectively, knowing the length of the specimen. Table 4-13 summarizes all the wave velocity data. The uncertainty in the determination of the P-wave velocity is ~10%; that of the S-wave velocity is ~20%.

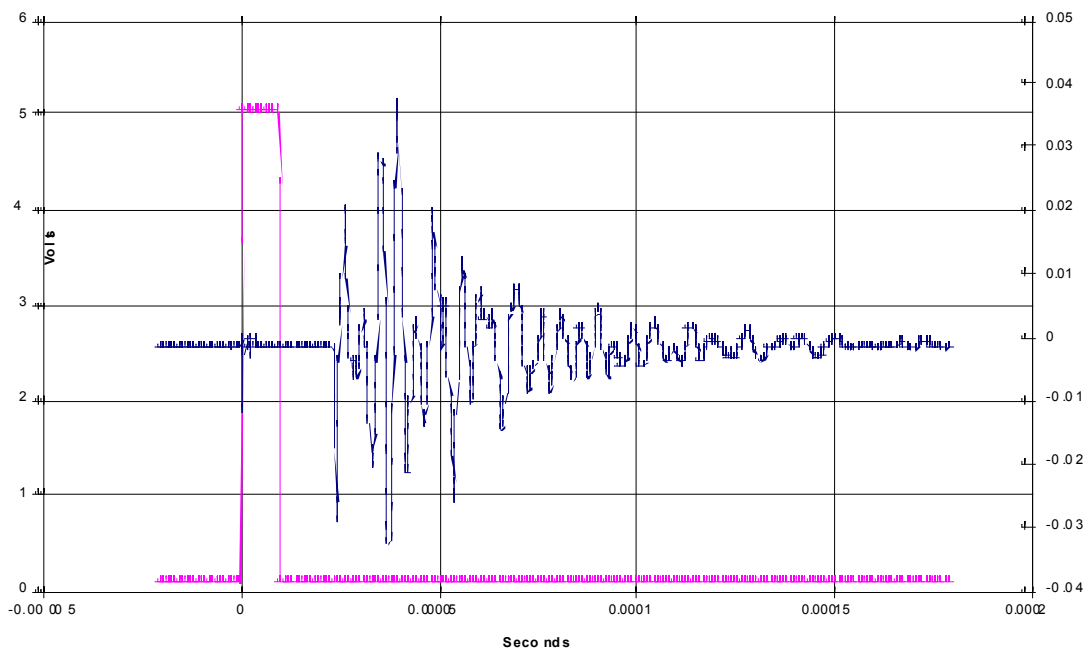


Fig. 4-40: Typical ultrasonic signal transmitted between two P-wave transducers through a cylindrical rock plug in the axial direction (plug extracted from the core NAGRA-B). The pink line corresponds to the trigger signal.

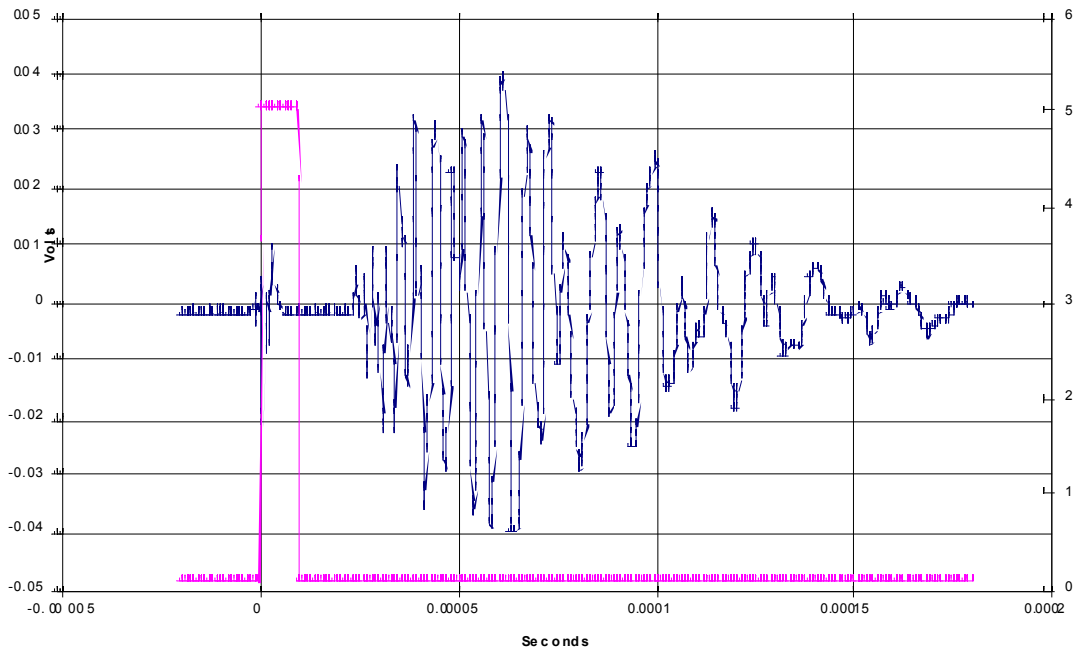


Fig. 4-41: Typical ultrasonic signal transmitted between two S-wave transducers through a cylindrical rock plug in the axial di. rection (plug extracted from the core NAGRA-B). The pink line corresponds to the trigger signal.

Tab. 4-13: Summary table of P- and S-wave velocities obtained on plugs extracted from cores A to J and from SCR04.

Sam-ple #	Strati-graphy	Depth (m bg)	Length (mm)	P flight time (us)	S flight time (us)	Vp (m/s)	Vs (m/s)	Vp / Vs	Radial Stress (psi)
A	Varians	761.85	57.35	28.6	43.6	2793.5	1864.4	1.50	0
B	Varians	766.15	57.5	23.3	39.4	3775.4	2164.9	1.74	100*
C	Parkinisoni	772.76	57.5	26.7	48.5	3086.4	1612.5	1.91	100*
D	Parkinisoni	773.6	57.4	24.5	40.8	3493.6	2052.9	1.70	100*
E	Wedel-sandsein	812.59	57.5	27.9	41.4	2899.6	2013.3	1.44	100*
F	Wedel-sandsein	826.72	57.5	19.4	31.3	5075.0	3114.8	1.63	100*
G	Opalinus	853.62	51.7	32	50.4	2160.5	1376.5	1.57	100*
H	Opalinus	886.6	57.17	18.5	33.1	5481.3	2821.8	1.94	100*
I	Opalinus	929.8	50.4	32.1	N/A	2097.4	N/A	N/A	100*
J	Opalinus	946.08	43	25.2	41.8	2510.2	1484.8	1.69	100*
SCR04	Opalinus	856.09	56.5	31.6	N/A	2401.2	N/A	N/A	100*

\* 100psi correspond to 0.69 MPa.

Table 4-13 summarises the most relevant petrophysics and rock physics parameters. A good correlation between velocities-grain densities and water content from NMR (Fig. 4.42) is also well sorted and contributes to explain the good cross-correlations between the water content-cementation effects on all the rock physics parameters. Note that the water content can be equivalent to the total porosity of the samples. The good cross-correlations seem to be governed by the lithological y/mineralogy in that they express the strong dependency of the aforementioned rock properties on carbonate content.

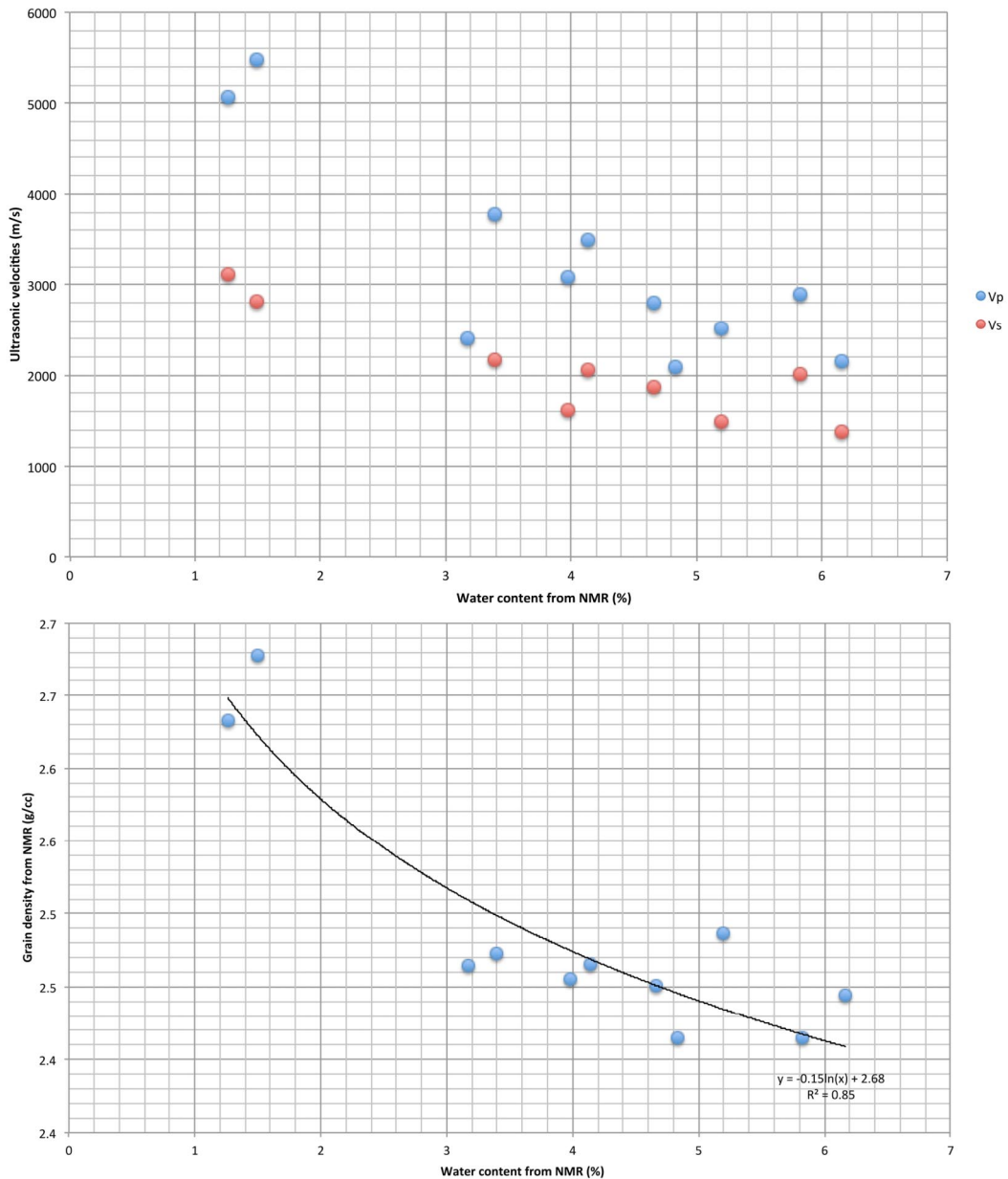


Fig. 4-42: Relationship between water content averaged from the three NMR methods (% from the Table 4-1) and the velocities (Vp-Vs) as well as grain density derived from NMR water content on all the NAGRA collection.



## 5 Summary and discussion

### 5.1 Empirical correlations of physical properties

#### 5.1.1 Dielectrics and P-waves ultrasonic velocities

Seismic imaging is the principal geophysical technique used by the petroleum industry for oil exploration and to determine reservoir extent and capacity. This leads to a natural requirement for information about rock acoustic properties. Laboratory testing of rock provides the principal data against which to compare acoustic borehole logging tools. It provides useful data for interpreting seismic image logs and may also be related to the degree of fracturing occurring in the rock and also to the nature of the pore fluids. This type of rock testing is often conducted using a triaxial load cell, completed with ultrasonic measurement and control over the confining pressure and pore fluid pressure. Unfortunately this type of measurement is particularly time consuming when testing shales because of the time required to equilibrate the fluid throughout the sample when transitioning the pore or confining pressure. Based on our simple textural model (Fig. 4-16) we have reason to believe that the dielectric response of a shale may be linked to the rigidity of the connection between rock grains and may also extend to predicting rock acoustic properties. Dielectric analysis however is fast and often requires only 10grams of non-preserved sample. If we can establish a relationship between the dielectric response and the ultrasonic velocities we may be able to provide industry with a significant quantity of valuable information as a substitute to elastic wave analysis at a much lower cost.

Dampening of the acoustic properties is associated with a reduction in P-wave velocity ( $V_p$ ), and an increase in deformability/compliance of the rock as a whole, including the effects of the various minerals composing the rock, the pore space/cracks/grain contacts and the pore fluid. Therefore, deformability is related to moisture content and SSA and this what causes the correlation between the dielectric response and  $V_p$  (Figs. 5-1 and 5-2). The relationship is strong for both real (Fig. 5-2) and equivalent imaginary (Fig. 5-1) dielectric permittivity. However in the case of real permittivity, the relationship gets weaker as the frequency is increased above 100 MHz. The equivalent imaginary dielectric permittivity at all frequencies correlates (maybe slightly improving with frequency) very well with  $V_p$ . Unexpectedly, this correlation exists between electrical properties of paste samples and  $V_p$  on preserved samples. Hence, it is likely that the same could be observed from comminuted rock for these formations. This would mean that we can determine  $V_p$  directly from pastes and maybe from drill cuttings. For example, at 100MHz:

$$V_p = 6805.8 - 107.68 * \epsilon''_r (\text{paste @ 100 MHz}) \quad (R^2 = 0.84) \quad [\text{Eq. 5}]$$

We would conclude that an approximate determination of laboratory  $V_p$  can be obtained from the drill cuttings dielectric measurements on pastes, but it is best to use the imaginary component. The most proper way of using this relationship would be to extract several preserved core samples and prepare them as pastes measured using the endloaded transmission line to create the best possible calibration chart for the well being analysed, then fit all of the cuttings data to the linear relationship determined from preserved powder. Obviously, the conversion from a laboratory measurement of  $V_p$  to the formation  $V_p$  would need to be well established before a  $V_p$  log from drill cuttings using dielectric analysis could be achieved, and this is currently a matter of ongoing research.

Note however that this type of correlation is inherently local and can't be extrapolated to any shale based on the analysis of data from a single shale formation or borehole. The explicit

relation ship bewteen electrical/dielectric and elastic properties, when established for a given shale, should exclusively used for that shale. Unsuccessful attempts have been made, aside from the current project, to use the correlations described in this report to predict  $V_p$  for other shales.

**Determining  $V_p$  from Dielectric Response**

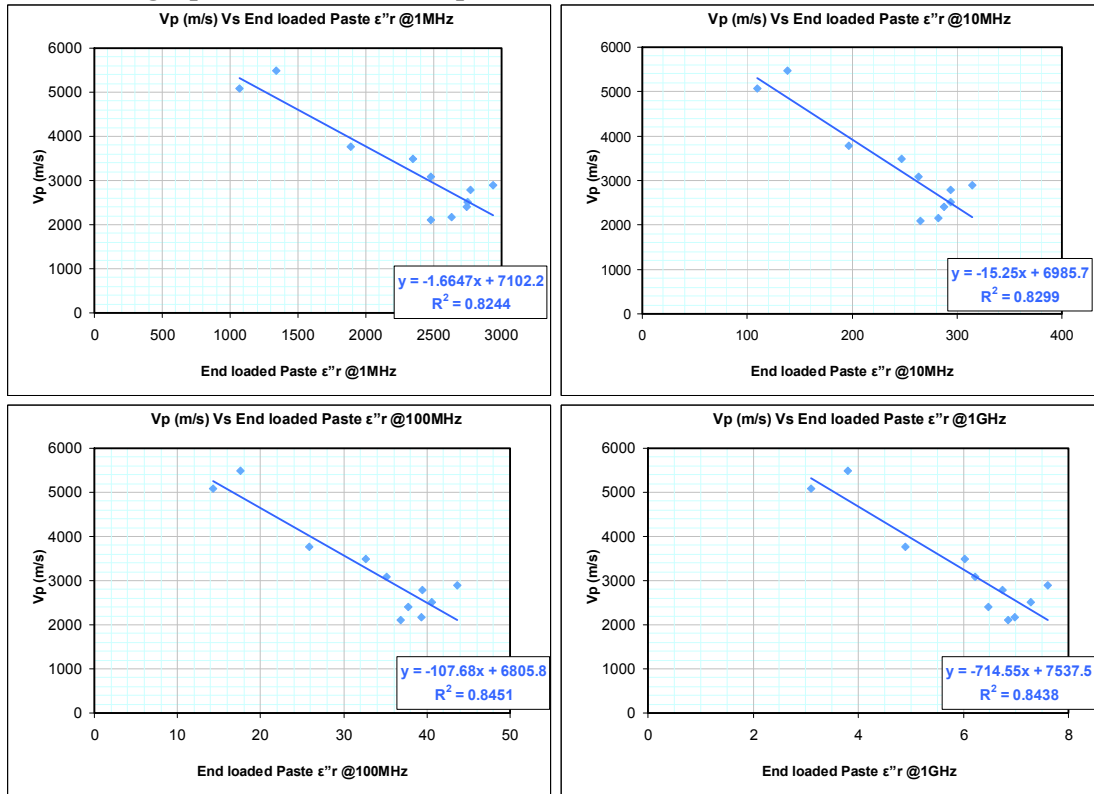


Fig. 5-1: The correlation observed between equivalent imaginary dielectric permittivity and  $V_p$ . The data presented covers the decadal incremental spot frequencies from 1 MHz to 1 GHz. The permittivity is measured on the paste sample prepared by drying and crushing preserved rock. The  $V_p$  measurement is performed directly on a preserved rock plug. We observe a strong negative correlation between  $V_p$  and the equivalent imaginary dielectric response of the powdered sample ( $V_p$  decreases as the equivalent imaginary dielectric response increases) and typically the correlation improves very slightly as the frequency is increased.

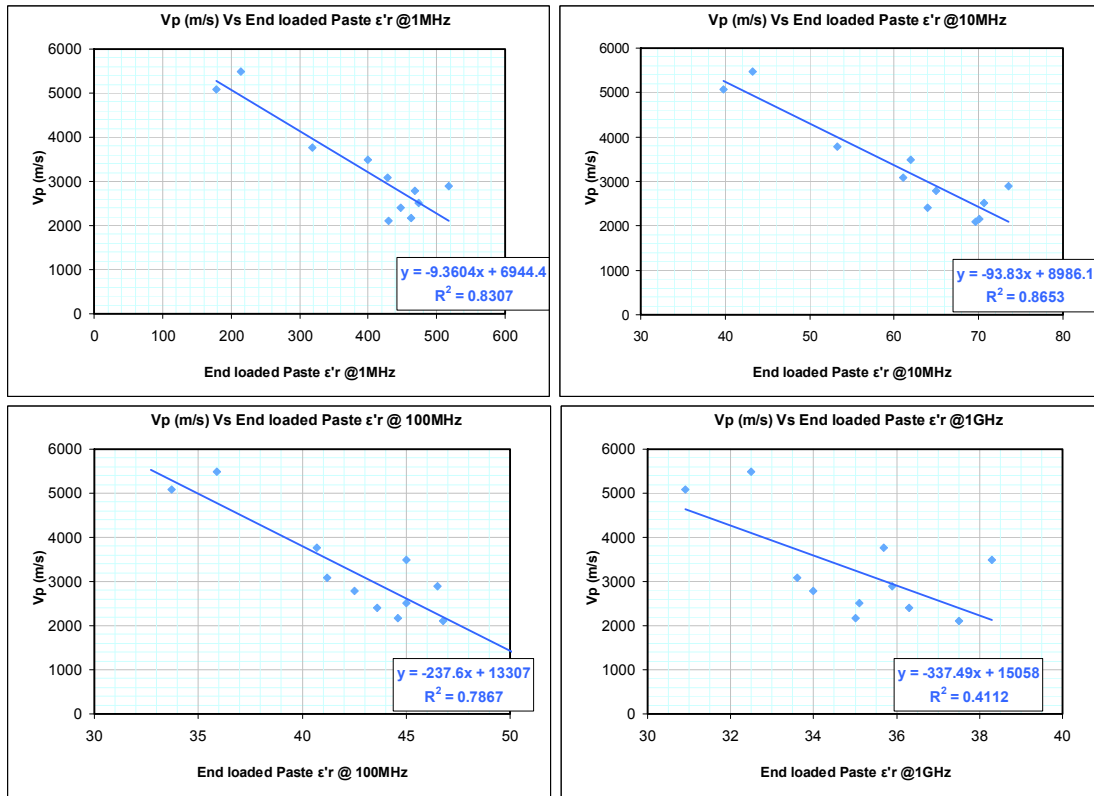


Fig. 5-2: The correlation observed between real dielectric permittivity and Vp. The data presented covers the decadal incremental spot frequencies from 1 MHz to 1 GHz. The permittivity is measured on the paste sample prepared by drying and crushing preserved rock. The Vp measurement is performed directly on a preserved rock plug. We observe a strong negative correlation between Vp and the real dielectric response of the powdered sample (Vp decreases as the equivalent imaginary dielectric response increases) and typically the correlation is better at low frequencies and reduces quite rapidly as the frequency exceeds 100 MHz. The optimum correlation occurs at 10 MHz.

### 5.1.2 Dielectrics and SSA

There is a positive correlation between both the real and equivalent imaginary dielectric permittivity and specific surface area (Figs. 5-3 and 5-4). The correlation between the real dielectric permittivity and SSA breaks down dramatically when the frequency exceeds 100 MHz, yet the correlation between equivalent imaginary dielectric permittivity and SSA is retained and slightly improves as the frequency is increased above 100 MHz. This is similar to the observation made for Vp for real and equivalent imaginary dielectric permittivity (Figs. 5-1 and 5-2). The two best approximations are as follows:

$$SSA = -124.26 + 3.2372 * \epsilon''r(\text{paste @ 10 MHz}) \quad (R^2 = 0.9324) \quad [\text{Eq. 6}]$$

$$SSA = -75.209 + 24.806 * \epsilon''r(\text{paste @ 1 GHz}) \quad (R^2 = 0.9206) \quad [\text{Eq. 7}]$$

These both provide better than 90% confidence and other historical data would indicate that these trends for SSA versus dielectric response are quite global. Note that the real physical meaning of these correlations is obscured, because they have non zero intercepts on both axes. That is to say, the paste correlations represent a hypothetical linear mixing, placing measured sample between model end members that do not physically exist (i.e. an idealised solid with bound charges and an idealised fluid with free charges). Texturally (Fig. 4-16), we would assume that a paste prepared dielectric measurement would reflect the water coating the interlayers within the clay minerals along with additional small droplets which would exist in the greater pore space as confirmed by NMR (Fig. 4-38 right). Expanding the textural model presented in Fig. 4-16 to explain electrical transport processes leads to a consideration of the role of swelling clays. In Fig. 5-5 simple cartoons of the two extreme cases are provided.

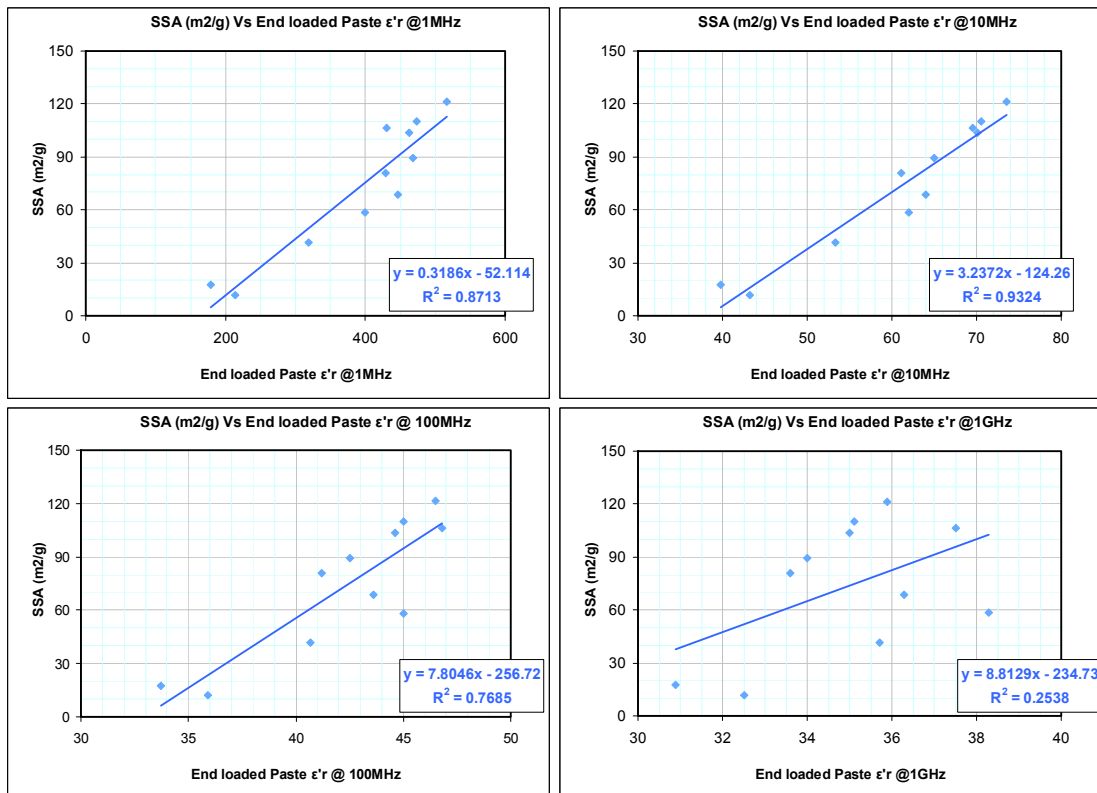


Fig. 5-3: The correlation observed between specific surface area and real dielectric permittivity for all of the spot frequencies. A strong positive correlation is observed (SSA increases with an increase in dielectric response), but the correlation is strongly reduced above 100 MHz. The optimum frequency to observe this correlation is at 10 MHz where the correlation is  $R^2 = 0.9324$ .

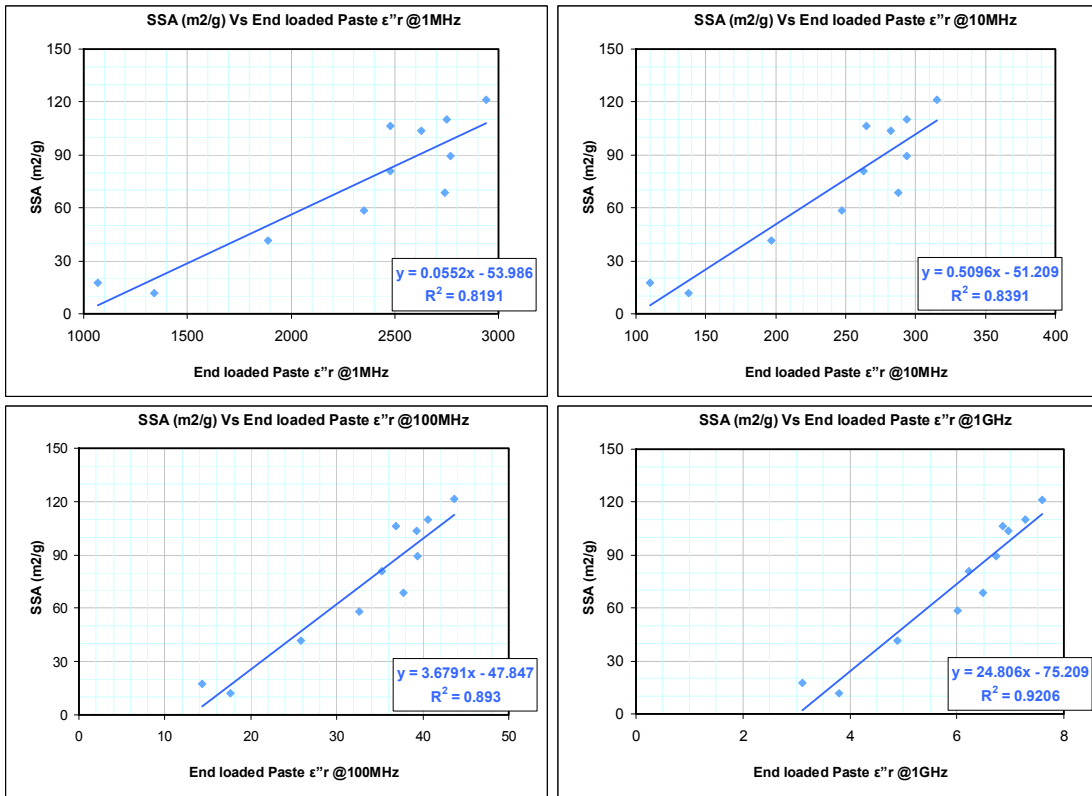


Fig. 5-4: The correlation observed between specific surface area and equivalent imaginary dielectric permittivity for all of the spot frequencies. The SSA shows a strong positive correlation with the equivalent imaginary dielectric permittivity better than  $R^2 = 0.81$  for all frequencies, but unlike the real dielectric permittivity the correlation improves slightly as the frequency is increased. At 1 GHz the correlation is  $R^2 = 0.9206$ .

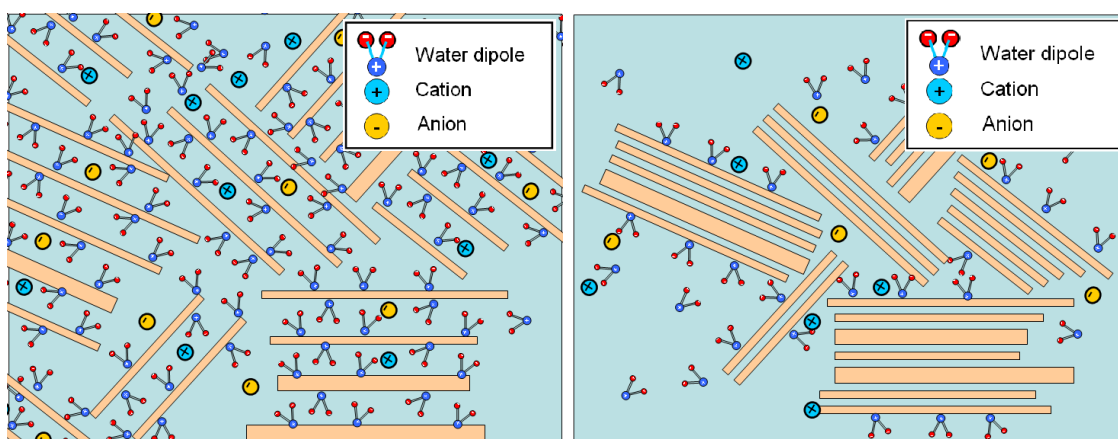


Fig. 5-5: (left) The high swelling clay content shale powder (clay platelets marked in orange) and (right) the low swelling clay content powder. In each case the water that is added (volume marked in light blue) to the sample form droplets between the disaggregated grains but the swelling clay retains a significant quantity of moisture in the interlayer volume. Ions occurring in the water form more easily in high SSA minerals and have a more pathways through which to conduct. We expect some of these ions to be free to migrate through the sample by hopping in and out of the platelets and into the free water. We also expect some of the ions to be less free to migrate and be constrained on the surfaces of the grains or within the interlayers. As such, the ions provide a dual role, participating in both conduction and polarisation and there real and equivalent imaginary dielectric permittivity.

In terms of the petrophysical model, we expect the swelling clays which permit water into the interlayer of the clay minerals to allow more conduction pathways through the paste sample. This occurs in addition to the creating of additional ions through CEC exchange processes that are later demonstrated in Fig. 5-9. There may be both charge hopping from grain-to-grain and grain-to-water facilitating overall conduction but likewise any component of the exchanged cations which is confined to the clay platelets will contribute to Maxwell-Wager polarisation of the mineral grains and this is one the reason why we observe a high dielectric permittivity below 10 MHz. In terms of experimental results, the Nagra shales demonstrate a reasonably wide range of SSA and in plotting a selection of these shales (ranging in SSA) we are able to demonstrate that the real and equivalent imaginary dielectric permittivities are both strongly influenced by SSA also supported by Figs. 5-3 and 5-4. Consider the following data set (Fig. 5-6) which includes a selection of SLA-1 shales with a range of SSA as marked.

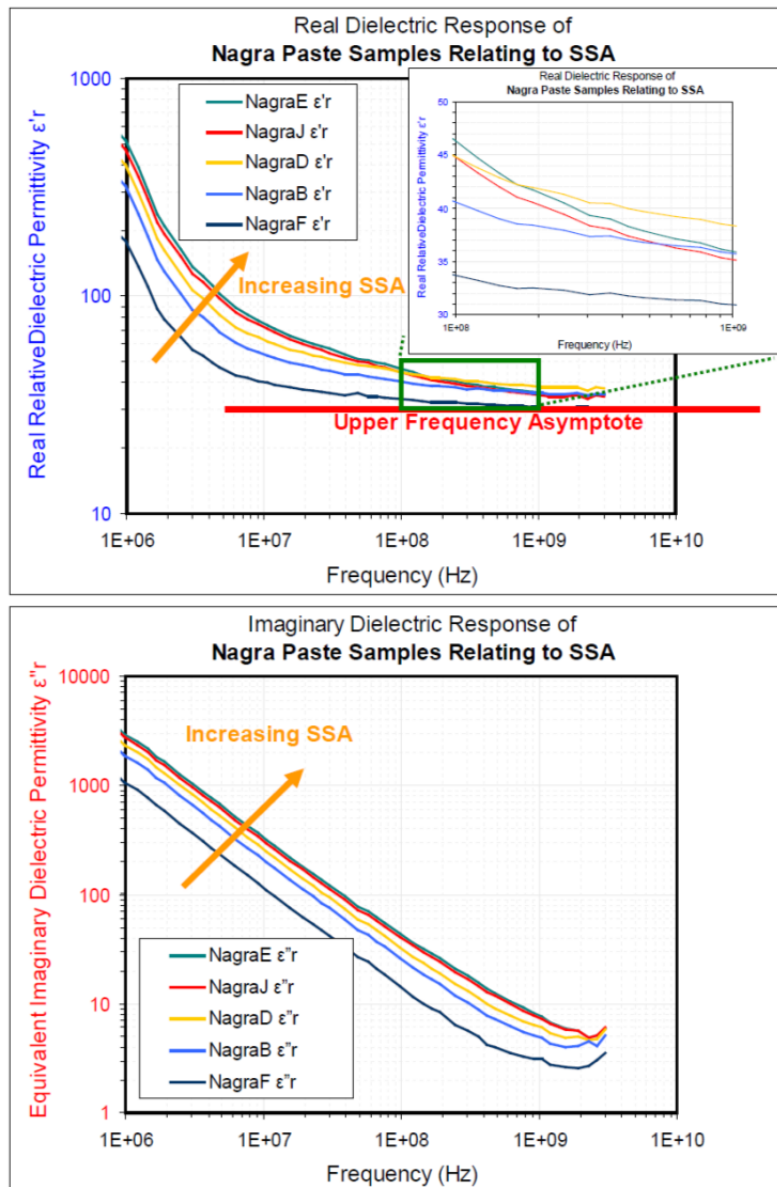


Fig. 5-6: Dielectric responses of a selected subset of the paste samples (Top and Top Inset) the real dielectric response, (Bottom) the equivalent imaginary dielectric response and (Bottom Inset) the conductivities. The samples have been selected to show how typical dielectric responses of shales are related to their SSA. The real dielectric response reduces with frequency to a plateau value of approximately 30 -40 but the real dielectric permittivity at 1 MHz is approximately 1 order of magnitude higher than the high frequency plateau. The real dielectric permittivity below 100 MHz is ordered according to SSA, with an increased SSA leading to an increased dielectric permittivity. In the frequency range between 100 MHz and 1 GHz the separation according to SSA is lost and it is apparent that the high frequency real dielectric permittivity is governed by other processes. Likewise the equivalent imaginary dielectric permittivity exhibits a simple downward 1-to-1 trend in frequency space which is consistent with conduction dominated loss, and is supported by the inset conductivity response. At above 100MHz the polarisation loss mechanisms begin to appear, but don't dominate equivalent imaginary dielectric permittivity until beyond 1 GHz.

The equivalent imaginary dielectric permittivity (Fig. 5-6 Top) displays a perfect downward 1-to-1 trend with frequency, which is characteristic of conduction processes dominating the total loss of the sample. Furthermore the spectra of samples are displaced from one another according to SSA with the highest SSA samples having an increased equivalent imaginary dielectric permittivity. For nearly the entire frequency range, conduction dominates this observation (Fig. 5-6 Inset) but at 100 MHz and above, it is apparent that dipolar loss becomes significant and dominates the equivalent imaginary dielectric permittivity above 1 GHz. We might anticipate that the strong correlation that we observe between equivalent imaginary dielectric permittivity and SSA would break down somewhere above 3 GHz because of dipolar loss, but we have insufficient data to prove this conclusively. Likewise, if we were investigating collection of rock samples with a lower propensity to absorb water and allow cation exchange, we may find that the reduction in conductivity may allow dipolar loss to appear earlier in the frequency sweep. The real dielectric permittivity is rather different (Fig. 5-6 Top). Conduction within the clay platy structures, leads to Maxwell-Wagner polarisation and subsequent establishment of a polarisable electric double layer. This gives rise to a high dielectric permittivity at low frequency but these processes are known to be quite slow and disappear as the frequency is increased. We observe that the spectra distributed according to SSA at all frequencies up to 100 MHz, with the highest SSA samples having an increased real dielectric permittivity. In the frequency range from 100 MHz to 1 GHz, the relative positions of the spectra become disordered relative to SSA and the remaining dielectric processes (presumably including dipoles in free water, bound water within the clays and clay minerals themselves) begin to dominate the upper frequency asymptote for each sample. If one was to rotate the real and equivalent imaginary dielectric permittivity's presented in Fig. 5-6 around a vertical axis onto a third plane for dielectric permittivity versus SSA then we would retrieve the same graphs presented in figure's Figs. 5-3 and 5-4. This explains why equivalent imaginary dielectric permittivity correlates with SSA for all frequencies whilst real dielectric permittivity losses correlation with SSA, as the frequency exceeds 100 MHz. The remaining unresolved question is what drives the upper frequency asymptote of the real dielectric permittivity of each sample given that it is clearly not SSA. Previous research (Fam and Dusseault , 1998; Myers, 1991) indicates that total moisture content is a possible factor (Fig. 5-7).

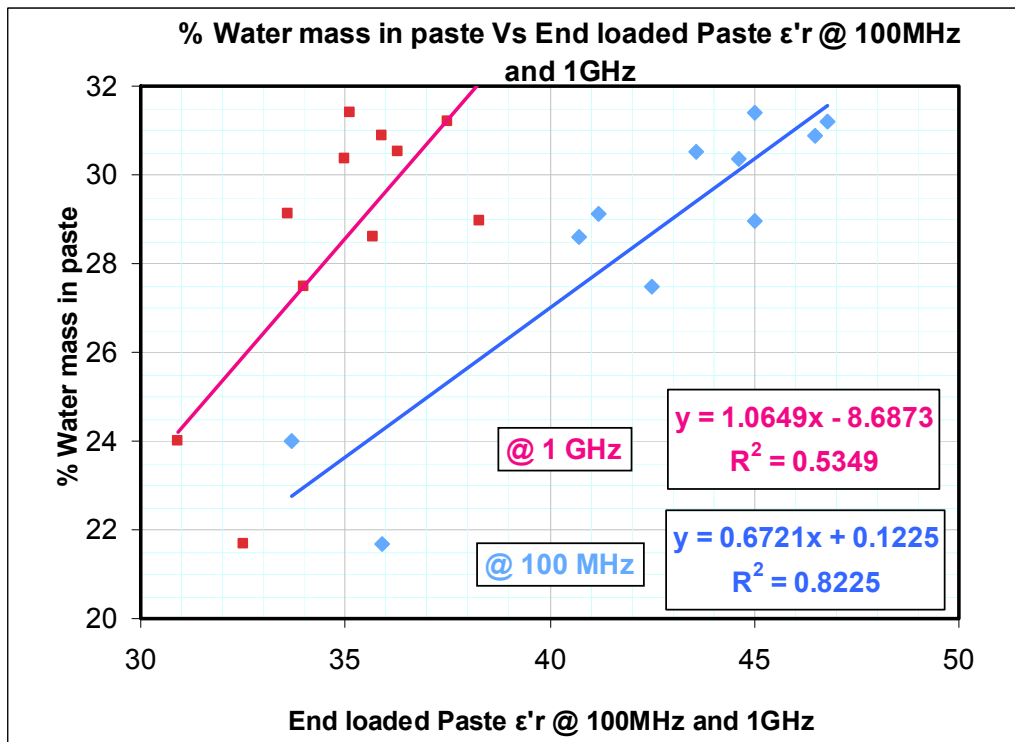


Fig. 5-7: There is reasonable positive correlation between the real dielectric permittivity and the % water content in the sample at 100 MHz ( $R^2 = 0.8225$ ). But the correlation become considerably worse as the frequency is increased from 100 MHz to 1 GHz

Water may occupy many locations within the paste sample, including free water with a range of droplet sizes and within the clay interlayers. Although water is believed to be the dominant cause of the upper frequency asymptote (i.e. the real dielectric permittivity above 1 GHz), the individual polarisability of each water molecule, will be affected by its interaction with nearby molecules. These include both clay grains and other bound/unbound water. It would be tempting to apply a mixing law to verify this claim, but of course where the free water is likely to have the published dielectric response of  $\epsilon'r = 80$ , the bound water will realistically have a distribution of polarisability and time constants (Fam and Dusseault, 1998), so determining the exact asymptotic value based on moisture content alone is difficult, even with an estimation of the ratio of bound to free water based on the SSA. So despite the commonly accepted belief (Fam and Dusseault, 1998), that the high frequency (1 GHz) dielectric response of any suspension or paste correlates with moisture content, it may in fact be complicated by differences in mineralogy and related microstructure. It is, however, likely that a data set containing unique, and/or sufficiently similar minerals, would retain a strong correlation between high frequency dielectric response and moisture content.

Put simply, the low frequency (<100 MHz) real dielectric permittivity is strongly linked to the SSA for reasons of conduction pathways within the platelets and the resulting Maxwell-Wagner polarisation. The high frequency (~1 GHz) response is indirectly linked to moisture content, with a number of complicating factors including interlayer hydration and non-unique bound water time constant. The entire frequency range of the equivalent imaginary dielectric permittivity is dominated by conduction processes which are directly related to SSA up to and including 1 GHz. The correlation is likely to breakdown beyond 1 GHz where polarisation loss begins to exceed conduction loss and dominates the equivalent imaginary dielectric permittivity.

### SSA Versus CEC

The propensity of ions to become liberated into the rock formation water is likely to be dependent on the quantity rock interfaces that are in contact with the water. In establishing a rock fabric model, this would translate into a simple correlation between SSA and CEC.

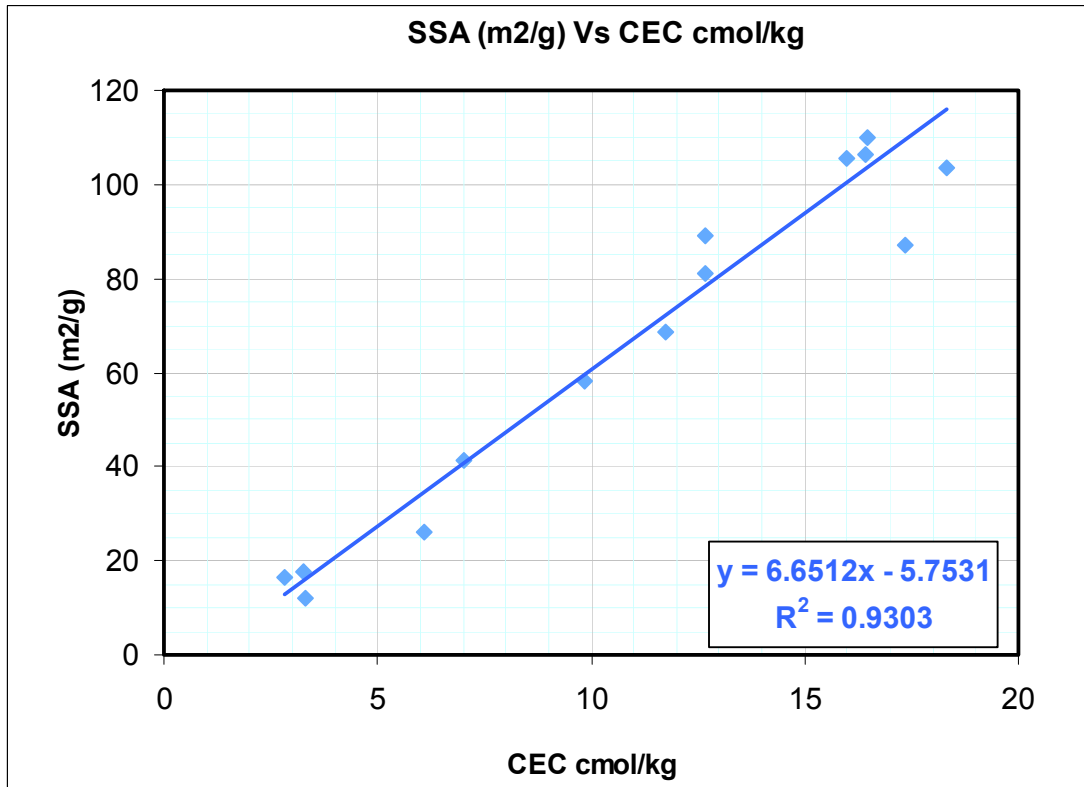


Fig. 5-8: The correlation observed between specific surface area determined by direct measurement in the laboratory using the EGME and the cation exchange capacity CEC determined during XRD analysis using tetra sodium pyrophosphate method. A strong positive correlation between SSA and CEC is observed ( $R^2 = 0.9303$ ).

Although the correlation is very strong (approximately 93%), this result was expected. Given SSA and dielectric properties were previously shown to correlation strongly (Figs. 5-3 and 5-4) we should also expect to find a strong relationship between dielectric response and CEC.

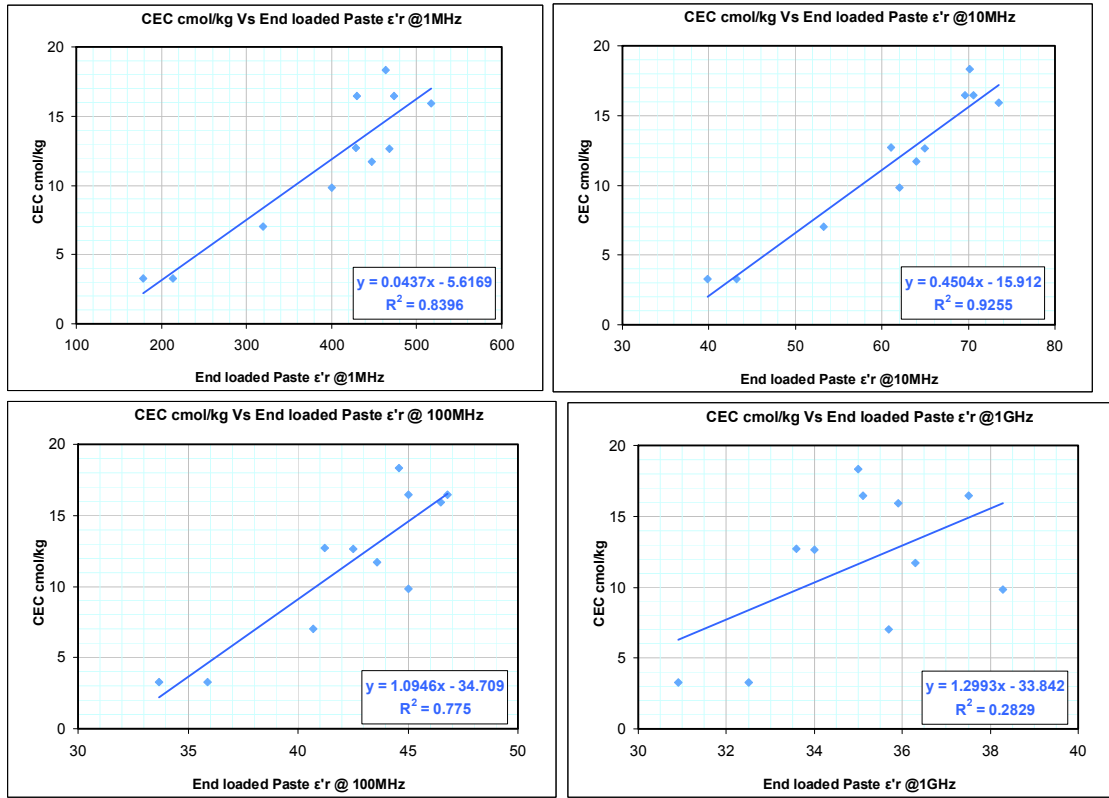


Fig. 5-9: The variation in cation exchange capacity versus real dielectric permittivity determined using endloaded paste measurement as the frequency is increased. Both measurements are done on samples prepared from a dried crushed preserved rock. We observe a strong positive correlation between CEC and endloaded real dielectric permittivity on the paste, but this correlation breaks down rapidly beyond 100 MHz.

The correlation that exists between CEC and SSA presented in Fig. 5-8 in conjunction with the data for SSA Versus dielectric response presented in Fig. 5-3a, naturally lead to a correlation between dielectric response and CEC (as shown in Fig. 5-9). But again this result was always expected and has been previously published (Leung and Steiger, 1992). In our case we find that:

$$CEC = -15.912 + 0.4504 * \epsilon'_{r(paste @ 10 MHz)} (R^2 = 0.9255) \quad [Eq. 8]$$

Leung and Steiger (1992) did not present a similar formulation for transforming from dielectric response to CEC. We can also demonstrate that there is a clearly optimum frequency for this effect in the vicinity of 10 MHz which is also consistent with the Leung and Steiger (1992) findings. Note that in other current similar studies we have investigated the link between dry powder dielectric response and CEC. Although the data is not yet available for presentation, these tests show that to have a linear and strongly predictive relationship, one must prepare a hydrated (at least partially) paste from the powder to allow the surface charges to become polarized by the applied electric field.

These data demonstrate that the internal surfaces within the shale are responsible for facilitating the cation exchange processes leading to ions that participate in polarisation phenomena when an external electric field is applied. As the electric field frequency is increased, the ions are either sufficiently bonded to the grain interfaces or have excessive inertia or lack the mobility to achieve the same level of polarisation that is possible at lower frequency. These observations would also be consistent with the rock fabric that is depicted in Fig. 4-16. At sub micron scale (Fig. 5-5), the platy structure of clay minerals, which is responsible for the high specific surface area, either facilitates a captive region in which liberated ions can participate in polarisation or simply they liberate ions into the nearby free water. According to our proposed petrophysical model, this would occur in the same location within the rock samples that cementing and connection between the rock grains occurs and it would be likely that hydration and cation exchange would affect the mechanical rigidity of these connections. Subsequently, the elastic and inelastic deformability of the connections between grains is affected by occurrence of hydration resulting from additional SSA, and we would expect this as being the cause of the relationship between dielectric and P-wave properties that we demonstrated in Figs. 5-1 and 5-2. Given that most clays are generally strongly hydrophilic, we would anticipate that the availability of specific surfaces would be generally linked to the propensity for the shales to gain and retain moisture. We commonly notice in the laboratory that dried shales samples quickly acquire moisture from the atmosphere, particularly if they consist of swelling clays. Using these arguments, we would anticipate that the preserved nature of the samples would lead to retention of the formation fluid and moreover, that the content of moisture is linked to the specific surface area (Fig. 5-10), which is actually determined after drying.

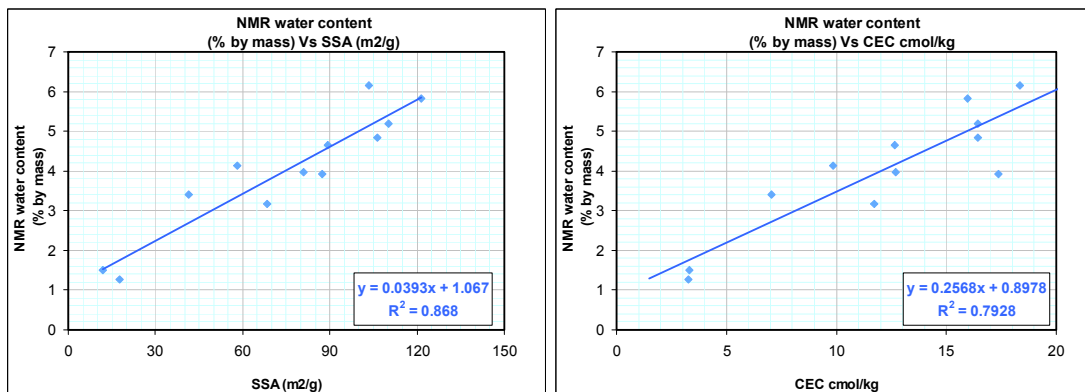


Fig. 5-10: Moisture within the preserved sample determined from NMR at 2 MHz versus Left) The specific surface area determined after drying cleaning and crushing and Right) the cation exchange capacity. The % water retained in the preserved sample shows a strong positive correlation with both the SSA ( $R^2 = 0.868$ ) and the CEC ( $R^2 = 0.8252$ ).

Given that the correlation between SSA and CEC versus dielectric response has already been shown to be quite strong we would expect a similar correlation with the dielectric response (Fig. 5-11).

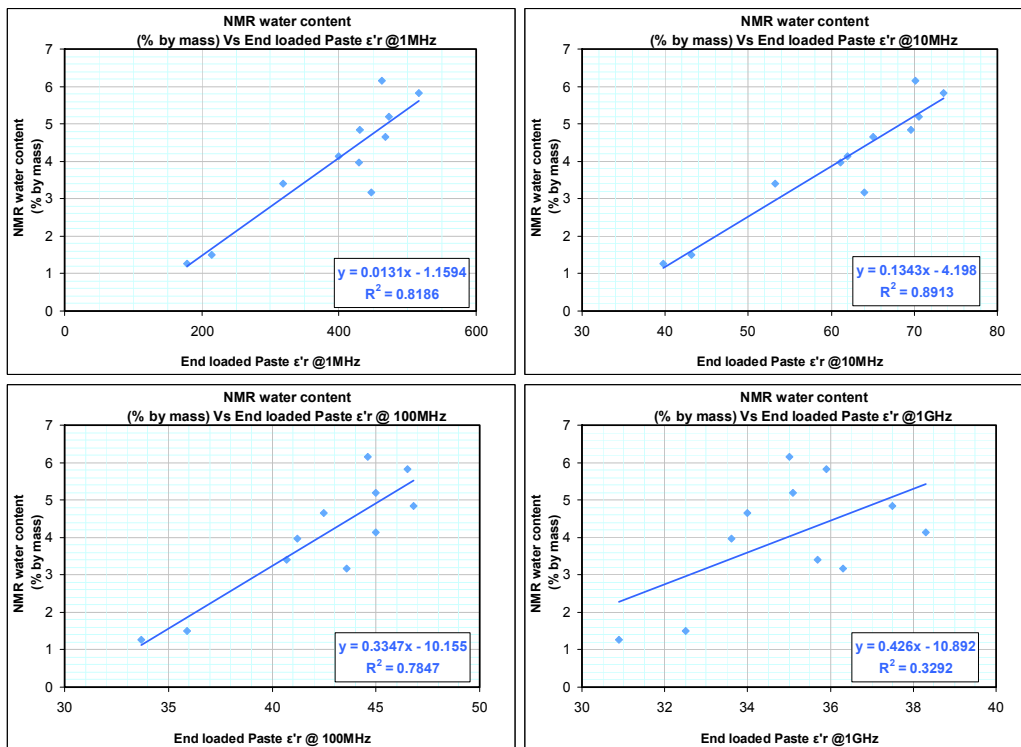


Fig. 5-11: The relationship between the moisture content determined from NMR on the preserved sample versus the endloaded dielectric permittivity of the paste samples. The data presented covers the decadal incremental spot frequencies from 1 MHz to 1 GHz. The data show a strong positive correlation which breaks down rapidly above 100 MHz.

The relationship between moisture content determined using a 2 MHz Maran NMR and the dielectric response indicates that the low frequency response correlates well but the high frequency dielectric response rapidly loses its correlation. Typically, the high frequency dielectric response would be associated with water dipole polarisation that can occur in “droplets” rather than ultra thin coatings and water monolayers which are known not to polarise as much or as fast because the charge carriers are “bound” directly or indirectly by surface forces. At low frequency, we would typically attribute the increase in dielectric response to surface space-charge polarization process. What we observe is a good correlation at low to intermediate frequency that rapidly disappears from 100 MHz to 1 GHz. These results (Fig. 5-11) are essentially indicating that the moisture content detectable by NMR is more associated with the surfaces rather than free pore-space water. However, this is not a definite conclusion, as we still need additional information to identify exactly where within the rock fabric the dielectric polarisation is occurring. It may be mainly within the free pore water resulting from the existence of ions liberated through cation exchange processes, or the polarisation may actually be dominantly occurring at the interfaces themselves. More elaborate experiments (stepwise hydration, perhaps relationships of polarization and conductivity increments with temperature) would be necessary to exactly answer these questions. What we can see from this study is that dielectric measurements on both intact samples and pastes can add a valuable component of electrochemical information to any study of shales or mudrocks.

### **5.1.3 Mineralogy, water content and velocities**

Table 4-3 (bottom) and Figure 5-12 synthesize the mineral content of the core samples in terms of total amount of clay, carbonates, feldspars and quartz as derived from full XRD analysis (see Section 4.3.4). The results confirm broadly the lithology description proposed by NAGRA excepted for one plug: NAGRA-H indicated as a sandy claystone which is almost a pure carbonates (> 80%). The NAGRA-J sample (Opalinus Clay, sandy claystone) is the most rich in clay minerals that we ascribe as a shale type.

The carbonates and clays content seem to control most of the water trend (Middle plot in Fig. 5-12) with a particular relationship between carbonates and velocities (Fig. 5-12: bottom plot) that we relate to a certain level of cementation effect. This is just a rough tendency and the mineralogical details will have to be performed with better technique on XRD to properly extract the carbonates and different types of clay minerals (presently ongoing).

## **5.2 Executive summary of petrophysics and rock physics results**

A total of 15 core samples from the geothermal well SLA-1 were subjected to detailed mineralogical, petrophysical and rock physical characterization. A variety of complementary laboratory techniques were applied to determine the key rock properties and to assess the methodological uncertainties of the different laboratory techniques. Thus, porosity was determined by NMR and by weight loss measurements after drying. Different protocols were used both for NMR studies and for the weight loss measurements. Table 5-1 summarises the representative petrophysics and rock physics results. All data are available in electronic format (EXCEL; see also Appendix A).

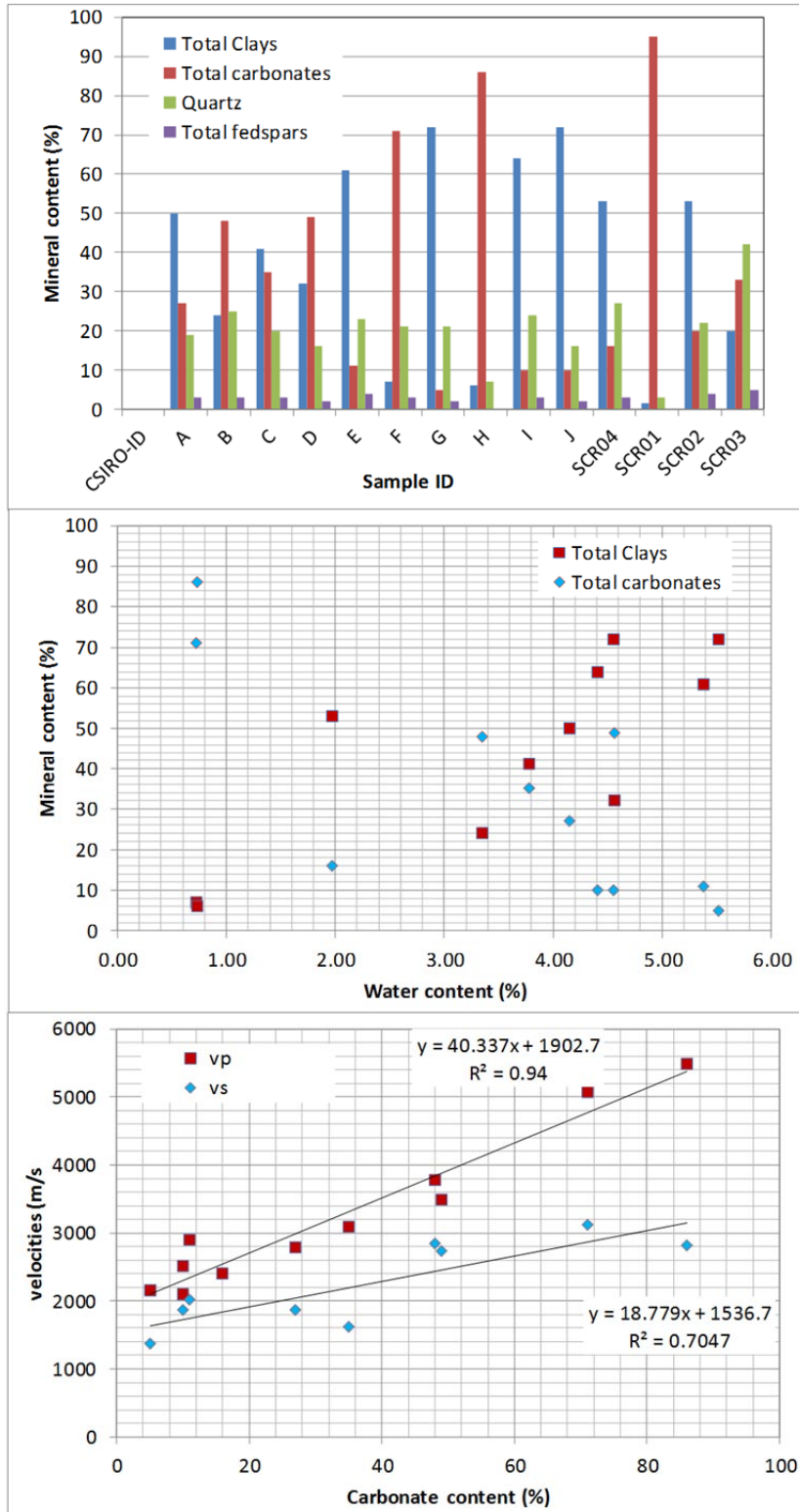


Fig. 5-12: Mineralogy analysis on each NAGRA plugs (Top) with comparisons of carbonates and water content from NMR (%) and velocities (m/s).

Tab. 5-1: Executive summary of petrophysics and rock physics results.

Sample #	Depth (m bg)	**Massic water (%)	Pore water salinity (g/l)	Resistivity at 1 kHz	Vp (m/s)	Vs (m/s)	*Wet Bulk density (g/cc)	**Grain density (g/cc)	**Poro- sity (%)
A	761.85- 762.06	4.15	14.02	N/A	2793.5	1864.4	2.55	2.74	10.59
B	766.15- 766.52	3.35	10.81	54.33	3775.4	2164.9	2.55	2.70	8.56
C	772.76- 773.00	3.78	13.28	53.88	3086.4	1612.5	2.54	2.71	9.61
D	773.60- 773.90	4.56	12.40	57.01	3493.6	2052.9	2.52	2.72	11.51
E	812.59- 812.86	5.38	12.27	22.67	2899.6	2013.3	2.52	2.75	13.53
F	826.72- 827.00	0.72	10.21	498.57	5075.0	3114.8	2.67	2.70	1.92
G	835.62- 835.89	5.52	17.18	56.20	2160.5	1376.5	2.45	2.68	13.51
H	886.60- 886.88	0.73	12.94	438.61	5481.3	2821.8	2.71	2.75	1.98
I	929.86- 930.10	4.41	12.92	33.20	2097.4	N/A	2.51	2.70	11.09
J	946.08- 946.37	4.55	12.79	54.20	2510.2	1484.8	2.50	2.69	11.39
SCR04	856.09- 856.40	1.97	21.26	57.15	2401.2	N/A	2.55	2.63	5.03

\* The wet bulk density measured on preserved plugs (File: Water\_analysis.xls)

\*\* The massic water, grain density and porosity is measured from the evaporation method at 105C after 1 month (File: Water\_analysis.xls).

## References

- Albert W., H.R. Bläsi, H. Madritsch, T. Vogt, H.P. Weber (2012): Geologie, Stratigraphie, Strukturgeologie, bohrlochgeophysikalisches Logging und Wasserproben der Geothermiebohrung Schlattingen SLA-1 (Rohdaten). Nagra Project Report NPB 12-16, Nagra, Wettingen, Switzerland.
- Atkins, P.W., 1986. Physical Chemistry, Third Edition, W.H. Freeman and Co., New York, 663-671.
- Archie, G.E., 1942. Electrical resistivity an aid in core-analysis interpretation. Am. Ass. Petrol. Geol. Bull., 31, 350-366.
- Baker-Jarvis, J., Vanzura, E.J., Kissick, W.A., 1990. Improved technique for determining complex permittivity with the transmission reflection method, IEEE Transactions on Microwave Theory and Techniques, vol. 38, no. 8, August.
- Berezanski, P., 1997. Handbook of Instrumental Techniques for Analytical Chemistry, Chapter 39, F. Settle, Ed., Prentice-Hall, Upper Saddle River, NJ, 749-764.
- Burdette, E.C., Cain, F.L., Seals, J., 1980. In Vivo probe measurement technique for determining dielectric properties at VHF through microwave frequencies, IEEE Transactions on Microwave Theory and Techniques, vol. MTT-28, no. 4, pp.414-427, April.
- Cerato, A. B., Lutenegger, A. J., 2002. Determination of Surface Area of Fine-Grained Soils by the Ethylene Glycol Monoethyl Ether (EGME) Method, Geotechnical Testing Journal, Sept, 2002, vol. 25, no. 3, pp 315-321.
- Coates, G.R., Xiao, L. and Prammer, M.G., 1999. NMR Logging: principles and Applications, Halliburton Energy Services, Houston, 234 pp.
- Detournay, E. and Defourny, P., 1992. A Phenomenological model for the drilling action of drag bits. *Int. J. Rock Mech. Min. Sc. & Geomech. Abstr.*, 29, 13-23.
- Dunn, K.-J., Bergman, D.J. and Latorraca, G.A., 2002. Nuclear Magnetic Resonance: Petrophysical and Logging Applications. Pergamon, Amsterdam, 293pp.
- Gilmore R.J., Clark B., Best D., 1987. Enhanced Saturation Determination Using the EPT-G Endfire Antenna Array. SPWLA Trans., 28th Annual Logging Symposium, London, England. K1-K24.
- Guéguen, Y., Palciauskas, V., 1994. Introduction to the Physics of rocks. Princeton University Press, 392 pp.
- Handwerger, D.H., R. Suarez-Rivera, K.I. Vaughn and J.F. Keller, (2011). Improved Petrophysical Core Measurements on Tight Shale Reservoirs Using Retort and Crushed Samples. SPE Paper 147456.
- Hizem, M., Budan, H., Deville, B., Faivre, O., Mosse, L., Simon, M., 2008. Dielectric dispersion: A new wireline petrophysical measurement, SPE 116130, Annual Technical Conference, Colorado USA, September.

- Holler, F.J. and Enke, C.G., 1996. Laboratory Techniques in Electroanalytical Chemistry, 2<sup>nd</sup> Edition, Chapter 8, P.T. Kissinger and W.R. Heineman, Eds., Dekker, New York, 237-265.
- Josh, M., B. Clennell, T. Siggins., R. Banks, 2007. Wideband electrical/dielectric measurements from millihertz to gigahertz frequencies, 77<sup>th</sup> Annual Meeting of the SEG, San Antonio, TX, Expanded Abstracts, 1701-1705.
- Kellomaki, A., Nieminen, P., Ritamaki, L., 1987. Sorption of Ethylene Glycol Monoethyl Ether (EGME) on Homoionic Montmorillonites, Clay Minerals, vol. 22, pp 297-303.
- Lasswell, P.M., 2006. Core analysis for electrical properties. *Petrophysics* 47, 191-213.
- Leung, P.K., Steiger, R.P., 1992. Dielectric constant measurements: A new, rapid method to characterize shale at the wellsite. IADC/SPE Drilling Conference paper No. IADC/SPE 23887, New Orleans, 401-408.
- Mazurek, M. (2011): Aufbau und Auswertung der Gesteinsparameter-Datenbank für Opalinuston, den 'Braunen Dogger', Effinger Schichten und Mergelformationen des Helvetikums. Nagra Arb. Ber. NAB 11-20.
- Nicholson, A.M., Ross, G.F., 1970. Measurement of the intrinsic properties of materials by Time-Domain techniques, IEEE Transactions on Instruments and Measurement, vol. IM-19, no. 4, November.
- Olsen, C., Christensen, H.F., and Fabricius, I.L. (2008). Static and dynamic Young's moduli of chalk from the North Sea. *Geophysics*, 73, 41-50
- Richard, T., 1999. Determination of rock strength from cutting tests. *PhD Thesis*, University of Minnesota.
- Sawyer, D.T., Sobkowiak, A. and Roberts, J.L., 1995. *Electrochemistry for Chemists*, 2<sup>nd</sup> Edition, Wiley, New York, 318.
- Schwank M., Green T.R., Mätzler C., Benedickter H. and Flühler H., 2006. Laboratory Characterization of a Commercial Capacitance Sensor for Estimating Permittivity and Inferring Soil Water Content. *Vadose Zone Journal*, 5:1048-1064.
- Serra, O., 1984. Fundamentals of Well-Log Interpretation (Vol. 1): The Acquisition of Logging Data: Dev. Pet. Sci., 15A: Amsterdam (Elsevier).
- Shugar, G.J. and Dean, J.A., 1990. *The Chemist's Ready Reference Handbook*, McGraw-Hill, New York, 20.10 - 20.17.
- Sims, J.C., Cox, P. T. and Simpson, R.S., 1988. Complex Dielectric Constant Well Logging Means and Method for Determining the Water Saturation and the Water Resistivity of an Earth Formation. *U.S. Patent No. 4774471*.
- Stuchly, M.A., Stuchly, S.S., 1980. Coaxial line reflection methods for measuring dielectric properties at radio and microwave frequencies—A Review. IEEE Transactions on Instrumentation and Measurement, Vol. 29, No. 3. 176-183.

Tan, C.P., 2008. Subsurface interval strength identifying tool for underground formation, has powered positioning device and caliper determining depth and width of scratches, and relative strength of formations based on scratches. Patent numbers: US2008184772-A1; WO2008098035-A1; IN200904593-P4; MX2009007808-A1; US7921730-B2. Patent assignee names and codes: SCHLUMBERGER TECHNOLOGY CORP(SLMB-C) PRAD RES&DEV LTD (PRAD-Non-standard) SCHLUMBERGER TECHNOLOGY BV(SLMB-C).

Vic Roads RC 355.01, 1996. Total surface area by retention of ethylene glycol monoethyl ether (EGME). Geopave, Manual of testing, test method RC355.01, 4pp.

Von Hippel, A.R., 1954. Dielectric Materials and their Applications. The Technology Press of M.I.T., United States of America.

Wang et al. (Soil Sci. Soc. Am. J., 1996, 60, 138-141).

Weir, W.B., 1974. Automatic measurement of complex dielectric constant and permeability at microwave frequencies, IEEE Trans., vol. 62, 33-36.



## Appendix A – Structure of the electronic data base

### 1 Overview

Auxiliary digital files containing the whole set of data were made available to NAGRA. The electronic data base ensures the traceability of the reported raw data and the results of data analyses and collects all graphical data representations. The electronic data base is organized in the 3 main directories:

- 1Reporting: Contains the CSIRO status reports and the final report in word format and pdf format
- 2ResultFigures: Contains all figures in a standard graphics format (jpg, wmf, etc) according to the sequence of the report outline (2\_X-Ray-Imaging; 3\_Mechanics; 4\_Petrophysics-RockPhys)
- 3DataFiles: Contains all raw data and data interpretations according to the sequence of the report outline (2\_X-Ray-Imaging; 3\_Mechanics; 4\_Petrophysics-RockPhys)

The detailed description of the contents of the directory “0DataFiles”

### 2 The data directory “3DataFiles”

The data directory contains all raw data and data interpretations according to the sequence of the report outline (2\_X-Ray-Imaging; 3\_Mechanics; 4\_Petrophysics-RockPhys) as given in Figure A1

2_X-Ray-Imaging	19.03.2012 14:19
3_Mechanics	19.03.2012 14:19
4_Petrophysics-RockPhys	27.11.2012 16:23

The sub-directory “2\_X-Ray-Imaging” comprises the CT-scans of all scanned plugs. JPG-Pictures of the cores along and normal to the core axis are given in the sub-directories Plug\_CT\_Slices and Wholecore\_Slice\_montage. The directory Raw\_data\_CT contains the raw data of the plug scans and the full core scans.

2_X-Ray-Imaging	
CTscan	
Plug_CT_slices	19.03.2012 14:19
Raw_data_CT	19.03.2012 14:20
Wholecore_slice_montage	19.03.2012 14:20

The sub-directory “3\_Mechanics” comprises the results of the Scratch tests and the UCS tests as EXCEL-Files.

 Scratch-SCR01.xls	09.12.2011 04:55	Microsoft Excel 97...	517 KB
 Scratch-SCR02.xls	09.12.2011 04:55	Microsoft Excel 97...	547 KB
 Scratch-SCR03.xls	09.12.2011 04:55	Microsoft Excel 97...	648 KB
 Scratch-SCR04.xls	09.12.2011 04:56	Microsoft Excel 97...	531 KB
 Scratch-SCR05.xls	09.12.2011 04:56	Microsoft Excel 97...	546 KB
 UCS-SCR01.xls	03.11.2011 07:16	Microsoft Excel 97...	10'012 KB
 UCS-SCR02.xls	03.11.2011 07:17	Microsoft Excel 97...	9'432 KB
 UCS-SCR03.xls	03.11.2011 07:17	Microsoft Excel 97...	9'621 KB

The sub-directory “4\_PetrophysicsR\_RockPhys” comprises the results of the dielectric, porosity (NMR, weight loss), mineralogy and ultrasonic measurements.

 Dielectrics	19.03.2012 14:20
 EIS	19.03.2012 14:20
 NMR	19.03.2012 14:20
 Pore_water_Salinity	19.03.2012 14:19
 Ultrasonic	19.03.2012 14:20
 Water_evaporation_discs	19.03.2012 14:19
 XRD_Report Extension 29.05.2012	27.11.2012 16:23
 XRD_Semi_quantitative	12.07.2012 13:26

## Appendix B – Photo documentation of core samples

### 1 List of core samples as received by CSIRO

CSIRO ID	Stratigraphie	Lithologie	KM	Status (August 2011)		Teufe		Konditionierung	Probenlänge (cm)	Kernmarsch-entnahme	Proben-nahme	Bemerkung
				Versand	Empfänger	von [m]	bis [m]					
SCR1	Effinger Schichten	Mergelkalk	9	21.06.2011	CSIRO	748.22	748.62	Harz	40	17.03.2011	18.06.2011	Nachbeprobung
A	Varians-Schichten	Tonmergel	15	15.07.2011	CSIRO	761.85	762.06	Harz	21	18.03.2011	22.03.2011	Nachbeprobung
B	Varians-Schichten	Tonmergel	16	15.07.2011	CSIRO	766.15	766.52	Harz	37	19.03.2011	19.03.2011	
SCR2	Parkinsoni-Würtembregica i.W.S	Tonmergel	17	21.06.2011	CSIRO	770.03	770.44	Harz	41	19.03.2011	18.06.2011	Nachbeprobung
C	Parkinsoni-	Tonmergel	18	15.07.2011	CSIRO	772.76	773	Harz	24	19.03.2011	22.03.2011	Nachbeprobung
D	Parkinsoni-Würtembregica i.W.S	Ton-/Kalkmergel	19	15.07.2011	CSIRO	773.60	773.9	Harz	30	20.03.2011	20.03.2011	
SCR5	Blagdeni Schichten	Tonmergel	28	21.06.2011	CSIRO	801.53	801.93	Harz	40	22.03.2011	18.06.2011	Nachbeprobung
E	Wedelsandstein	Tonstein	32	15.07.2011	CSIRO	812.59	812.86	Harz	27	23.03.2011	23.03.2011	
SCR3	Wedelsandstein	Sandmergel	36	21.06.2011	CSIRO	826.16	826.66	Harz	39	24.03.2011	18.06.2011	Nachbeprobung
F	Wedelsandstein	Kalkmergel	36	15.07.2011	CSIRO	826.72	827	Harz	28	24.03.2011	24.03.2011	
G	Murchisonae Schichten	Tonstein	41	15.07.2011	CSIRO	835.62	835.89	Harz	27	11.04.2011	11.04.2011	
SCR4	Opalinus Ton	Tonstein	50	21.06.2011	CSIRO	856.09	856.40	Harz	39	13.04.2011	18.06.2011	Nachbeprobung
H	Opalinus Ton	Tonsandstein	62	15.07.2011	CSIRO	886.60	886.88	Harz	28	17.04.2011	17.04.2011	möglicherweise Kataklasi?
I	Opalinus Ton	Tonsandstein	80	15.07.2011	CSIRO	929.86	930.10	Harz	24	09.06.2011	09.06.2011	
J	Opalinus Ton	Tonsandstein	86	15.07.2011	CSIRO	946.08	946.37	Harz	29	11.06.2011	11.06.2011	

2 Photo documentation of core samples

SCR1

Sample A



Sample B

SCR1, Samples C & D

